Universitat
de Girona

Hevar Hamid Abdulrahman

Modelling of the Interfacial Behaviour between Fiber Reinforced Polymer Rebars and Concrete

FRP++
Advanced structural analysis and
design using composite materials

Master Dissertation
European Master Advanced Structural Analysis and
Design using Composite Materials

Work developed under the supervision of
Professor Doctor Cristina Barris
Professor Doctor Karim Benzarti
Professor Doctor Sylvain Chataigner

July 2025

DECLARATION

Name: Hevar Hamid Abdulrahman

Email: hevarrahman@yahoo.com   **Phone number:** +351 91 221 2116

Citizen Card Number: Z3005086A

Title of the Dissertation: Modelling of the Interfacial Behaviour between Fiber Reinforced Polymer Rebars and Concrete

Supervisors:

Professor Doctor Cristina Barris

Professor Doctor Karim Benzarti

Professor Doctor Sylvain Chataigner

Year of Conclusion: 2025

Master Course in Advanced Structural Analysis and Design using Composite Materials

University of Girona, 15/07/2025

Signature:

ACKNOWLEDGEMENTS

I dedicate this dissertation to my late uncle, who passed away at the beginning of this journey. You are deeply missed and will forever remain in our hearts. I only wish that circumstances had allowed us to be closer and that I had the chance to know you more intimately. I hope to carry forward even a fraction of your legacy. May your place now be far better.

First and foremost, I would like to express my heartfelt thanks to the directors, coordinators, and lecturers of the FRP++ program. My special gratitude goes to my supervisors, who supported me throughout this journey. Their dedication, patience, and attention to detail consistently helped me improve and stay on track. I'm truly grateful for their guidance, and I hope to carry forward the lessons I've learned under their mentorship. The FRP++ program itself has been a truly enriching journey into the world of composites. Through well-structured organisation and expert guidance, it has successfully imparted decades of knowledge in a way that will stay with us for a lifetime.

I am deeply grateful to my family, and especially my parents, for their constant support throughout my academic path. Their unquestionable trust in me has been a steady source of strength. The unconditional love of the family is a true miracle and a blessing that cannot be found elsewhere.

I want to extend my heartfelt thanks to all my loyal friends who stood by me through highs and lows. To each of you who lifted me up whenever I faltered, I sincerely hope that your own journeys bring you even greater success and happiness than you have helped bring to mine. Friendship, at its best, is the quiet strength we lend one another, regardless of the space and time between us.

Last but not least, I want to sincerely thank Dr. Wrya for his continuous support since he first became my lecturer during my bachelor's studies. From the very first course you taught us, you have gradually nurtured my understanding of the academic world, beginning with your ingenious explanation of the concept of replicability. Having someone of your calibre believe in my potential is a true honour and a source of pride.

In the end, I hope to live up to your expectations and bring even more pride to your believing hearts. Your support is what keeps me pushing forward, and you are the reason I am where I am today. A heartfelt thank you to each and every one of you.

Modelización del Comportamiento Interfacial entre Armaduras de Polímero Reforzado con Fibra y Hormigón

RESUMEN

Actualmente, las barras de refuerzo de acero se usan comúnmente para reforzar el concreto a tracción. Sin embargo, esto puede provocar el deterioro de la estructura por corrosión del acero. Por ello, se han introducido las barras de polímero reforzado con fibra (FRP) como una alternativa libre de corrosión. El creciente interés en esta tecnología de refuerzo requiere comprender su interacción con el concreto. En consecuencia, en las últimas décadas se han realizado numerosas investigaciones experimentales, así como modelados analíticos y numéricos del comportamiento de adherencia. No obstante, la falta de procesos estandarizados de deformación superficial y fabricación, junto con múltiples factores que influyen en la adherencia, generan gran variabilidad en las relaciones esfuerzo-deslizamiento entre diferentes barras.

Para entender mejor estas variaciones, esta investigación desarrolla un modelo numérico en Abaqus para caracterizar el comportamiento interfacial entre barras de polímero reforzado con fibra de vidrio (GFRP) indentadas y concreto en ensayos de tracción. Se creó un modelo axisimétrico que requiere datos experimentales mínimos. La barra de GFRP se modela como material linealmente elástico, mientras que el concreto usa el modelo de plasticidad con daño para captar su comportamiento inelástico.

La precisión y estabilidad se mejoran mediante calibración rigurosa de los parámetros del modelo constitutivo y detalles geométricos, y análisis de sensibilidad sobre el ángulo de dilatancia, parámetro de viscosidad y coeficiente de fricción. Finalmente, se realiza un estudio paramétrico para evaluar la validez del modelo con diversas geometrías y diámetros de barras.

Aunque el modelo reproduce la forma general de la curva esfuerzo-deslizamiento tras la calibración, se observa una sobreestimación constante del esfuerzo máximo y discrepancias en el deslizamiento respecto a los datos experimentales, especialmente en barras de menor diámetro. Estos resultados evidencian la complejidad del comportamiento de adherencia GFRP-concreto y apuntan a futuras mejoras para aumentar la precisión predictiva en distintas aplicaciones.

PALABRAS CLAVE: Adherencia GFRP-concreto; Ensayo de extracción; Modelado por elementos finitos; Plasticidad con daño del concreto.

Modelització del Comportament Interfacial entre Armadures de Polímer Reforçat amb Fibra i Formigó

RESUM

Actualment, les barres d'acer per a reforç s'utilitzen habitualment per reforçar el formigó a tracció. Tanmateix, això pot provocar el deteriorament de l'estructura a causa de la corrosió de l'acer. Per això, s'han introduït les barres de polímer reforçat amb fibra (FRP) com una alternativa lliure de corrosió. L'interès creixent en aquesta tecnologia de reforç requereix comprendre la seva interacció amb el formigó. En conseqüència, en les darreres dècades s'han realitzat nombroses investigacions experimentals, així com models analítics i numèrics del comportament d'adherència. No obstant això, la manca de processos estandarditzats de deformació superficial i fabricació, juntament amb múltiples factors que influeixen en l'adherència, generen una gran variabilitat en les relacions esforç-lliscament entre diferents barres.

Per entendre millor aquestes variacions, aquesta recerca desenvolupa un model numèric a Abaqus per caracteritzar el comportament interfacial entre barres de polímer reforçat amb fibra de vidre (GFRP) indentades i formigó en assaigs de tracció. Es va crear un model axisimètric que requereix dades experimentals mínimes. La barra de GFRP es modela com a material linealment elàstic, mentre que el formigó utilitza el model de plasticitat amb dany per captar el seu comportament inelàstic.

La precisió i estabilitat s'aconsegueixen mitjançant la calibració rigorosa dels paràmetres del model constitutiu i detalls geomètrics, i anàlisis de sensibilitat sobre l'angle de dilatància, paràmetre de viscositat i coeficient de fricció. Finalment, es realitza un estudi paramètric per avaluar la validesa del model amb diverses geometries i diàmetres de barres.

Tot i que el model reprodueix la forma general de la corba esforç-lliscament després de la calibració, s'observa una sobreestimació constant de l'esforç màxim i discrepàncies en el lliscament respecte a les dades experimentals, especialment en barres de menor diàmetre. Aquests resultats evidencien la complexitat del comportament d'adherència GFRP-formigó i apunten a futures millores per augmentar la precisió predictiva en diverses aplicacions.

PARAULES CLAU: Adherència GFRP-formigó; Assaig d'extracció; Modelització per elements finits; Plasticitat amb dany del formigó.

Modelling of the Interfacial Behaviour between Fiber Reinforced Polymer Rebars and Concrete

ABSTRACT

Currently, steel reinforcement bars (rebars) are commonly used to reinforce concrete in tension. However, this introduces the possibility of concrete structure deterioration due to steel's corrosion. As a result, fibre-reinforced polymer (FRP) rebars have been introduced as a corrosion-free substitute. The increasing interest in using this reinforcement technology necessitates an understanding of its interaction with concrete. Consequently, extensive experimental investigations, as well as analytical and numerical modelling of the bond behaviour, have been carried out over the past decades. On the other hand, the lack of standardised surface deformation and manufacturing processes, as well as the many influencing factors on the bond behaviour, cause a lot of variations in bond stress-slip relationships among various rebars.

To gain a better understanding of these variations, this research aims to develop a numerical model using Abaqus to characterise the interfacial behaviour between ribbed/indented glass fibre-reinforced polymer (GFRP) rebars and concrete in pull-out tests. An axisymmetric model with minimal experimental data input required is developed for this purpose. GFRP rebar is modelled as a linear elastic material, while the concrete damaged plasticity model is used to capture the inelastic behaviour of concrete.

Its accuracy and stability are then improved through rigorous calibration of material constitutive model inputs and geometric details, and sensitivity analyses on various parameters such as dilation angle, viscosity parameter, and coefficient of friction. Finally, a parametric study was conducted to analyse the model's compatibility and validity across various ribbed rebar geometries and diameters.

While the model successfully captured the general shape of the bond stress-slip curve following the calibrations, a consistent overestimation of the τ_{max} and discrepancies in s_1 were observed when compared to experimental data, particularly for smaller diameter rebars. The findings underscore the complexity of GFRP-concrete bond behaviour and highlight areas for future model refinement to enhance predictive accuracy for diverse applications.

KEYWORDS: GFRP-concrete bond; Pull-out test; Finite Element Modelling; Concrete Damaged Plasticity.

TABLE OF CONTENTS

LIST OF FIGURES

LIST OF TABLES

LIST OF ABBREVIATIONS AND SYMBOLS

Abbreviations

ACI	American Concrete Institute
CDP	Concrete Damaged Plasticity
COF	Coefficient of Friction
EC2	EuroCode 2
EN	European Standard
FEM	Finite Element Modelling
fib	International Federation for Structural Concrete
FRP	Fibre-Reinforced Polymer
GFRP	Glass Fibre-Reinforced Polymer
LVDT	Linear Variable Differential Transformer
MC90	Model Code 1990
RC	Reinforced Concrete
Rebar	Reinforcement Bar
RILEM	International Union of Laboratories and Experts in Construction Materials, Systems and Structures

Symbols

α, β, p	Experimental curve-fitting parameter
d	Rebar diameter
d_c	Concrete damage in compression
d_t	Concrete damage in tension
D	Cylindrical concrete specimen diameter
E	Damaged elastic modulus of concrete
E1	Elastic modulus of FRP in longitudinal direction
E2, E3	Elastic modulus of FRP in transverse direction
E_{cm}	Initial elastic modulus of concrete
e	Plastic potential eccentricity

ε	Strain
	ε_c for compression
	ε_t for tension
ε_{c1}	Compressive strain in the concrete at the peak stress
ε_c^{in}	Inelastic strain in compression
$\varepsilon_{cu,1}$	Ultimate compressive strain in the concrete
ε^{pl}	Plastic strain
	ε_c^{pl} for compression
	ε_t^{pl} for tension
ε_t^{cr}	Cracking strain in tension
F	Applied load
f_{ck}	Characteristic axial compressive strength of concrete cylinder at 28 days
f_{cm}	Mean axial compressive strength of concrete cylinder
f_{ctm}	Mean axial tensile strength of concrete
G12, G13	In-plane shear modulus of FRP
G23	Out-of-plane shear modulus of FRP
K_c	Ratio of second stress invariant on the tensile meridian
L	Embedded length
μ	Viscocity parameter
ψ	Dilation angle
s	Slip
s_1	Slip at maximum bond stress
σ	Stress
	σ_c for compression
	σ_t for tension
σ_{b0}/σ_{c0}	Equibiaxial yield stress ratio
τ	Average bond stress
τ_{max}	Maximum bond stress
v_{12}, v_{13}	In-plane Poisson's ratio of FRP
v_{23}	Out-of-plane Poisson's ratio of FRP
η, k	Intermediate variable

1. INTRODUCTION

1.1. Motivation

Reinforced concrete (RC) is a widely used construction material in the world due to concrete's abundance, high strength, and ability to be cast into complex shapes [1]. However, concrete is largely limited by its lack of tensile strength, which is why reinforcement bars (rebars) have been used in different forms throughout the years, such as plain steel, deformed steel, and more recently, fibre-reinforced polymer (FRP) rebars [2]. Deformed steel is currently the most commonly used type of rebar, but its main challenge comes from corrosion, which leads to the deterioration of RC structures [3]. Hence, the corrosion of steel rebars causes a significant loss of durability and strength of RC structures and can result in their failure [3], [4]. With this issue being the main cause of RC structures' degradation, it demands consistent measures to be taken for their preservation and repair, therefore causing an ever-growing cost of maintenance [3], [5]. Consequently, FRP rebars have been increasingly used and studied in the last decades as a corrosion-free alternative for their steel counterparts in the construction field [6] - [8].

In addition to being corrosion resistant, FRP rebars possess the advantages of having higher tensile strength and strength-to-weight ratio, better fatigue resistance, lower maintenance costs, and higher speed of application in construction [4], [6], [8]. These give the FRP rebars a prospect of replacing conventional rebars in construction.

The increasing interest in application is complemented by an interest in researching the material's behaviour to better understand and design RC structures with FRP rebars [3]. One aspect that is critical to the implementation of these materials as reinforcement is their bond behaviour with concrete, as it controls serviceability, cracking behaviour, and ultimate capacity of RC members [8]. When considering RC structures with steel rebars, the reliability of the bond between the two materials guarantees they work well together. However, because of all the different surface treatments that FRP rebars can offer and their reduced axial stiffness compared with conventional steel ones, meeting serviceability limit state requirements becomes the driving design element in composite reinforced concrete parts [4], [7]. Therefore, it is important to understand the load transfer mechanisms, which affect the bond behaviour, between FRP rebars and the surrounding concrete, as bond properties govern a RC structure's durability [5].

FRP rebars are typically manufactured through the pultrusion process using long fibres and thermosetting resins as matrices, which offer durability in line with the RC structures' requirements. Then, surface treatment is done following the pultrusion process to enhance the bond characteristics of the rebar. Additionally, thermoplastic resin is being introduced as an alternative matrix material in the rebar manufacturing, offering the possibility of bending on-site and recycling at the end of the structure's life [9], [10]. As mentioned earlier, FRP rebars are manufactured with various surface configurations, such as sand coating, helical wrapping, ribbed, and indented rebars, in order to enhance their bond with concrete. Currently, there is no standardisation for the manufacturing process of these bars, unlike their steel counterparts. This introduces a lot of variability in the bond behaviour between the rebars and concrete, making the characterisation of their behaviours a crucial part of their structural usability before being commercialised [6], [7], [11]. However, this had also been the case for steel rebars in the early 1900s when there was no standardisation of yield grades and deformation patterns [12].

The mechanical interlocking of the bars and the friction between their surface and the surrounding concrete are the key components of the bond mechanism between FRP rebars and concrete [4]. In contrast to conventional bars, there is minor effect from the chemical bond between FRP bars and concrete, and it may be neglected [13]. This is because of the resin used to make FRP rebar, which has a water-repellent quality. Hence, rough or deformed surface treatments have been introduced as properties that provide greater mechanical interlock actions and friction [4], [13], [14]. The bond mechanism of FRP reinforcement is different from that of conventional steel reinforcement and is dependent on even more parameters. The primary variables taken into account in the assessment of the bond behaviour are bar diameter, embedment length, the modulus of elasticity of FRP bars, concrete strength, concrete cover, and bar surface treatment [11], [14] - [16].

Due to the variability of FRP rebars, numerous investigations on the variables influencing the bond performance of FRP bar-reinforced concrete have been carried out by researchers [4]. The hinged beam test and the direct pull-out test are the most widely used procedures for evaluating the bond behaviour of FRP rebars with concrete. The maximum applied load and the total slippage of the FRP rebar are the measured quantities during bond tests. The pull-out test described by the American Concrete Institute (ACI) 440.3R-04 [17], International Union of Laboratories and Experts in Construction Materials, Systems and Structures (RILEM) recommendations [18] and European Standard (EN) 10080 [19] is the most straightforward testing procedure for bonds and has been widely used by researchers to compare the effects of influencing factors and study failure modes of rebars embedded in concrete [20].

The two main bond failure modes in these tests are the pull-out and splitting modes. The splitting failure prevents the specimen from reaching the maximum load transfer capacity. Thus, short embedment lengths are commonly used, as well as sufficient concrete cover in bond tests to prevent this type of failure. Besides concrete splitting, concrete shear failure, rebar deformation peeling, and rebar squeeze-through are the other failure mechanisms that can be observed in bond tests [21].

The latter three all result in a pull-out failure mode, as can be seen in Figure 1.1, which shows the various failure modes and mechanisms. The shear failure of concrete primarily depends on the concrete strength and is similar to the behaviour of conventional reinforcement specimens illustrated in Figure 1.2. Crushing of concrete in front of rebar deformations and radial cracking of concrete dominate the failure mechanisms. However, due to the FRP rebars' low radial stiffness and interlaminar strength in the longitudinal direction, an increase in the concrete's shear strength does not always result in an increase in bond strength. The rebar surface deformation peel-off can occur as a result of the low shear strength between the rebar and the deformations. Meanwhile, the squeezing of FRP rebars could be observed through the concrete due to its low radial stiffness. Any of these failure mechanisms, or a combination of them, can govern the maximum bond strength of FRP rebars embedded in concrete [21]. Furthermore, different diameter bars having the same surface deformation and from the same manufacturer can display different failure mechanisms, adding to the complexity of their behaviour [22].

(a) Concrete splitting [23]   (b) Concrete shear-off [23]
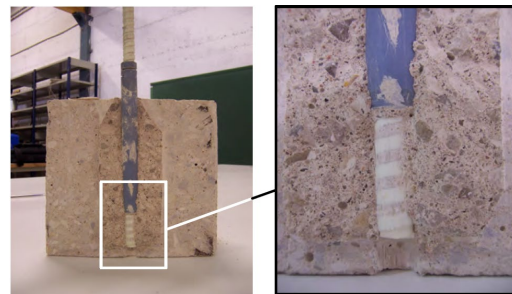
(c) Rebar surface deformation peel-off [24]

Figure 1.1: Failure modes and mechanisms of pull-out tests.
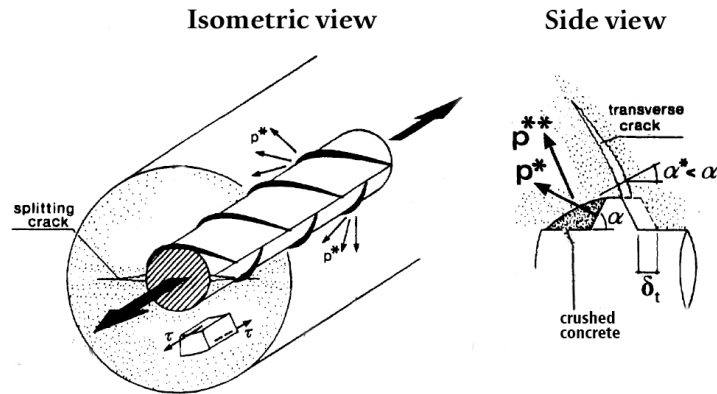
Figure 1.2: Concrete crushing and transverse cracking failure mechanisms during concrete shear failure. (adapted from [25])

In the literature, a number of analytical models have been developed to explain the bond-slip behaviour of rebars embedded in concrete. To gain a better understanding of the load transfer mechanisms between FRP bars and concrete under certain test configurations, numerical modelling based on the finite element method has also been carried out [26]. Distinguishing the effects of various material and geometrical characteristics on bond behaviour based solely on experimental results is challenging. Therefore, a reliable bond model is essential for gaining a deeper understanding of the underlying mechanisms. Moreover, experimental characterisation of materials is time-consuming and resource-intensive. As a result, numerical simulations are often employed to design and optimise testing procedures before conducting experiments. However, existing numerical models struggle to accurately predict bond behaviour across different bar configurations and influencing factors. This limitation means that key parameters of the bond model must be determined in advance and incorporated into the simulation database, typically using experimental data [27].

The two main levels of numerical modelling of the bond behaviour are (1) detailed modelling shown in Figure 1.3 (b), which uses 3-D elements to model the geometry of the bar and the concrete, and (2) phenomenological modelling shown in Figure 1.3 (c), which is based on a discrete or smeared formulation of the bar-concrete interface.

In phenomenological modelling, the bond is represented using discrete or zero-thickness cohesive elements governed by a bond stress-slip relationship, allowing realistic simulation with relatively low modelling and computational effort, provided that the bond parameters are predefined. However, this method cannot directly capture the influence of bar geometry. In contrast, detailed modelling involves explicitly representing the reinforcement ribs and surrounding concrete features, requiring a significantly higher modelling complexity and computation time [27], [28].

(a) Idealised bond zone. (b) Detailed modelling. (c) Phenomenological Modelling.
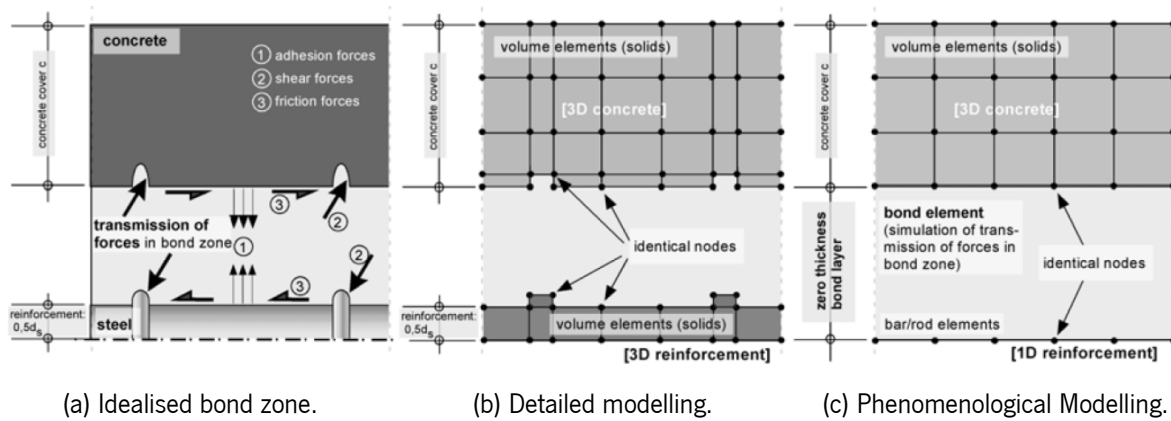
Figure 1.3: Schematic representation of the idealised bond zone modelling approaches [29].

1.2. Objectives

In this study, a state-of-the-art review will be carried out on the characterisation and the modelling of interfacial behaviour between FRP rebars and concrete, consisting of three parts: (1) existing experimental characterisation methods of the interface, (2) main analytical and (3) numerical models. The main question of the review will be to determine the methodology commonly used in the literature to capture the interface behaviour between FRP bars and concrete. The experimental and analytical models will be explored to study their accuracy and representativeness of structural RC members and experimental results. Numerical models used in the literature studying the bond-slip behaviour in pull-out tests will also be analysed based on the modelling space, material constitutive models, and interface modelling strategies.

Following the state-of-the-art review, a numerical model relying on the use of Abaqus finite element modelling (FEM) software [30] will be developed. The focus of the model will be on the characterisation of interfacial behaviour between ribbed/indented glass fibre-reinforced polymer (GFRP) rebars and concrete. The objective is to characterise this behaviour using minimal experimental input. In the end, the results of the numerical model will be assessed based on experimental investigations.

1.3. Structure of the Dissertation

The dissertation consists of six chapters. Chapter 1 provided the motivation and objectives of the dissertation, providing clarity for the upcoming study, while also outlining the structure of the dissertation. Chapter 2 presents a comprehensive review of existing experimental characterisation methods and analytical and numerical models for the interface between FRP rebars and concrete. This chapter aims

to identify the methodologies commonly employed in the literature to capture this interfacial behaviour, assessing their accuracy and representativeness of structural reinforced concrete (RC) members and experimental results.

Chapter 3 details the development of a numerical model using Abaqus [30] software. The model is developed with a focus on characterising the interfacial behaviour between ribbed/indented GFRP rebars and concrete, requiring minimal experimental data. It outlines the geometry, constitutive models for GFRP and concrete, and boundary conditions used in the pull-out test simulation.

Chapter 4 presents the initial results obtained from the numerical model and discusses the iterative development process undertaken to improve its accuracy and stability. This includes investigations into loading rate, mesh refinement, constitutive model calibration (tensile softening and compressive inelastic behaviours), geometric details calibration, and sensitivity analyses on various parameters such as dilation angle, viscosity parameter, mesh, and coefficient of friction.

Chapter 5 explores the model's compatibility and validity across various ribbed rebar geometries and diameters. This chapter investigates the influence of different bar geometries and diameters on the bond stress-slip relationship. It also examines the impact of GFRP elastic properties and concrete specimen dimensions on the model's predictions.

In the end, Chapter 6 summarises the main findings and conclusions drawn from the entire study. It highlights the limitations of the developed model and proposes avenues for future research and development, including potential extensions to 3D simulations and more refined material property definitions for rebar deformations.

2. STATE-OF-THE-ART REVIEW

The state-of-the-art review consists of three sections: the first section will focus on the experimental rebar-to-concrete bond characterisation methods, while the next section will focus on the analytical models in to estimate the bond behaviour, lastly, a review will be carried out on the numerical modelling strategies used in the literature, how well they represent the said experimental setups and their compliance with existing design guidelines.

Before starting the review, a timeframe in which the state-of-the-art review will be carried out is set by determining markers to define the timeframe. The timeframe is chosen between 2007 and the present with reference to the date of publication of the International Federation for Structural Concrete *(fib)* Bulletin 40 [21], which focuses on FRP reinforcement in RC structures.

2.1. Experimental Bond Characterisation Methods

Among the existing experimental characterisation methods used to analyse the interfacial behaviour between concrete and rebars are the pull-out, hinged beam, and direct tensile pull-out tests [21]. In general, these test setups involve a debonded area near the face of the pull-out to prevent the "edge effect" leading to failure in the concrete cone near the loaded end, as shown in Figure 2.1.
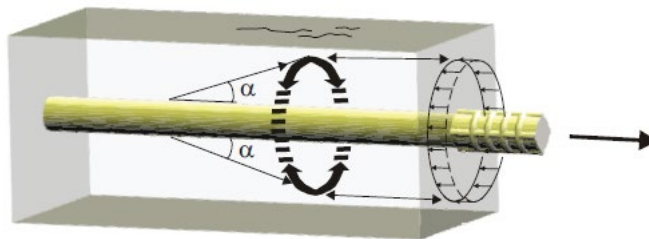
Figure 2.1: Concrete cone failure at the loaded end of a pull-out specimen [31].

Relative displacements between the rebar and concrete, known as the slip *(s)*, are measured at the loaded and free ends of the specimen using dedicated sensors in the test setup. The slip is then plotted against the average bond stress. The average bond stress (τ) is calculated by dividing the force from a load cell measuring the load carried by the rebar *(F)* by the total embedded surface area of the rebar using Eq. (2.1).

$$\tau = \frac{F}{\pi d L}$$

(2.1)

where: d is the rebar diameter, and L is the embedded length

Throughout the literature, pull-out and hinged beam tests are the most widely used in the characterisation of the bond behaviour between FRP rebars and concrete. Despite the former being unadvisable by ACI 408R-03 [32] to find the development length of rebars in concrete, it is valid for contrasting and characterising the bond performance of various concrete strengths and rebar types and sizes, and is more commonly used due to its simplicity [17], [33]. The pull-out test is also stated as a viable bond characterisation method by the *fib* Bulletin 40 [21]. The experimental set-ups of these characterisation methods are described in the following sub-sections.

2.1.1. Hinged Beam Test

The main advantage of using a beam test for bond characterisation is the replication of actual in-service stress conditions in the whole specimen [1], [7]. Since the hinged beam test aims to study the interfacial behaviour between the rebar and concrete, it aims to achieve bond failure in the rebar through pull-out, splitting, or the rupture of the rebar, the latter of which is less obtainable in FRP rebars. To ensure bond failure, two half-beams are cast, connected by a rebar in the bottom face and a steel hinge in the top face as shown in Figure 2.2. A debonded region of the rebar is added, typically using a pipe section, near the central hinge of the beam, to prevent the interaction of concrete and rebar in the loaded face, which helps in capturing the bond behaviour and failure more accurately. During testing, the slip of reinforcement is measured at the ends, typically using linear variable differential transducers (LVDT) as shown in Figure 2.2.

Figure 2.2: Hinged beam test set-up [1].

Another important aspect in obtaining the correct behaviour is the prevention of shear cracks with the use of transverse reinforcement as shown in Figure 2.3. Although several works have been developed without the use of stirrups in hinged beams [6], [7], this has caused issues with shear affecting the actual behaviour and resulting in lower bond strengths in certain specimens. Hence, if the use of stirrups is to be avoided, it is necessary that the beam is designed with enough shear resistance to avoid shear cracking, as was done in [7] with the use of high-performance fibre-reinforced concrete. Additionally, the use of stirrups shows that hinged beams are more challenging to prepare and test because of the extra effort and time required to prepare the reinforcement cage of the beams prior to casting [6].

Figure 2.3: An example of reinforcement cage and formwork before casting beams for testing [1].

To obtain the bond stress-slip relationship of the reinforcement, the readings from the LVDTs are used against the stress, which is processed from readings of a load cell during load application. In beam tests conducted for bond characterisation, the applied flexural load must be converted into the corresponding tensile force acting on the reinforcement. This conversion depends on the beam's geometry, support conditions, and the location of the applied load, as these factors influence the internal moment distribution and, consequently, the tensile demand on the embedded rebar [1]. The determined tensile load on the reinforcement is then converted to bond stress using Eq. (2.1) defined earlier, considering the total embedded length in both half-beams if the total load on the reinforcement is considered.

2.1.2. Pull-out Test

The pull-out test is one of the most common testing methods for studying the effect of various parameters on bond behaviour and has been performed since the 1940s [34]. Despite the beam tests being more realistic and representative of the in-service behaviour of reinforced concrete structures, especially flexural ones, the pull-out test is more efficient in terms of cost, handling, and curing before testing, as its specimens are smaller [6]. For these reasons, they are more frequently used by researchers in parametric

studies. Similar to the hinged beam test, the pull-out test aims to achieve bond failure through pull-out and splitting failure modes through pulling central and eccentrically placed rebars, respectively. Sufficient concrete cover is typically used to obtain a pull-out failure mode and avoid splitting failure in the case of the central test setup shown in Figure 2.4. Alternatively, concrete confinement has also been used to prevent longitudinal split cracks [25]. The collected outputs are also similar to the beam test, with the difference that the load readings from the load cell can be directly used in the calculation of the bond stress as a tensile load is being applied, as opposed to the flexural load of the beam test. However, when the displacement of the loaded end is considered, it is essential to subtract the portion of the slip that corresponds to the elongation of the rebar between the LVDT and the embedded point at the insulating pipe [35], [36].
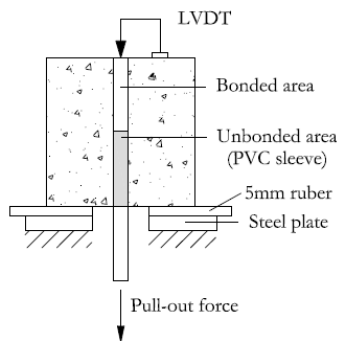
Figure 2.4: Pull-out test arrangement described in RILEM/ *fib* [23].

2.1.3. *Comparison of Testing Methods*

Among the characterisation methods, the beam test represents the actual performance of the FRP rebars in concrete members the best [8]. The influence of the characterisation method on bond behaviour has been investigated in [22], where pull-out, beam, and direct tensile test methods were compared. This comparison was done for several types of rebars as shown in Figure 2.5. It was found that the pull-out test yielded the highest maximum bond strength values, while the direct tensile test generally resulted in the lowest, except for one rebar type. Given that the beam test is the most accurate of the methods, this means the pull-out test generally overestimates the bond strength, while the tensile test underestimates it. The overestimation of the pull-out test is because the isostatic stresses from the supported face of the concrete affect the pull-out process by providing confinement to the rebars, increasing the maximum stress [7]. This brings up another drawback of the pull-out test set up: in practice, the concrete and rebar are undergoing the same stress type, either compression or tension, while in the pull-out test, when the

rebar is being pulled and is in tension, the concrete is in compression at the face where it is supported [33].
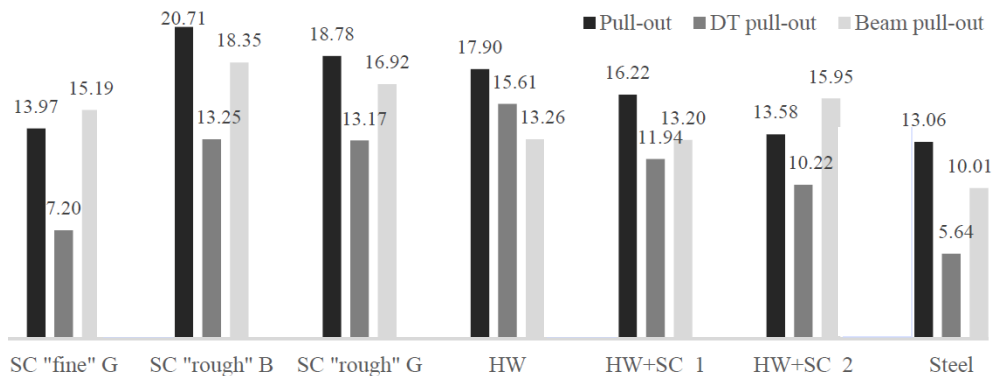
Figure 2.5: Comparison of different testing methods' bond strength results (in MPa) for various rebar materials and configurations [22].

Despite its limitations, the simplicity of the pull-out test favours its use by researchers, especially when extensive experimental programs such as the one in [37] are to be done. This can be attributed to the ease of preparation, as generally no stirrups are required, and the smaller size of its specimens when compared to hinged beams. The number of specimens prepared in the experimental programs by researchers implementing pull-out tests ranges from 24 to as high as 216 specimens, with an average of 64 specimens studied per test [4], [5], [14] - [16], [20], [24], [33], [35] - [39]. While this number is lower when looking into beam test programs, ranging from 11 to 36 beams with an average of 19 specimens per study [1], [3], [6] - [8], [11].

These bond characterisation methods for finding the average bond stress-slip relationships of FRP rebars in concrete have been adopted from the procedures used previously for the characterisation of steel rebars' bond behaviour [21]. Despite their adequacy, an interesting next step would be to develop an analytical method to relate pull-out test results to hinged beam test results. This would be challenging before a standardisation has been made to the manufacturing process due to the immense variability of FRP rebars among themselves [22]. As it is evident from the results of [22] in Figure 2.5, a consistent pattern does not exist between the results of the test setups, and the variation between bond strengths is significant even when the same surface category is compared in the same test setup. The development of this relationship, if successfully done, would help in obtaining realistic bond stress-slip relationships using pull-out tests, saving the extra effort and cost of conducting beam tests in the process.

2.2. Analytical Modelling of Bond Behaviour

The necessity to analytically model bond behaviour between FRP rebars and concrete comes in when considering the numerical modelling of the interfacial behaviour. Analytical models generate essential inputs for the understanding of the overall structural behaviour of structural members reinforced with FRP rebars in numerical simulation software. However, despite having numerous experimental programs studying this behaviour, not so many attempts have been published on analytical modelling [21].

An early analytical model describing the bond stress-slip law of FRP rebars in concrete was proposed in 1994 [40] using experimental data. Afterwards, the "Bertero, Popov, and Eligehausen (BPE) model" [41], best known for the definition of bond stress-slip law of steel rebars, was calibrated to represent FRP rebars instead [42], [43]. The original BPE model shown in Figure 2.6 consists of an ascending branch given by Eq. (2.2), a constant branch up to s_2, a linearly descending branch from (s_2, τ_1) to (s_3, τ_3), and a final constant friction plateau for $(s > s_3)$. However, when modified for FRP rebars, the plateau at peak stress is neglected based on experimental curves, and the authors proposed a modified "double branch model" shown in Figure 2.6. The ascending branch is still defined with Eq. (2.2) with the experimental parameter α varying with various rebars, whereas the value of 0.4 was used for steel. However, the descending branch is modified to be calculated through Eq. (2.3).
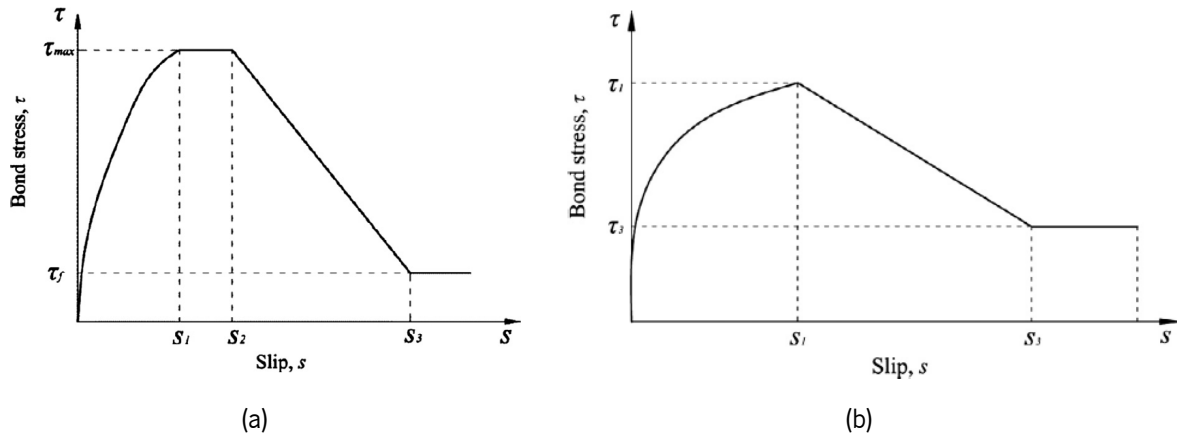
Figure 2.6: (a) BPE and (b) modified BPE models [44].

$$\frac{\tau}{\tau_1} = \left(\frac{s}{s_1}\right)^{\alpha} \qquad s \leq s_1 \qquad (2.2)$$

$$\frac{\tau}{\tau_1} = 1 - \frac{p(s - s_1)}{s_1} \qquad s_1 < s \leq s_3 \qquad (2.3)$$

where:
α is an experimental parameter less than 1 that determines the ascending branch.
p is an experimental parameter that determines the descending branch in the modified model.

12

Additionally, another model was later proposed in 1997 [45] known as the "Cosenza, Manfredi, and Realfonzo (CMR) model" that calculates the ascending branch only ($s < s_1$) using the constitutive law given in Eq. (2.4) instead.

$$\frac{\tau}{\tau_1} = (1 - e^{-s/s_r})^\beta \qquad\qquad s \leq s_1 \qquad\qquad\qquad (2.4)$$

where s_r and β are parameters based on curve-fitting of experimental data

This model was later calibrated based on additional experimental data, resulting in a new analytical model for the ascending branch given by Eq. (2.5) being proposed in [46], although it is believed that it comes with mathematical limitations [44], [47].

$$\frac{\tau}{\tau_1} = (1 - e^{4s})^{0.5} \qquad\qquad s \leq s_1 \qquad\qquad\qquad (2.5)$$

The modified BPE and CMR models have since been widely used in literature and were found to be more reliable in contrast with the model developed in 1994 [40] based on experimental results [47]. The *fib* has published a thorough analysis of each of these models' accuracy [21].

Moreover, authors have consistently been working to calibrate the experimental parameters to provide representative results using the analytical models [23], [47]. However, despite having vast populations of experimental results, the variability in the plots with the variation of surface finish, diameter, and concrete strength provides a significant challenge in the usability of these calibrated parameters [21], [47], [48]. Another path that researchers have taken to overcome this issue is proposing novel analytical models that take into account additional aspects like the characteristics of bond stress-slip curves such as the shape of the ascending branch [26], [49], [50], type and diameter of FRP rebar [48], [51], and influence of rebar geometry [16]. These models are aimed at representing the influencing factors discussed in the previous chapter instead of directly relying on experimental curve-fitting.

The model in [16] proposes two parameters, namely the rib area-to-space ratio (a_s) and concrete lug ratio *(CLR)*, as shown in Figure 2.7. Since the ribbed and indented rebars rely mainly on mechanical interlock, friction, and crushed concrete wedging, the rib geometry could be the main focus of the study to obtain a representative constitutive model. Despite the successful implementation of the models when compared to their respective experimental results, the models are still limited as the bond stress-slip behaviour can

vary between rebars of the same surface category with different surface finishes, diameters, or manufacturers [16], [47].
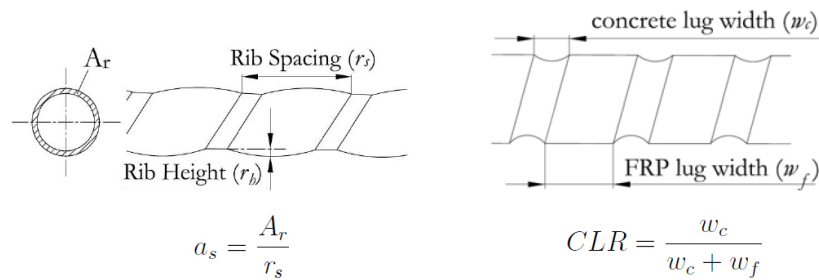
Figure 2.7: Parameters recommended in [16] to take into account rib geometry in the analytical model.

2.3. Numerical Modelling of Pull-Out Bond Behaviour

Numerous models have been developed throughout the literature to simulate the bond stress-slip behaviour in pull-out tests. These use various modelling strategies, which will be studied and contrasted through the review. It is important for the model to be able to capture the failure mechanisms described in the previous chapter, or for the results to show a resemblance in behaviour.

When it comes to numerical modelling, various aspects need to be studied carefully to obtain an accurate and representative model, such as part modelling, material properties, boundary conditions, and interactions [52]. Hence, the aspects that will be looked into in this section are the modelling space, material constitutive models for both the GFRP rebar and concrete, and interface modelling strategies. The modelling space mainly affects the computational time required and the damage pattern. Various material behaviours require different inputs and vary the captured failure mechanisms and patterns of the damaged material under the pull-out load [30]. The interface modelling strategy is crucial in determining the bond behaviour as it will directly represent the bond between the FRP rebar and concrete and how they interact. Similar to the material behaviour, different interface modelling strategies require different inputs.

2.3.1. Modelling Space

Several strategies can be found in the literature when looking at the modelling space used for pull-out tests, such as 2-D [31], [53], axisymmetric [27], [34], [54], and 3-D [13], [55], [56]. In the case of 3-D models studied, the complete test specimen can be modelled. Alternatively, truss elements can be used

for the rebar [49] or the symmetry (single or double) of the specimen can be taken advantage of [57] - [61].

The use of 2-D modelling is the simplest of the strategies listed. The main limitation in that case would be having a different interface area than the actual pull-out specimen. In [53], a fictitious third dimension is assumed to have an equivalent cross-sectional area of each material. A fictitious third dimension in terms of a planar 2-D model is the shell thickness assigned to the section. It is offset from the midplane and given a value such that the total cross-sectional area of each material is the same as that of the pull-out specimen. While this will be accurate in the case of material resistance, it will pose a challenge as the interface area will not be equivalent, and the bond-slip law would need to be calibrated in the model accordingly. This difference in the interface area using the fictitious third dimension can be illustrated by comparing a 2-D model and rendering the shell thickness with a complete 3-D model as in Figure 2.8 (a). The interface between the rebar and concrete in the bonded area is highlighted in red in the cross-section view. Using variables *(D)* and *(d)* for the diameter of the concrete and rebar, respectively, Figure 2.8 (b) shows that the interface area using the fictitious third dimension is half the actual area in the specimen, given that the embedded length is the same.
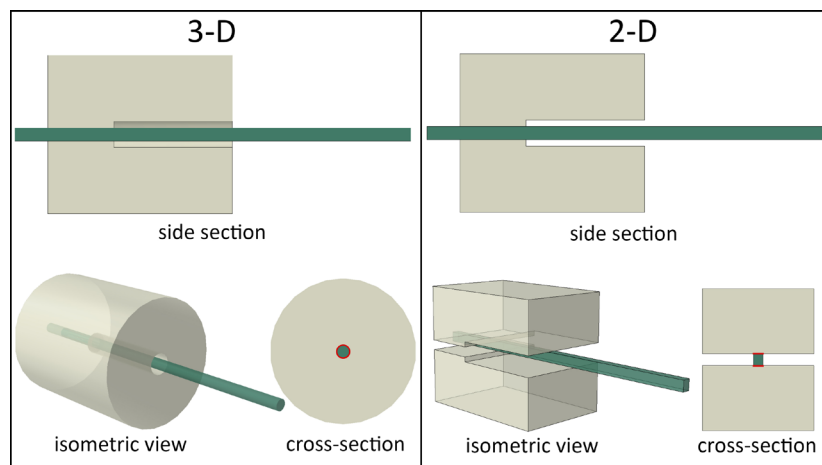
(a) Comparison of the complete specimen model and 2-D model with shell thickness rendered
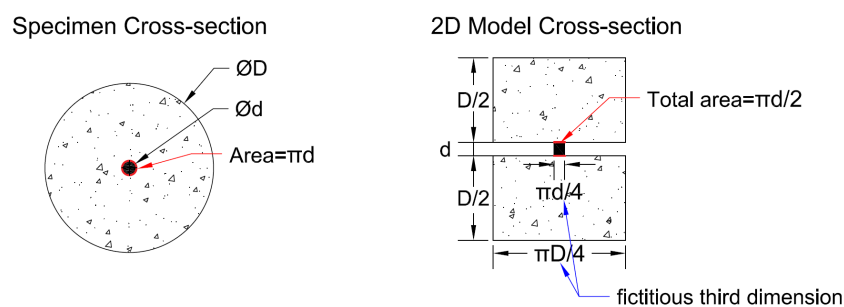
(b) Schematic comparison of the cross-sectional geometry of the two models

Figure 2.8: Comparison of the pull-out specimen's bond interface area with that of the simplified 2-D model.

Similar to 2-D modelling, axisymmetric model space provides a reduction in computational time and power required [27]. This modelling strategy has its limitations as well, as in the case of modelling pull-out specimens, only cylindrical specimens can be modelled as opposed to rectangular or eccentric test specimens, because they are not axisymmetric. To the best of the author's knowledge, axisymmetric modelling with a detailed modelling level of the interface has not yet been applied in the literature to simulate FRP rebars. Most existing studies using this approach have focused on steel reinforcement.

3-D modelling space, while providing the most accurate representation of the test setup, is the least efficient when it comes to the computational power required. Highly detailed models can also cause mesh generation and convergence issues, for instance, in the case of modelling the spirally wound ribs. Therefore, the spiral ribs are commonly simplified to a single circular winding pattern [13], [28]. Using full 3-D models of the test specimen is necessary when it has no symmetry, such as eccentric near-edge tests for splitting failure, particularly when the rebar is at the corner, as in [56].

As mentioned earlier, one of the methods used to improve the computational efficiency of the model is to use truss elements for the rebar. This strategy, however, prevents the possibility of modelling deformations in indented or ribbed rebars. This implies that the effects of mechanical interlock need to be included in the analytical model used for the interface, as it will be explained later on. Another strategy for improving the computational efficiency of 3-D models is the use of symmetry. Double symmetry can be employed when rebars are at the centre of the concrete specimen, while only a single axis of symmetry can be utilised in near-edge specimens [13], [56] or ones including bent bars [57]. This modelling strategy combines the ability to model detailed parts with reduced computational costs, making them a midway point between axisymmetric models and full 3-D ones [57].

2.3.2. *Material Constitutive Models*

In defining the constitutive models of the materials, different behaviours need to be considered for the GFRP and concrete based on their nature and the influencing factors that need to be captured by the model. Due to the GFRP rebars having linear elastic behaviour up to failure in the longitudinal direction and being anisotropic materials in their nature [13], linear-elastic properties are commonly defined by employing engineering constants without the necessity for defining failure stresses as it was not one of the modes of failure that were discussed [13], [49], [53] and in some cases simplified to isotropic materials [57] which means the effect of radial stiffness that is lower than the longitudinal stiffness is neglected. This latter approach simplifies the model and property inputs and could be useful in specific

scopes of work. Regardless, the use of engineering constants fits the modelling of pull-out tests on GFRP rebars better, especially if a squeeze-through behaviour is expected in the results.

Three constitutive models for modelling concrete damage are available in the Abaqus material library: (1) the brittle cracking, (2) smeared cracking, and (3) concrete damage plasticity (CDP) models [30]. Each of these models has its optimal use. In the case of pull-out tests, the CDP is the optimum constitutive model for concrete non-linearity. This is primarily because it accounts for both compressive and tensile non-linear behaviours, whereas the former two are most suitable for models where tensile cracking dominates the behaviour of the material and compression can be assumed to be linear elastic [62]. It is also the reason why CDP is very commonly used in the numerical modelling of pull-out tests in the literature where the researcher finds the behaviour of concrete essential for capturing the accurate mode of failure [13], [28], [34], [49], [54], [57] - [59], whereas in other cases the concrete behaviour was assumed linear when using phenomenological modelling level and bond behaviour was just considered in the constitutive models directly input [53], [55], [60]. The details of the brittle and smeared cracking models of concrete are elaborated in [62] and in the software documentation available online for reference [30].

The CDP relies on the definition of concrete's compressive and tensile behaviours in terms of stress with plastic strain or crack-opening displacement. The non-linear responses of concrete can either be obtained directly from experimental programs or analytical models such as the one proposed in Eurocode 2 (EC2) [63]. The main failure mechanisms associated with concrete using CDP are tensile cracking and compressive crushing, which are defined in a tabular form as pairs of cracking strain (ε_t^{cr}) and tensile damage (d_t), and inelastic strain (ε_c^{in}) and compressive damage (d_c), respectively [30]. Note that the terms "cracking" and "inelastic" are used when defining the plastic strains (ε^{pl}) in the different responses; the difference is only in the nomenclature to differentiate between the two behaviours, and their meaning is the same for their respective responses. The damage variable ranges from 0 to 1 and defines the stiffness degradation of concrete calculated in the software as shown in Figure 2.9.

In addition to these scalar isotropic damaged elasticity models, a non-associated flow rule is also defined as hardening plasticity with 5 variable parameters, the dilation angle (ψ), plastic potential eccentricity (e), equibiaxial yield stress ratio (σ_{bo}/σ_{co}), the ratio of second stress invariant on the tensile meridian (K_c), and viscosity parameter (μ). The five input parameters governing the CDP model's plastic flow and yield surface definition are essential for accurately capturing the complex inelastic behaviour of concrete under multiaxial loading. ψ controls the volumetric expansion associated with plastic flow, representing the
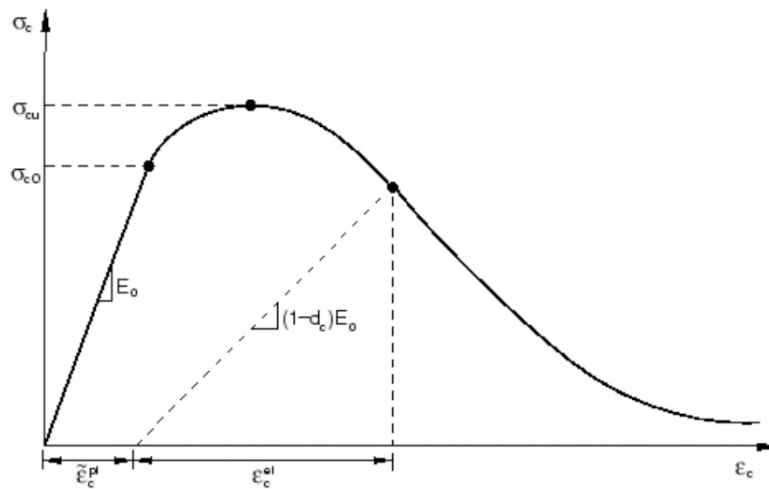
Figure 2.9: Concrete compressive behaviour and parameters described in the Abaqus documentation [30].

angle of inclination of the flow potential. Higher values (>40°) result in a more ductile response, while smaller angles (<20°) correspond to a more brittle fracture mode; this sensitivity has been extensively validated in numerical studies and experimental comparisons [59], [62], [64], [65]. The eccentricity defines the rate at which the plastic potential surface approaches its asymptote. It is typically set to 0.1 to maintain numerical stability and reflect the smooth nonlinear transition in concrete's inelastic regime [28], [34]. σ_{bo}/σ_{co}, often taken as 1.16, captures the enhanced strength of concrete under biaxial compression relative to uniaxial loading and is derived from consistent experimental evidence [58], [65]. The parameter K_c adjusts the shape of the yield surface in the deviatoric plane by controlling the ratio of the second deviatoric stress invariant on the tensile meridian to that on the compressive meridian. This parameter typically assumes a default value of 0.667 to reflect the tension-compression strength asymmetry inherent in quasi-brittle materials [54], [65]. Finally, the viscosity parameter serves as a regularisation factor in viscoplastic formulations, allowing for improved convergence in nonlinear simulations without significantly altering physical behaviour. ψ and μ vary among the models, with values between 30-40° commonly being used to define ψ. This range has also been proven in [62] to produce the best results in terms of concrete behaviour. Values of μ range widely (from 0.0001 to 0.67) depending on the modelling goals and loading rate sensitivity [58], [59].

2.3.3. Interface Modelling Strategies

With the advancement of FEM software, it is possible to facilitate their vast modelling solutions providing different levels of simulation complexities that enable researchers to choose different modelling strategies based on a balance between accuracy and computational efficiency [66]. On the other hand, this causes

18

dissimilarities in the developed models in different researchers' works. The available models use several interface modelling strategies such as spring elements [49], [53], surface-based contact [34], [57], [59], cohesive elements [55], [58], [67], rib modelling [13], or a combination of the last two [27], [28]. Each of these modelling strategies requires different inputs and provides challenges that might not be similar to the other strategies or even not suitable for all types of FRP rebars. The first three strategies have something in common, which is the need for input from experimental or analytical data to the law used in the interface elements, while the rib modelling relies on mechanical interlock through friction and material behaviours of the GFRP and concrete. The following sub-sections present the details required for understanding each of the interface modelling strategies listed above.

2.3.3.1.   Spring Elements

Both spring elements and translator elements are used similarly in the literature to model the bond interface. Spring elements can be used to connect node-to-ground (Spring1) or node-to-node (Spring2/SpringA) [30], with the latter being used in the models. They provide the advantage of being able to input pairs of force to relative displacement, which can be used with any analytical model but is particularly useful when self-developed models are simulated, as in [49]. The inputs for a non-linear load-displacement behaviour are given with ascending relative displacement to the software in the following format;

*spring, elset=[name], nonlinear
u_1, $F(u_1)$
0, $F(0)$
u_2, $F(u_2)$
...

Where negative values represent compression and positive values represent tensile forces, and at the end of the set, the software assumes a zero stiffness [30]. In the case of the interface, the zero-stiffness continuation can represent the bond failure and the load provided by friction during pull-out. Figure 2.10 shows the representation of the non-linear spring behaviour definition.

As discussed earlier, the Spring2 elements connect node-to-node in the different parts of the model. This implies that the use of these elements will cause stress concentrations in the node on which it is used, as is evident in the results of [53] in Figure 2.11.
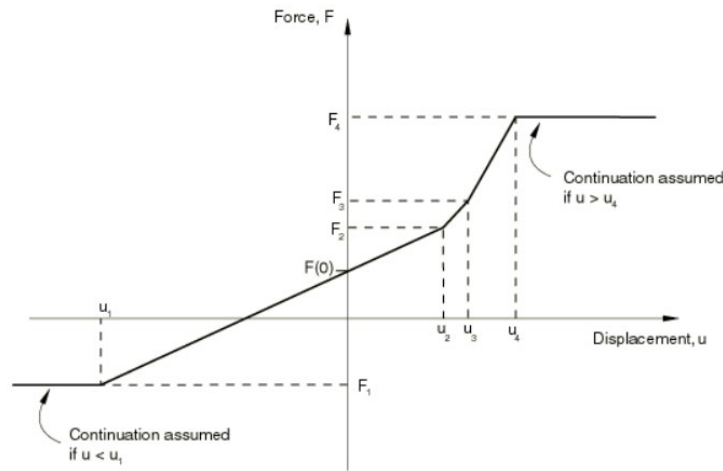
Figure 2.10: Non-linear definition of spring elements [30].
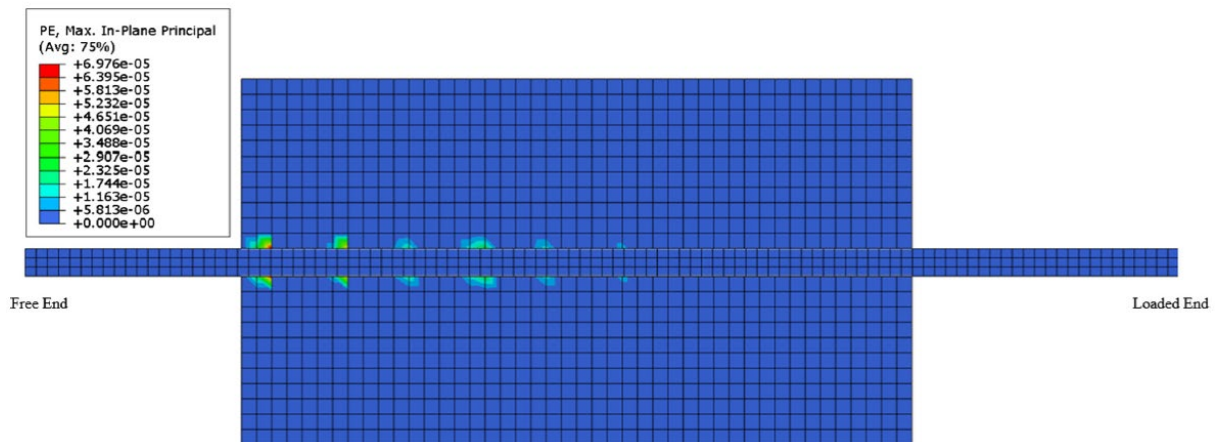
Figure 2.11: Stress singularities in mesh elements around spring elements [53].

The more elements are used, the less severe the singularity will be, as each spring element accounts for an equal fraction of the applied force divided by the number of elements, but at the same time, the required computational effort increases. This stress concentration means that the concrete behaviour cannot be accurately captured. On the other hand, this localisation of stress transfer could be used as an advantage in the modelling of ribbed rebars, where the spring element would represent the point of contact between the lugs and the bearing concrete. Similar to the models already in use, this will require calibration and sensitivity analysis of the spring element inputs as discussed in [53]. To do so in that study's specific case, the stress at the plateau and displacement at which the plateau starts were kept constant when defining the traction-separation relationship for the spring elements while varying the peak stress value as shown in Figure 2.12 to fit the results to the experimental ones. While this strategy saves a lot of computational power through the simplification of the bond interface, it comes at the cost of stress localisations and the requirement of experimental results for calibration.
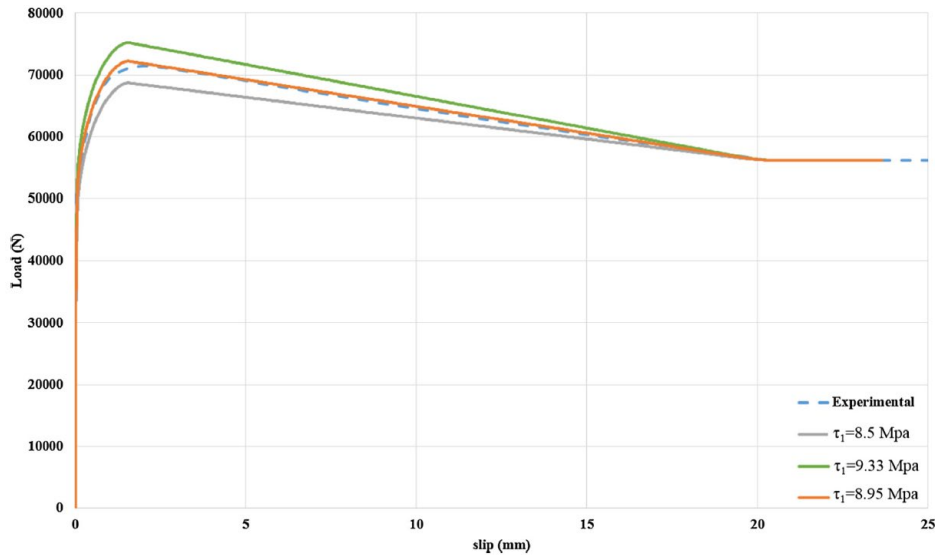
Figure 2.12: Sensitivity analysis done in [53] on peak stress value while keeping the plateau value constant.

2.3.3.2. Surface-Based Contact

Another interface modelling strategy is using surface-to-surface contact between the GFRP rebar and the concrete surrounding it. In this strategy, cohesive behaviour is defined between the two surfaces through the traction-separation law of the software, where traction is interpreted as bond stress and separation as slip [34]. To capture a similar behaviour to experimental programs, the parameters that define the cohesive behaviour, damage initiation, and evolution in the interaction properties are defined according to calibrated bond stress-slip laws [57]. A calibrated traction-separation law using linear damage evolution is shown in Figure 2.13. This calibration is done by keeping the maximum bond stress (τ_{max}) and slip at that stress (s_1), as they are in the experimental results. Then, the damage evolution is defined such that the fracture energy is equivalent to the energy dissipation of the bond stress-slip law. The calculations and definition of various parameters in the traction-separation law are discussed in detail in [59].
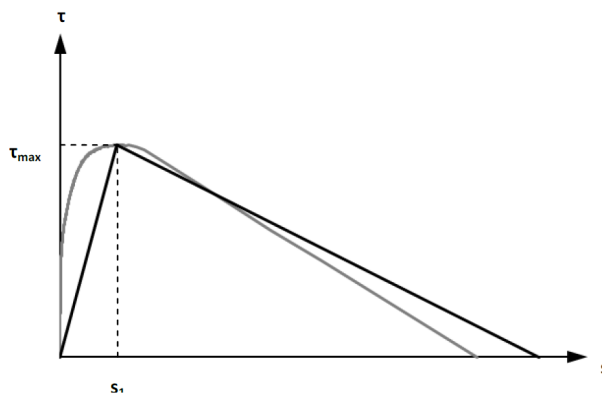
Figure 2.13: Approximation of the real bond-slip relation, shown in grey, with a traction-separation law, shown in black, such that each curve has the same area under it [59].

Other approaches include the adjustment of maximum bond stress due to the non-linearity of the bond stress-slip law near the peak stress [57], or the use of tabular damage evolution instead of linear to better fit the experimental results [34]. Both this and the previous strategy need existing experimental pull-out curves and calibration of the parameters to fit the software's available models. This can be useful when modelling the bond of a certain tested GFRP rebar in various concrete members is required, but inefficient for bond characterisation [13]. This is because the same model cannot be used for any rebar other than the tested ones due to the variability of the bond behaviour with many factors, for instance, the bar diameter, which adds to the complexity of modelling this behaviour. To elaborate, the peak stress and post-peak behaviour of the same rebar and concrete strength can vary with the bar diameter, even if it is from the same supplier [16].

2.3.3.3.   Cohesive Elements

An additional strategy that also relies on the input of experimental data, parameter calibration, and cohesive behaviours [55] is the use of cohesive elements, which is another type of special element in Abaqus next to the spring elements discussed before [30]. This strategy is similar to the previously discussed surface-based contact. However, instead of allowing direct contact between the two surfaces, a transitional element is introduced. This transitional element consists of cohesive elements placed between the surfaces. These cohesive elements function as an adhesive layer within which the cohesive behaviour and damage parameters are defined. Both of these methods have the advantage of distributing the bond stress across the entire surface over the spring elements strategy, preventing the occurrence of the aforementioned stress singularities [55].

This kind of special element is intended for use as a negligibly thin layer of adhesive when modelling the delamination of composites, along with the traction-separation law discussed in the previous sub-section [28], [30]. The main difference between using surface-based contact and cohesive elements in Abaqus is that surface-based contact models the interaction between separate surfaces with defined contact properties, while cohesive elements explicitly simulate the bond or interface behaviour between connected materials within zero- or finite-thickness elements. In the case of modelling pull-out tests where the same traction-separation law is used for both, the difference is that cohesive elements are mesh-dependent, while surface-based cohesive contact is mesh-independent and more geometrically flexible. Hence, a surface-based contact modelling strategy offers more flexibility in modelling contact between separate bodies [30].

2.3.3.4.   Rib Modelling

The previous modelling strategies are a phenomenological level of modelling the bond behaviour between rebars and concrete, and their behaviour is controlled by a predefined bond stress-slip law. This means that they are only able to predict the behaviour realistically if the parameters defining the bond model are input with reference to their experimental results [27]. However, modelling the bar's rib geometry is considered a detailed modelling approach that relies mainly on the mechanical interlock and the constitutive models of the materials defined [13].

Further, the main definitions in the interactions module are the normal and tangential behaviours, for which "hard contact" and a "coefficient of friction" (COF) of 0.5, respectively, are used in the literature [13], [57]. In the case of modelling the interfacial behaviour of steel rebars with concrete, cohesive layers are often used in conjunction with the rib modelling strategy as there is a certain level of chemical bond that affects the behaviour [27], [28]. This is not the case when modelling GFRP bars, as the effect of chemical adhesion is negligible [13]. The lack of bond is evident from the results of experimental pull-out test programs involving plain GFRP rebars, where no concrete residue can be seen on non-sand-coated rebars (Glass-NS) as opposed to sand-coated ones (Glass-S) in Figure 2.14.

Table 2.1 summarises the articles and their modelling strategies, showing the modelling space and interface modelling strategy used by their authors, as well as the type of concrete and rebars they studied.

Figure 2.14: Pull-out failure results for GFRP rebars with (S) and without (NS) sand coating [26].

Table 2.1: Summary of reviewed modelling strategies.

Reference	Year	Concrete Strength [MPa]	Rebar Material	Rebar Surface Configuration	Model Space	Interface Modelling Strategy
[49]	2019	32.6	Basalt, glass, carbon, and steel	Helical wrapping, sand coated, and screw thread	3-D	Spring elements
[53]	2017	-	Glass	Helical wrapping with sand coating	2-D	Translator elements
[34]	2022	43.5	Steel	Deformed	Axisymmetric	Surface-based contact
[57]	2022	25.3	Glass	Fibre-wrapped, sand-coated, and ribbed	3-D (one symmetry)	Surface-based contact
[59]	2015	27.3	Steel	Deformed	3-D (double symmetry)	Surface-based contact
[67]	2010	30	*FRP*	-	2-D	Cohesive elements
[55]	2020	154, 204	Carbon and steel	Ribbed and deformed	3-D	Cohesive elements
[58]	2017	23.3, 56.3	Glass	Ribbed	3-D (one symmetry)	Cohesive elements
[13]	2024	22.8, 44.2	Glass	Ribbed	3-D	Rib modelling
[27]	2009	30	Steel	Deformed	Axisymmetric	Rib modelling + Cohesive elements
[28]	2015	30	Steel	Smooth, deformed, and galvanised	3-D (double symmetry)	Rib modelling + Cohesive elements

From the analytical and numerical models, it can be observed that the current state involves models that represent individual rebar types. The developed models are based on experimental studies by each author, fitted for a specific population of results. Hence, these models are limited, with no variables that can be changed to use the model for other rebars [13], especially since even the manufacturing process varies the rebar properties [21]. It is difficult to have a representative analytical or numerical model for all types of rebars without experimental curve-fitting parameters, as FRP rebar manufacturing and surface deformations are yet to be standardised [22]. In the scope of numerical modelling, a possible step forward is developing a model that will be able to characterise rebars without direct experimental data input. However, this can only be realistically attempted with individual models exclusive to each surface configuration due to the variability among the failure mechanisms of different configurations.

3. NUMERICAL MODELLING OF PULL-OUT TEST ON GFRP REBARS

As studied in the previous chapter, despite having several models that have been developed before, many of the authors rely on the input of experimental stress-slip data in cohesive behaviour models. This approach, while effective for the rebars they were calibrated for, is limited and cannot be expanded to other rebars. The aim here is to develop a model using Abaqus that will be able to predict the bond stress-slip behaviour of GFRP bars embedded in concrete using minimal test data from the rebar and concrete. Due to the lack of standardisation and the high number of influencing factors, it would be difficult to develop a model that would characterise the bond behaviour of all surface configurations. Hence, the focus will be on the modelling of ribbed/indented GFRP rebars in concrete, as their failure mechanism relies mainly on mechanical interlock and friction between the rib projections and concrete, which can be modelled on a direct modelling level.

Axisymmetric modelling space will be used due to its computational efficiency. However, this will limit the model to centrally embedded reinforcement and will potentially need to be transformed into a 3-D model if eccentric specimens are to be modelled. Moreover, it will result in a circular winding pattern as opposed to a spiral one for the surface deformations, which is also a common simplification in 3-D models. In terms of material constitutive models, GFRP rebars will be defined as linear elastic using engineering constants. While the CDP model will be used to define the material non-linearity and damage evolution of the surrounding concrete. Abaqus/Explicit solver will be used in the simulations due to material non-linearities involved in the concrete's constitutive model. This will provide more stable solutions in addition to providing the possibility of stabilising the load application rate if needed through the use of amplitude curves [30].

3.1. Reference Geometry and Experimental Basis for GFRP Rebar Modelling

A ribbed GFRP rebar surface geometry was required to start developing the model. One such geometry was obtained from [68], where it is explicitly described. Moreover, the article chosen includes three different ribbed GFRP rebar types shown in Figure 3.1 with diameters of 6-, 8-, 10-, 12-, and 14-millimetres (mm). This is particularly advantageous, as it provides a comprehensive set of experimental results against which the developed model can be validated. The availability of multiple rebar geometries and diameters allows for a more robust assessment of the model's adaptability and accuracy across varying configurations.

25

Figure 3.1: Three surface types of GFRP rebars investigated in [68].

The schematic drawing of the rib dimensions is shown in Figure 3.2, with the respective variable values used in the numerical model shown in Table 3.1. The units used in the modelling process are Newtons (N) and mm. Note that the modelled rib spacing is 16.8 mm instead of the 10 mm reported in [68]. This simplification reduces the number of rib projections in the bonded area, thereby decreasing the number of interaction points between the rebar and concrete, and ultimately lowering the computational cost of the simulations. Additionally, the increased rib spacing enhances the visualisation of concrete crushing between the lugs.
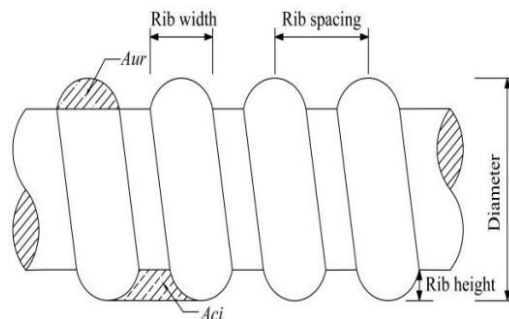
Figure 3.2: Schematic description of the rib geometry modelled [68].

Table 3.1: Modelled rib geometry dimensions.

Rebar Type	Diameter (mm)	Rib Width (mm)	Rib Spacing (mm)	Rib Height (mm)
S3	14	6.8	16.8	1.5

At this stage, only the rib geometry has been adapted from the experimental reference and incorporated into a simplified model. Once the model has been sufficiently developed and demonstrates behaviour that is representative of the overall response described in the preceding chapter, the material properties, rib spacing, and concrete dimensions will be adjusted to match those reported in [68] for more accurate

simulation and validation. The geometric dimensions and material properties of the simplified model are described in the subsequent sections.

The experimental stress–slip relationships corresponding to the three surface configurations shown in Figure 3.2 are presented in Figure 3.4. While all specimens exhibited a pull-out failure mode, a notable variation in τ_{max} is observed among the D14 specimens across the different surface configurations. This variation presents an important opportunity for investigation within the numerical model, as it allows for the evaluation of the model's ability to replicate the influence of different rib geometries on bond performance.

(a)

(b)

(c)
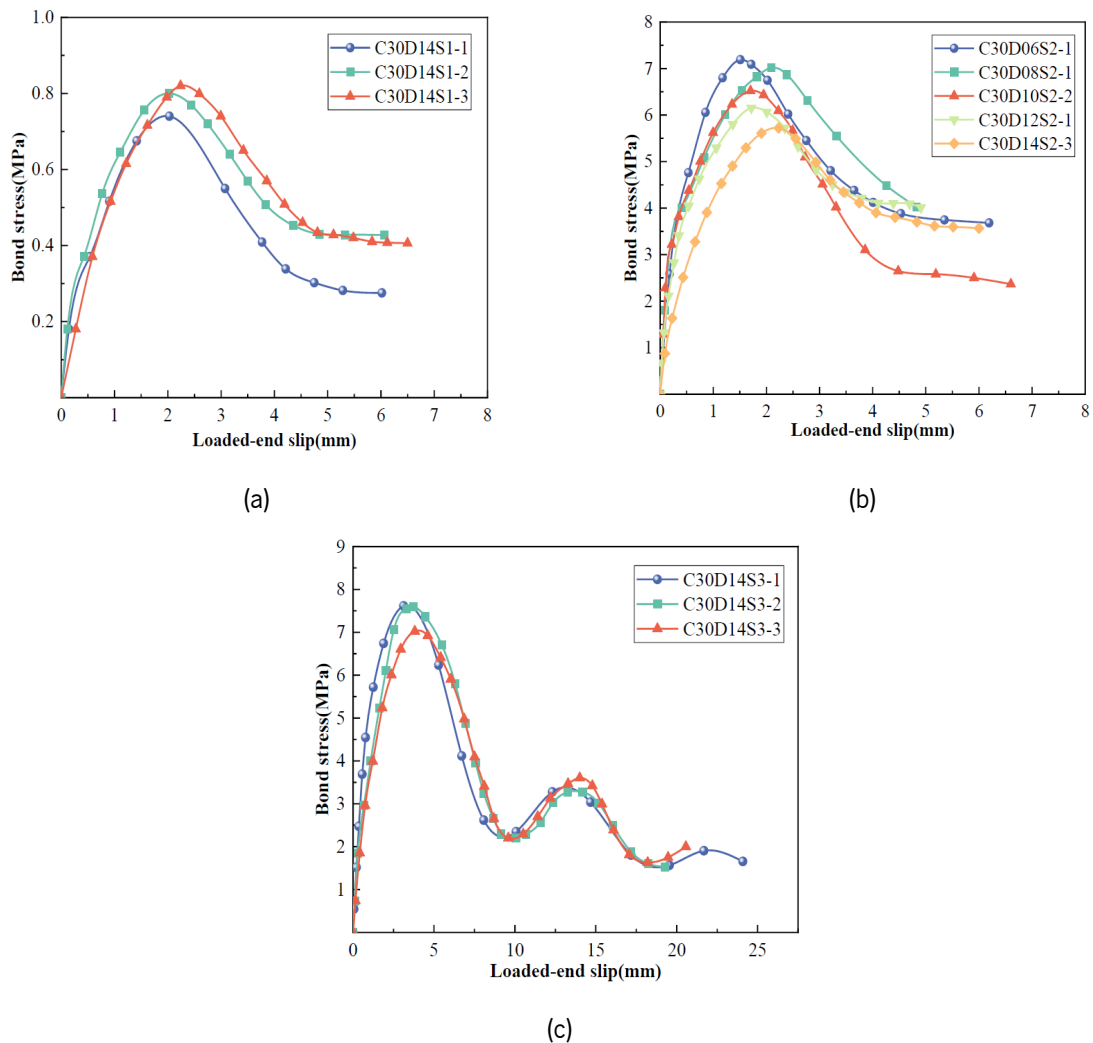
Figure 3.3: Bond stress-slip curves of specimens (a) S1, (b) S2, and (c) S3 with various diameters (D06-D14) and concrete strength class of 30 MPa (C30) [68].

3.2. Geometry

The assembly in Figure 3.4 shows the geometry used to model the pull-out test configuration. The unbonded region can be seen near the top with a bonded region having a length of 70 mm, which is 5d, the same value used in [68], based on ACI 440.3R-04 [17] recommendations. The modelled concrete specimen is a cylinder with both a height and a diameter of 200 mm. A partition was made near the centre of the cylinder where the GFRP is embedded to be assigned a finer mesh to capture the stress variations that occur in that region more accurately [57]. A global mesh size of 5 mm and a local seed size of 1.7 mm were used with structured mesh controls as shown in Figure 3.4. The 1.7 mm local size was used to have a greater value than the rib projection and to avoid too much mesh distortion near the ribs. The ribs of the rebar were also assigned a local seed by number to generate a more structured mesh. The geometry was modelled in the global x-y plane, with the symmetry axis shown as the yellow dashed line in Figure 3.4 being the line $(x = 0)$.
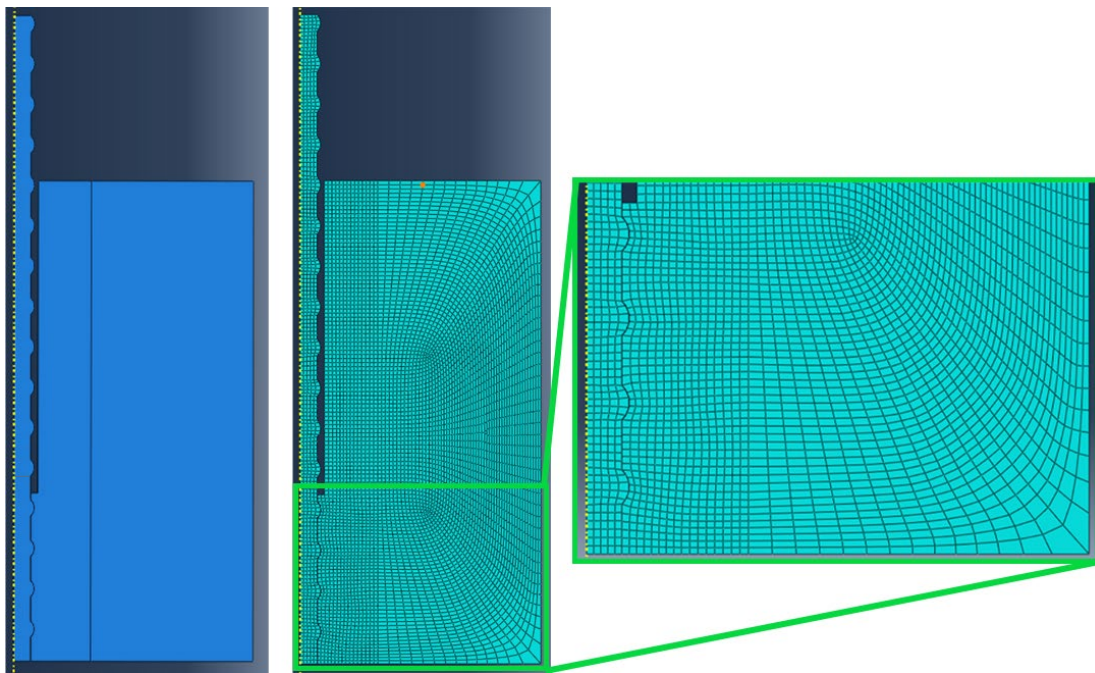
Figure 3.4: Complete model assembly and mesh structure.

3.3. Constitutive Models

The elastic material properties of the GFRP rebars used in defining the engineering constants were assumed as the ones listed in Table 3.2. Axis 1 in the table is the local axis of the rebar in the longitudinal direction. The selected parameters reflect representative mechanical properties for GFRP rebars used in

structural applications. The elastic properties used for GFRP rebars in the numerical model were selected based on values reported in the literature and manufacturer specifications. The longitudinal, transverse, and shear moduli adopted are consistent with commonly reported ranges from manufacturers [69] - [71]. Poisson's ratios were taken from published studies [72], as these values are typically not specified by manufacturers.

Table 3.2: Engineering constants input in elastic properties of GFRP.

E1 (MPa)	E2 (MPa)	E3 (MPa)	v_{12}	v_{13}	v_{23}	G12 (MPa)	G13 (MPa)	G23 (MPa)
36900	10000	10000	0.32	0.32	0.37	3300	3300	3900

The mean compressive strength of concrete (f_{cm}) is assumed to be 33 MPa, and the material properties and inelastic compressive behaviour are obtained analytically following the provisions of EC2 [63]. The elastic modulus of concrete (E_{cm}) was calculated according to Eq. (3.1), and the Poisson's ratio was assumed as 0.2.

$$E_{cm} = 22(f_{cm}/10)^{0.3} \tag{3.1}$$

where E_{cm} is in GPa and f_{cm} is in MPa

The concrete compressive behaviour shown in Figure 3.5 (a) is described in EC2 as having a linear elastic branch up to $0.4f_{cm}$, and a non-linear inelastic branch onwards, which will be input in the CDP data [63]. Tabular data starting from the compressive strain at $0.4f_{cm}$ ($\varepsilon_{c,1}$) up to $\varepsilon_{cu,1}$ in 0.0001 strain intervals were calculated using Eq. (3.2) through (3.5) to obtain the final curve shown in Figure 3.5 (b). Moreover, the mean tensile strength of concrete (f_{ctm}) was calculated using Eq. (3.7) [63].

$$\varepsilon_{c1}(‰) = min\left(0.7f_{cm}^{0.31}, 2.8\right) \tag{3.2}$$

$$k = 1.05 \cdot E_{cm} \cdot |\varepsilon_{c1}|/f_{cm} \tag{3.3}$$

$$\eta = \varepsilon_c/\varepsilon_{c1} \tag{3.4}$$

$$\frac{\sigma_c}{f_{cm}} = \frac{k\eta - \eta^2}{1 + (k-2)\eta} \tag{3.5}$$

$$\varepsilon_{cu,1}(‰) = \begin{cases} 3.5, & f_{cm} \leq 58 \\ 2.8 + 27[(98 - f_{cm})/100]^4, & f_{cm} > 58 \end{cases} \tag{3.6}$$

$$f_{ctm} = \begin{cases} 0.3 \cdot f_{ck}^{(2/3)}, & f_{cm} \leq 58 \\ 2.12 \cdot \ln\left(1 + f_{cm}/10\right), & f_{cm} > 58 \end{cases}$$

(3.7)

where:

E_{cm} is in GPa, and f_{cm} is in MPa

k and η are intermediate variables

f_{ck} is the characteristic concrete compressive strength in MPa, equal to (f_{cm} - 8)
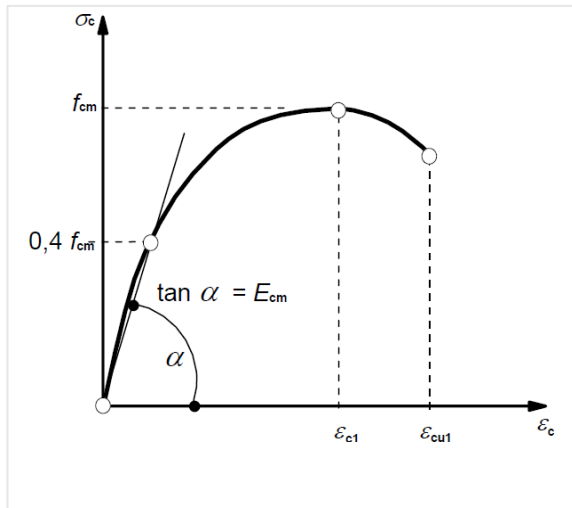
(a) Code schematic [63]
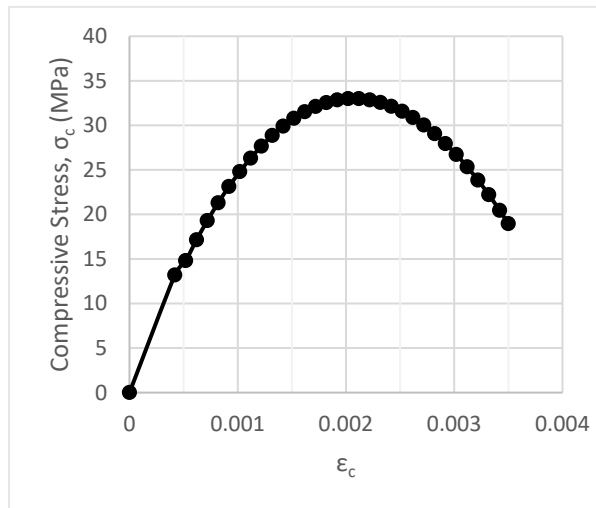
(b) Calculated result for f_{cm} = 33 MPa

Figure 3.5: Compressive behaviour representation of concrete in EC2.

The inelastic tensile behaviour was calculated following a simplified model from [73] shown in Figure 3.6 (a). The value of f_{ctm} obtained previously from Eq. (3.7) was used, and the points were calculated to obtain the relationship shown in Figure 3.6 (b).
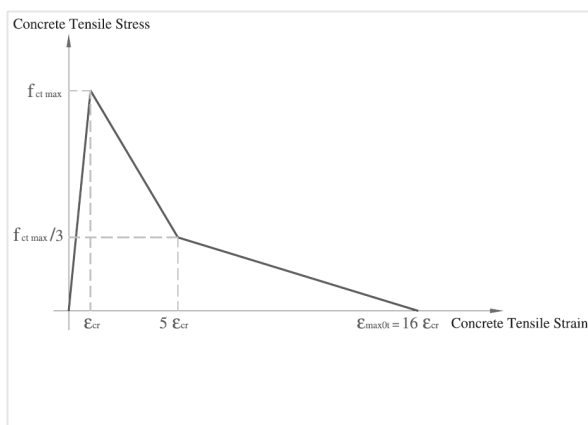
(a) Analytical model
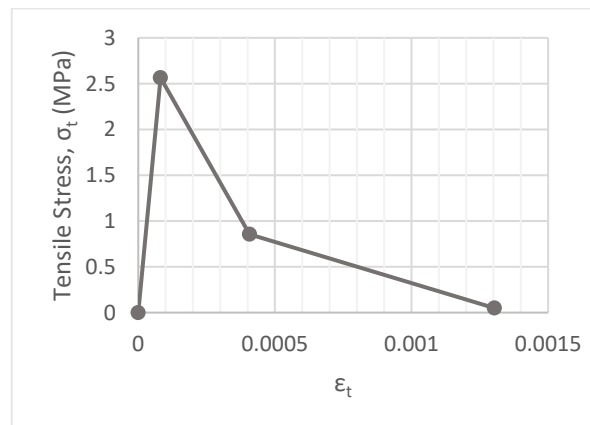
(b) Calculated result for $f_{ct,max}$ = 2.56 MPa

Figure 3.6: Simplified analytical model for tensile softening behaviour in [73].

The values of ε_0^{el} and ε^{in} were calculated using Eq. (3.8) and (3.9), respectively, as the inelastic behaviour input requires yield stress (σ) at various points and their respective ε_c^{in}. The damage parameter (d_c) is given by Eq. (3.10) as the stiffness degradation of the material with a value between 0 and 1. Note that the subscript (c) stands for compression in the following equations. In the case of tensile behaviour, the calculations are identical using tensile stress-strain values and the inelastic strain is named cracking strain (ε_t^{cr}) [30]. The Abaqus documentation [30] recommends using a maximum damage value of 0.99 to avoid numerical errors.

$$\varepsilon_{c0}^{el} = {\sigma_c}/{E_{cm}} \qquad (3.8)$$

$$\varepsilon_c^{in} = \varepsilon_c - \varepsilon_{c0}^{el} \qquad (3.9)$$

$$d_c = 1 - (E/E_{cm}) \qquad (3.10)$$

where:
σ and ε are the stress and strain values at each point, respectively.
E is the degraded stiffness value at each point.

However, cyclic loading test for the used concrete is required to obtain this data, and in the absence of such data, an approximation can be made where ($E = \sigma_c/\varepsilon_{c0}^{el}$) and ($E_{cm}=f_{cm}/\varepsilon_{c0}^{el}$). Substituting these values in Eq. (3.10) results in Eq. (3.11), which will be used in subsequent calculations.

$$d_c = 1 - (\sigma_c/f_{cm}) \qquad (3.11)$$

Even though this analogy is accurate for the case of concrete in tension, it is merely an approximation for the compressive behaviour. Finally, the plastic strain (ε^{pl}) was calculated using Eq. (3.12) to make sure they are positive and increasing with increasing inelastic strain. Otherwise, it is an indication that the damage data is incorrect, causing an error message by the solver to show [30].

$$\varepsilon_c^{pl} = \varepsilon_c^{in} - \frac{d_c \cdot \sigma_c}{(1 - d_c) \cdot E_{cm}} \qquad (3.12)$$

Annex I presents the results of these calculations, along with the input parameters used for the CDP model. Inputs for subsequent iterations will also be included in the annex if they differ.
It is possible to use the CDP with an extra function, which is *Concrete Failure. This function defines the complete failure strain and damage for concrete in tension and compression, as it is currently not defined

by default from the interface inputs. This function will also trigger element deletion when activated if element deletion is enabled in the element controls. It is necessary to edit keywords in the model's input file, which can be accessed from the model tree section of the interface. Figure 3.7 shows an example of the function used in the model, including the maximum values of ε_t^{cr}, ε_c^{in}, d_t, and d_c input for the specific case of the current model. Furthermore, this function requires inelastic strain values, which is why the tensile softening model from EC2 was avoided, which relies on fracture energy and crack opening calculations. That would require the inelastic tensile behaviour to be input in terms of yield stress and displacement in the CDP, which is possible but would cause complications when using the concrete failure function. Finally, the values for plasticity parameters in Table 3.3 were defined considering the default values discussed in the previous chapter.

```
*Concrete Tension Damage
     0.,      0.
   0.6667, 0.000380287
  0.980507, 0.00130225
*Concrete Failure, Type=STRAIN
   0.00130225, 0.00289795, 0.980507, 0.425759
```

Figure 3.7: CDP input functions in the model keywords.

Table 3.3: Constitutive parameters of concrete plasticity.

ψ	e	σ_{b0}/σ_{c0}	K_c	μ
35°	0.1	1.16	0.667	0.0001

3.4. Boundary Conditions

To simulate the pull-out test set-up described earlier, the top edge of the concrete cylinder was constrained in vertical displacement and rotation (U2=0, UR3=0) as shown in Figure 3.8. The node on the top left corner highlighted in the figure was assigned a horizontal constraint (U1=0) as well. A displacement of 10 mm was also applied at the top of the rebar in Step-1 (standard, explicit) to simulate a displacement-controlled loading.
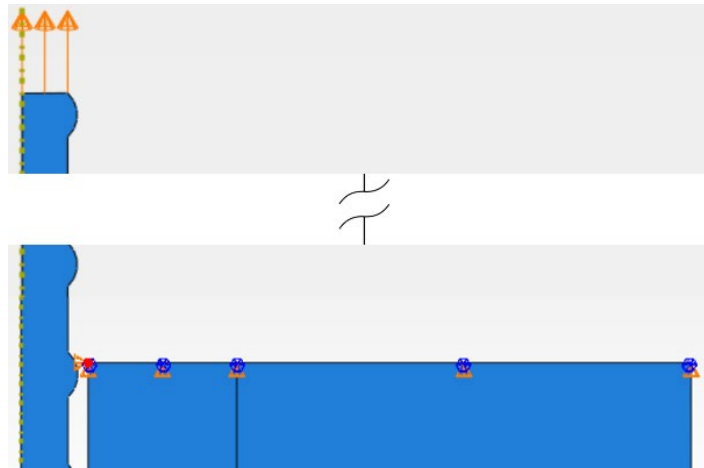
Figure 3.8: Section of the model's top part showing the boundary conditions.

General contact interaction was defined for the whole model, with self-contact, having normal and tangential behaviour defined in the interaction properties. Hard contact was used for normal behaviour, and a COF of 0.5 for the tangential behaviour. Lastly, three node sets were created for result extraction: (1) first at the top support to obtain the vertical reaction force, (2) one at the bottom of the rebar for free end slip, and (3) a set at the partition highlighted in Figure 3.9 on the rebar for the loaded end slip. The results of the loaded end are extracted from there to avoid extra calculations, taking into account the elongation and subtracting it as done in experimental programs. Instead, this allows for the recording of the slip at exactly the bonded region's end, neglecting the elongation that occurs beyond it at the unbonded region. Field outputs are requested at 50 equally spaced intervals.
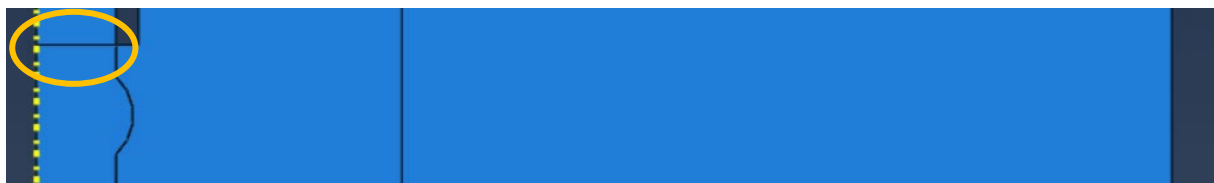
Figure 3.9: Section of the model assembly showing the partition at the top of the bonded area.

THIS PAGE WAS INTENTIONALLY LEFT BLANK

4. RESULTS AND MODEL DEVELOPMENT

This chapter presents the development and refinement of the numerical model, along with a comparison of its results to both analytical and experimental benchmarks. The numerical outcomes are evaluated against the analytical bond–slip model illustrated in Figure 2.6, as well as the experimental results shown in Figure 3.3 (c). The comparison with the analytical model aims to ensure that the numerical model accurately captures the key features of the bond–slip response, specifically, the ascending and descending branches and the friction plateau depicted in Figure 2.6. In parallel, comparison with the experimental curve in Figure 3.3 (c) focuses on accurately capturing the values of τ_{max} and s_1. Through iterative calibration and validation, the model is progressively refined to improve its predictive capability.

4.1. Results

To obtain the stress-slip relationship of the bond, the reaction force values from the top support are summed and converted to bond stress through Eq. (2.1). It is then plotted against the respective average displacement outputs for the free end and loaded end node sets. The results of this initial simulation show many limitations, especially in the model, which includes the concrete failure function and element deletion. Figure 4.1 and Figure 4.2 show the bond stress-slip relationship at the free end for the pull-out test simulated with and without concrete failure, respectively. A significant difference in τ_{max} and overall behaviour can be observed between the two graphs. It should be noted that the y-axis scales differ between the two graphs, which must be taken into account when comparing the data.

The main cause of this difference was the damage propagation pattern during the loading process. The deletion of tensile-damaged elements led to stress concentration in adjacent elements, ultimately causing their abrupt failure. Figure 4.3 shows the concrete damage during the first four steps in the loading process. No significant compressive damage was observed that could have led to this behaviour. This behaviour is delayed in the model without element deletion, as the damaged elements retain residual stiffness and continue resisting loads after damage initiation. This explains the higher τ_{max} observed in Figure 4.2. However, this value is higher than what was previously seen in the experimental results in Figure 3.3. In the following section, the model with concrete failure and element deletion is modified to enhance the stability and continuity of damage propagation.
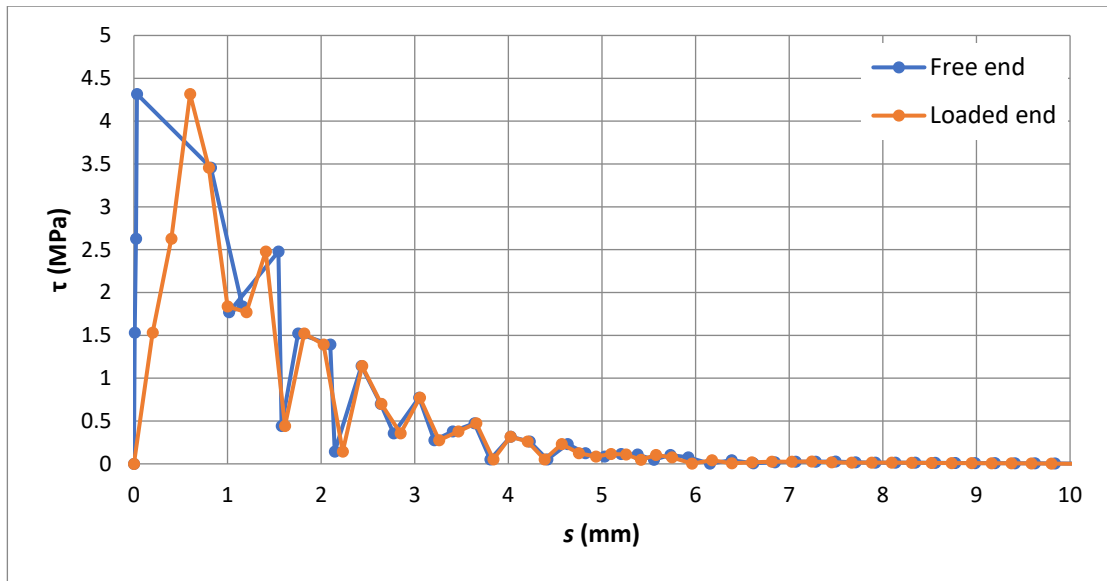
Figure 4.1: Bond stress-slip relationship for the model described in Chapter 3 without concrete failure.
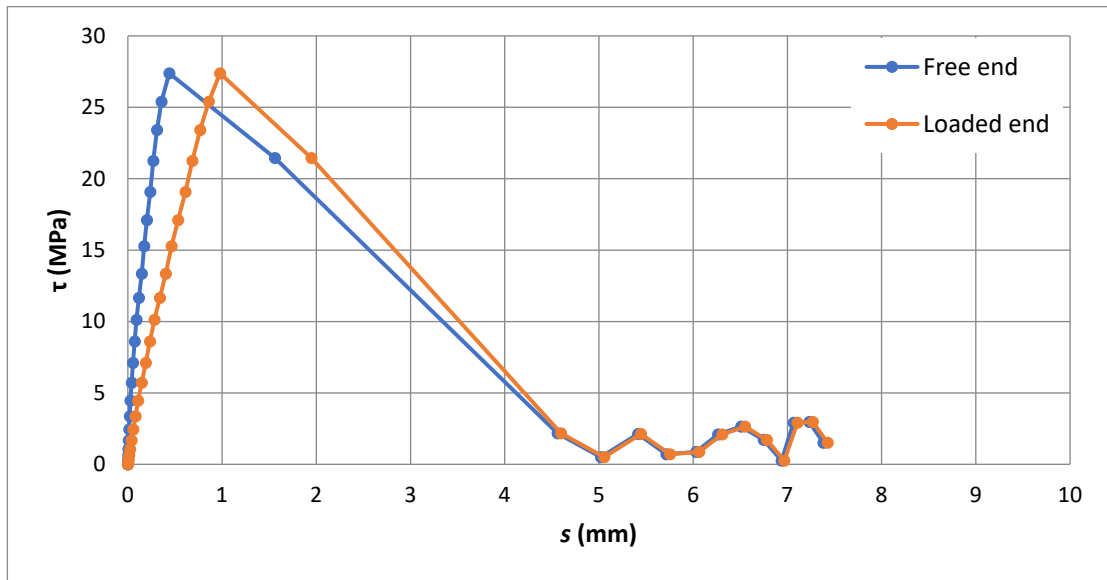
Figure 4.2: Bond stress-slip relationship for the model described in Chapter 3 with concrete failure.

(a) $t = 0.02$ (b) $t = 0.04$ (c) $t = 0.06$ (d) $t = 0.08$
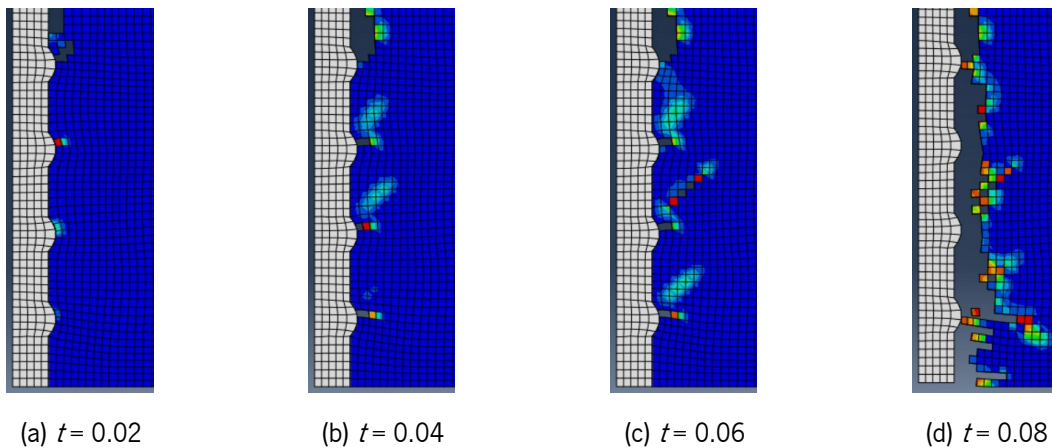
Figure 4.3: Tensile damage evolution in concrete at various step times *(t)* in the model with element deletion.

4.2. Effect of Loading Rate and Mesh Refinement

The displacement application rate was a possible cause for this abrupt failure in the model with concrete failure. To obtain a better representation of the results, a new amplitude, shown in Figure 4.4, was defined in a subsequent model. This smooth step amplitude was used to minimise the energy release stage where the damage propagates the most, which is why it has a stage with a low displacement rate at the corresponding step time.
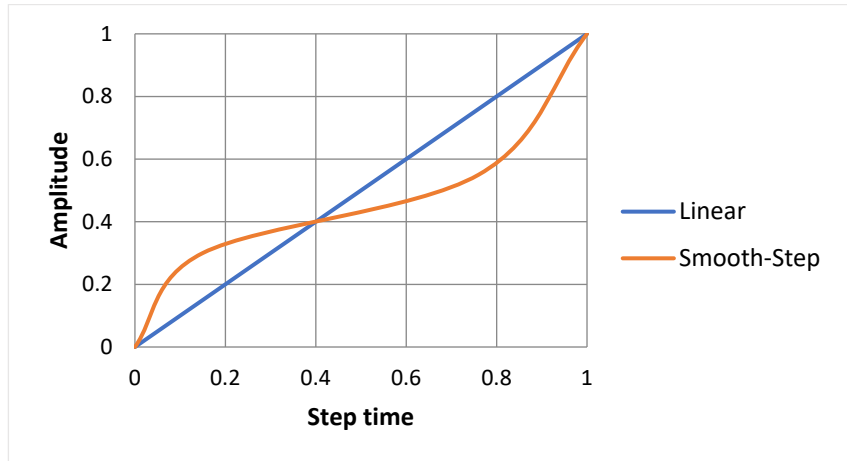
Figure 4.4: Smooth-step amplitude with displacement rate calibrated to obtain the best output distribution.

Although this modification improved the visualisation of the problem, it did not resolve the underlying issue. The bond stress-slip relationship obtained was similar to what was seen in Figure 4.1. The resulting bond stress-slip relationship from this simulation is presented in Annex II, which includes comparative graphs showing no significant variations in the overall stress-slip relationship of the simulations. Furthermore, the tensile cracking leading to the abrupt deletion of the elements could be seen as before. However, this behaviour was observed at a step time of 0.22 rather than 0.08, as shown in Figure 4.5. This occurred with a more gradual deletion in the steps before due to the new amplitude defined with a lower loading rate.

Another anomaly observed in the simulations was the incompatibility between the rebar and concrete mesh at the bonded area, as seen in Figure 4.6 (a). Also, the tensile cracking followed a diagonal path, which was not very well defined, showing a step-like path due to the geometry of the elements, as can be seen in Figure 4.5 (c). Therefore, the mesh element shape at that region was changed to triangular elements, and the mesh nodes were matched for both the rebar and the concrete, as shown in Figure 4.6 (b), by using local seeds. The results following these modifications demonstrate a better-defined path for cracking damage, but the abrupt failure is still present in the results, as can be seen in Figure 4.6 (c) and (d).

(a) $t = 0.16$ (b) $t = 0.18$ (c) $t = 0.20$ (d) $t = 0.22$
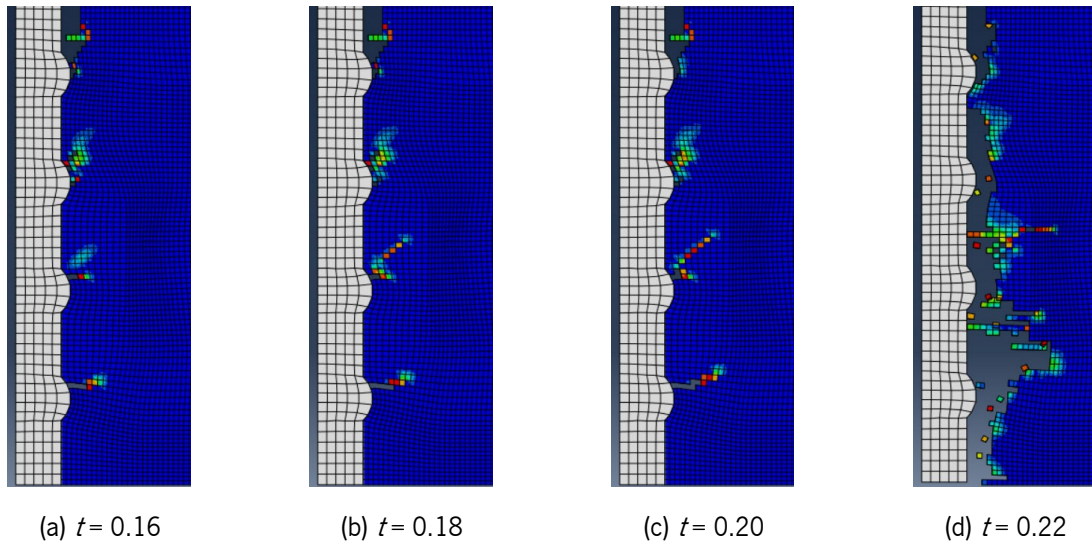
Figure 4.5: Tensile damage in concrete at step times 0.16 through 0.22 with the new defined amplitude.

(a) Quadrilateral mesh at the interface   (b) Triangular mesh with matching nodes.   (c) Tensile damage at $t = 0.24$ (d) Tensile damage at $t = 0.26$
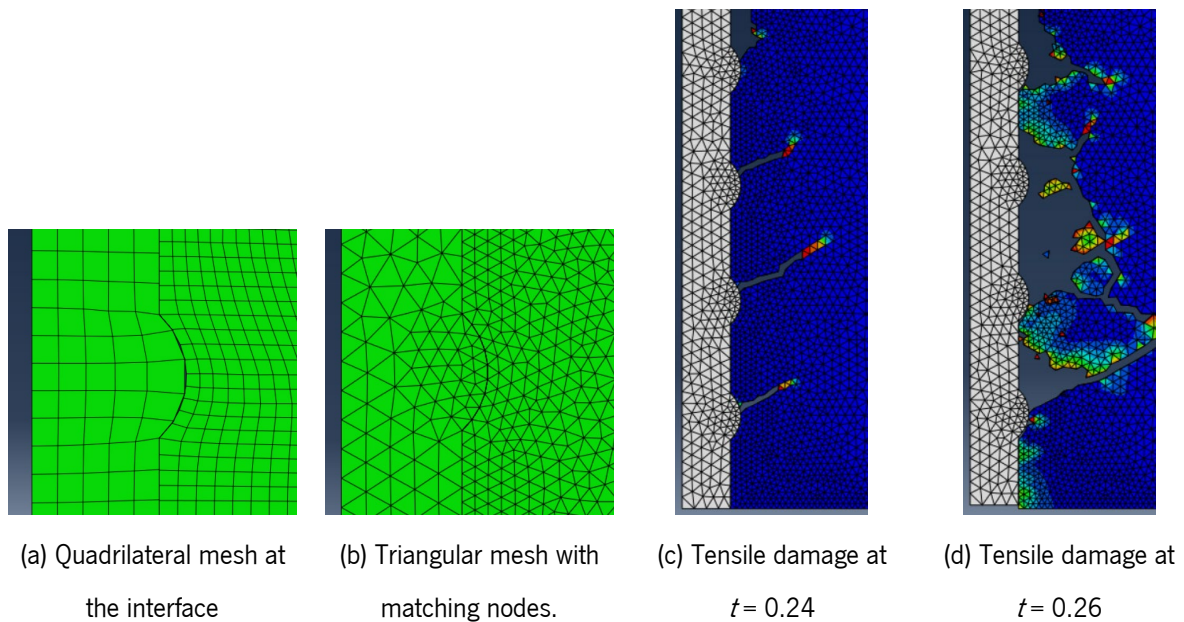
Figure 4.6: New mesh definition using triangular element shape.

Studying the results following these changes, a deviation in the cracking path and a stress singularity could be observed as the damage propagates to the quadrilateral-shaped coarse mesh region. As successfully implemented before, the quadrilateral element shape was changed to triangular in that region as well to obtain a better-defined damage path and a more stable propagation. Finally, the concrete failure function was neglected as it caused the abrupt element deletion that could not be resolved.

The results of these trials in Figure 4.7 show a significant improvement in the post-peak behaviour. Specifically, an increase in the friction plateau can be seen in the bond stress-slip relationships using a triangular mesh for the coarse region. This implies that the friction plateau described by the analytical model in Figure 2.6 is characterised in the current model. The use of a triangular mesh in the coarse

region successfully eliminated the singularity encountered after the damage propagates to that region. However, the value of τ_{max} has increased even more compared to that in Figure 4.2, which was already higher than the 7.6 MPa seen in the experimental results in Figure 3.3 (c).
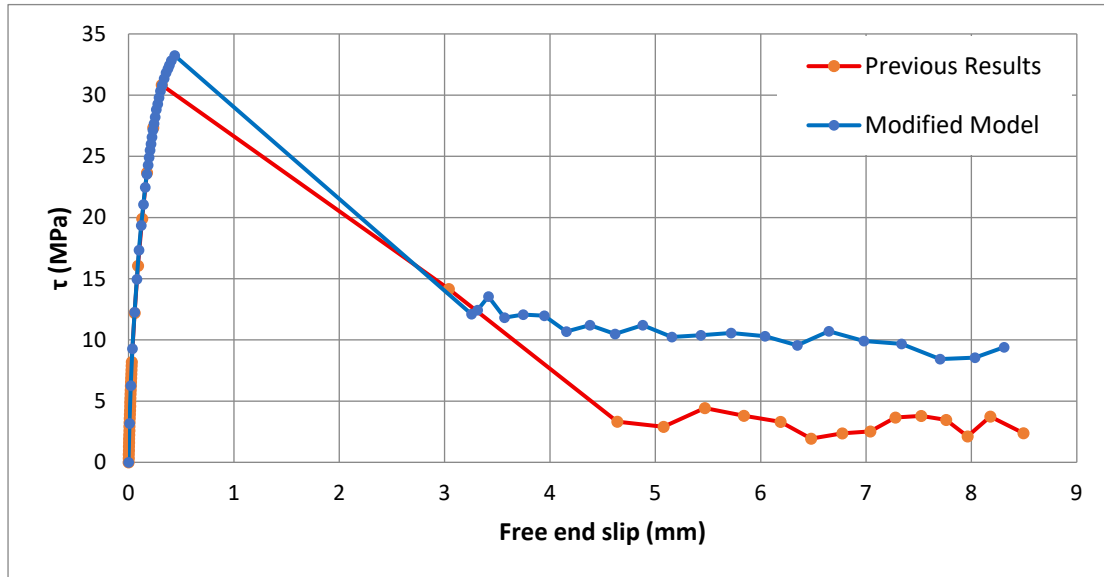
Figure 4.7: Bond stress-slip relationship of modified models (without concrete failure).

Following these modifications, the fine mesh region was reduced to the partitioned geometry shown in Figure 4.8. The change was made to reduce the element number and, consequently, the computational effort required. The obtained bond behaviour was unaffected after this change.
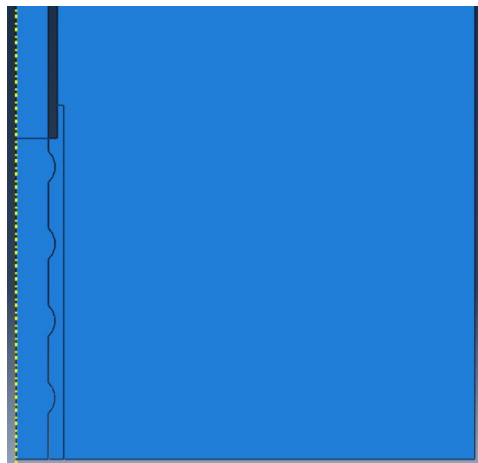
Figure 4.8: Geometry with refined mesh partition in bonded region.

The final refinement involved simplifying the rebar geometry beyond the bonded region. As seen in Figure 3.4, the ribs were previously modelled in the unbonded area. This was changed to a plain round rebar as there is no interlock in that region and no reason for their modelling as shown in Figure 4.8. This change of geometry and mesh decreased the CPU time by 16% from 3 hours and 9 minutes to 2 hours

and 38 minutes. The results showed similar behaviours with a slight increase in the τ_{max} and friction plateau. This effect is possibly due to the different elongation that occurs in the rebar now that it has a lower cross-sectional area at certain points.

4.3. Constitutive Model Calibration

Based on the experimental results presented in Chapter 3, one of the limitations of the model that remains at this point is the high value of τ_{max}. The descending branch does not have a good definition either, with a sudden jump in the slip after the τ_{max} is reached. The τ_{max} being higher than concrete is not common in experimental results, and the descending branch can be better defined with more output data points. These aspects will be further investigated in the coming sub-sections.

4.3.1. Tensile Softening Behaviour

When looking into the descending branch of the stress-slip relationship, it can be observed that the post-peak relationship is similar in shape to the tensile softening model introduced. This led to inputting a modified softening model from [73], shown in Figure 4.9 (a). A higher value of σ_t at the final point was also introduced to obtain a maximum d_t value of 0.9, compared to 0.99 previously defined in Chapter 3, resulting in the curve shown in Figure 4.9 (b).
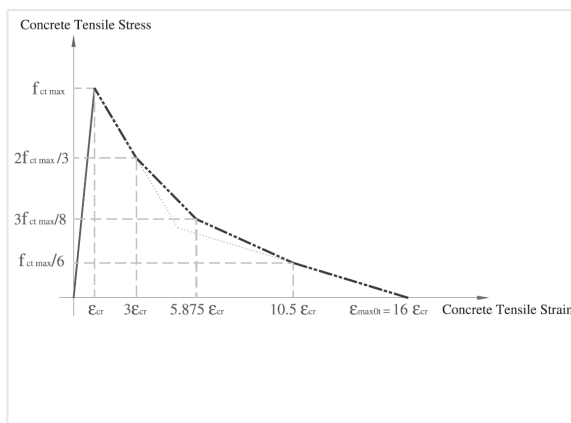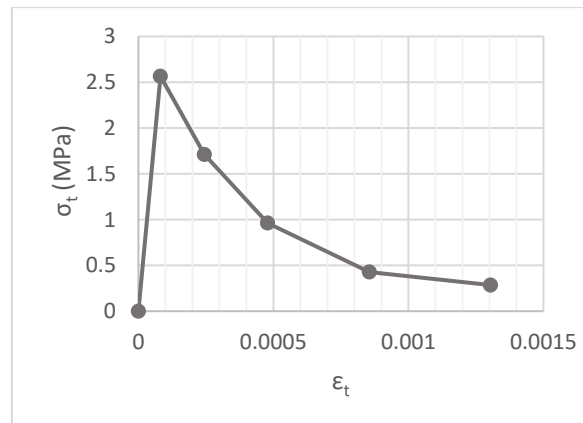
(a) Analytical model　　　　　　　(b) Calculated result for $f_{ct,max}$ = 2.56 MPa

Figure 4.9: Modified analytical model for tensile softening behaviour in [60].

While the resulting stress-slip relationship of this change had the same τ_{max}, additional points on the descending branch were introduced with a higher stress on the friction plateau. This suggests that, between the compressive and tensile behaviours of concrete in the model, the post-peak response is

primarily governed by its tensile softening behaviour. The friction plateau that is seen in experimental results is a result of the mechanical interlock and wedging action of the crushed concrete. This behaviour is captured differently in the model. In reality, crushed or cracked concrete ceases to resist or transform loads imposed on it to the surrounding concrete after bond failure. Whereas in the model, the degradation mechanisms cause a loss in stiffness while maintaining the ability to transmit loads. Therefore, despite the failure of the bond, the damage continues propagating through the whole concrete specimen. Although this phenomenon may not reflect physical reality, it serves as a practical means of approximating the friction plateau, since the crushed elements cannot be separated to achieve wedging and interlocking as in experimental programs. Hence, the increased residual stiffness in the new tensile softening model in Figure 4.9 (b) resulted in a higher stress value of the friction plateau.

4.3.2. Compressive Inelastic Behaviour

With a step forward in the descending branch, the remaining concern to be considered is the high value of τ_{max}. Similar to what was observed between the post-peak behaviour and the tensile softening model, the ascending branch resembles the compressive behaviour of the concrete. Therefore, the compressive behaviour in the CDP inputs was modified with an additional point to get the maximum input of d_c up to 0.98 from the previous maximum value of 0.42. The modified compressive stress-strain and the resulting bond stress-slip relationships are shown in Figure 4.10 and Figure 4.11, respectively. The resulting stress-slip relationship in light colour shows a lot of instability and jumps between output points, but the polynomial trendlines (Poly.) plotted in darker colours in Figure 4.11 show an improved relationship with a lower τ_{max}. This result confirms that stiffness degradation affects the stress values, as the higher input damage value resulted in less residual stiffness in the damaged material, which in turn translated to lower stress values for the bond stress-slip relationship. Moreover, the s_1 has a similar value to that of the experimental ones in Figure 3.3 (c).

A promising next step to enhance the resulting behaviour would be to use a compressive softening relationship resembling the one presented in the Abaqus documentation [18] (shown in Figure 2.9).
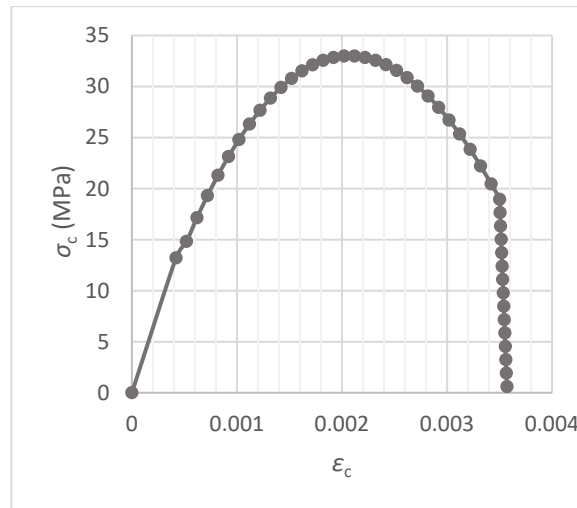
Figure 4.10: Modified compressive stress-strain relationship for concrete with maximum $d_c = 0.98$.
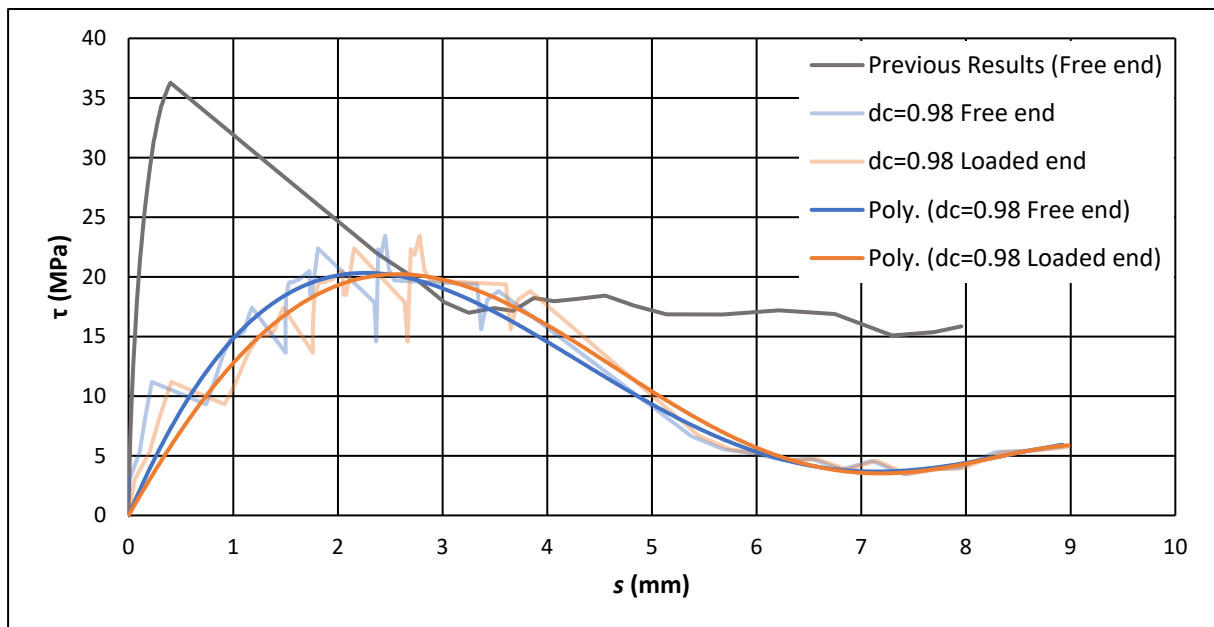
Figure 4.11: Bond stress-slip relationship with modified compressive damage reaching 0.98.

4.3.3. Inelastic Behaviours from "CDP Generator"

CDP Generator [74] is a tool available online that utilises pre-defined subroutines from various design codes to generate compressive and tensile behaviour inputs for the CDP model. One of the design models that is utilised is the Model Code 1990 (MC90) [75], which will be used in the following steps. Although to the author's knowledge, the reason for using the MC90 over more recent versions is not stated explicitly in the software's publication, the reason can be attributed to the fact that the subsequent updates do not include equations defining the tensile softening behaviour in terms of the stress-strain relationship. The more recent codes describe the tensile behaviour of concrete in terms of fracture energy and crack

opening instead of strain, which is also present in the MC90 [76]. The software requires data such as the f_{cm} and f_{c0}/f_{cm}, which were calculated earlier from EC2 equations and used to generate the inputs required for CDP. Figure 4.12 shows the interface of the software, which includes the data required in order to generate the CDP inputs.

Figure 4.12: CDP Generator and inputs used to generate inelastic behaviours.

The obtained tensile inelastic behaviour may not be very reliable, as it showed that the cracking strain is much greater than what is expected in plain concrete with a maximum ε_t^{cr} of 0.058. Accordingly, the following modifications were implemented: (1) the f_{ctm} was reduced to the value obtained through EC2 equations previously, and (2) the strain values were reduced by two orders of magnitude. In the end, the purpose of using this software was to derive softening behaviours that align more closely with those in the Abaqus documentation; hence, it is favourable to retain as much data from EC2 results as possible. Figure 4.13 shows the previous inelastic behaviour inputs with the ones obtained from the CDP generator, following the tensile behaviour modification. Additionally, another input was used where the compressive curve from the CDP generator was extended up to a stress value where the damage of 0.98 was reached. The extended portion is shown in Figure 4.13 (a) in green. The original generated tensile behaviour with a maximum ε_t^{cr} of 0.058 is not shown since the scale is too different to be seen in contrast in the graph. Figure 4.14 illustrates the resulting bond stress-slip relationships for various CDP model inputs, including a comparison with the EC2 model. The 'CDP Generator (original)' curve exhibits a relatively higher τ_{max} and a more pronounced friction plateau. This behaviour is attributed to the high cracking strain (ε_t^{cr} = 0.058) in the original generated inputs, which requires significant deformation to induce tensile damage. The 'CDP Generator - MT' model, incorporating modified tensile behaviour as described previously (where fctm was reduced and strain values were scaled down), maintains a similar ascending branch but reaches a lower τ_{max} than the 'original'. This is followed by a notably steeper descending branch.

(a) Compressive inelastic behaviour
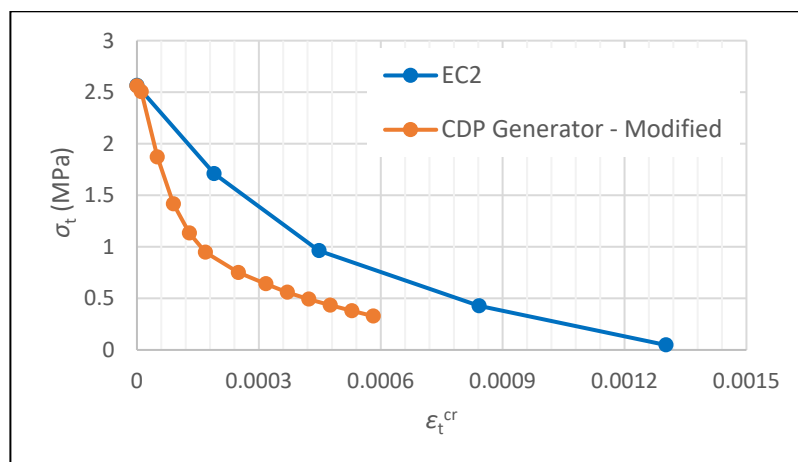
(b) Tensile inelastic behaviour

Figure 4.13: Concrete inelastic behaviour input points used in the CDP model.

The 'CDP Generator - MT-dc' model, which further extends the compressive curve to a damage value of 0.98, shows a closer resemblance to the EC2 model results, particularly with a better-defined descending branch and friction plateau.

Overall, the 'CDP Generator - MT' model demonstrates the most stable slipping and damage propagation, characterised by minimal sudden jumps in the curve and the resemblance to the analytical model in Figure 2.6. Despite these improvements, the descending branch in all CDP models still requires further refinement and stability. The next section investigates factors influencing these instabilities further.
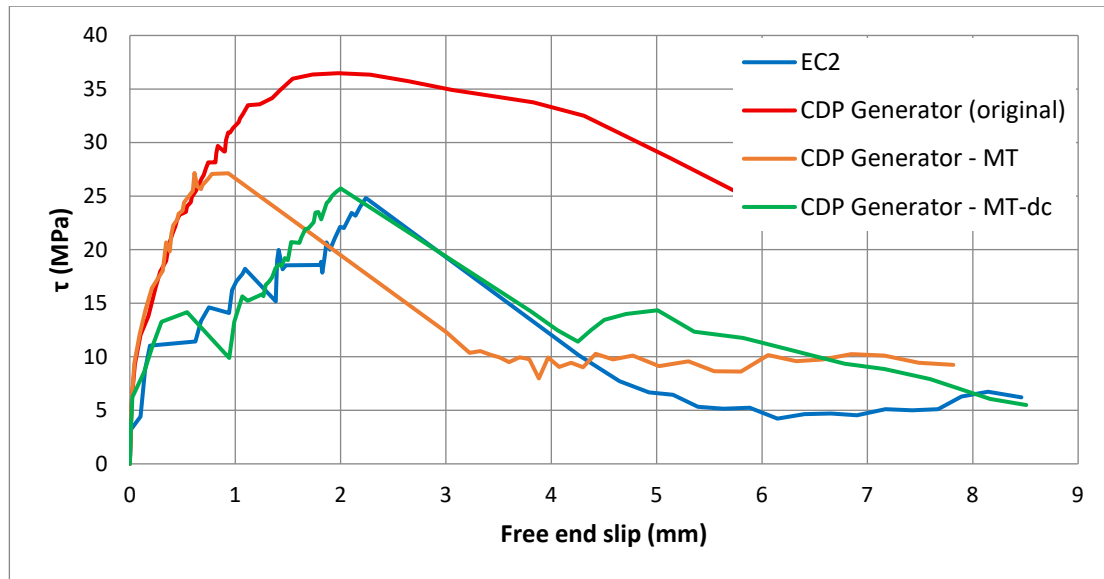
Figure 4.14: Bond stress-slip relationship with different CDP model inputs described earlier.

4.4. Geometry Adjustments

The compressive damage propagation stages shown in Figure 4.15 visualise localisation of compressive damage that could be attributed to two possible factors: (1) the partition used to separate the fine and coarse mesh regions delaying the propagation of damage which could cause energy accumulation leading to a sudden release post-peak, and (2) the elongation of the rebar in the unbonded area could be a factor for elastic energy build-up, causing a sudden slip where the elongation is undone upon the concrete's failure.

4.4.1. Partitions

In order to investigate the first factor, the various partitions shown in Figure 4.16 were used, with the final model not having a partition. The simulations were done for both CDP model inputs from the CDP generator 'MT' and 'MT-dc'. The resulting relationships were similar in all cases, with minor variations. Partition 2 in the 'MT-dc' set showed a slightly better-defined descending branch with extra points. However, the overall results show that the effect of different partitions is minor on the bond behaviour.

(a) $t = 0.12$ (b) $t = 0.14$

(c) $t = 0.40$ (d) $t = 0.70$ (e) $t = 0.72$
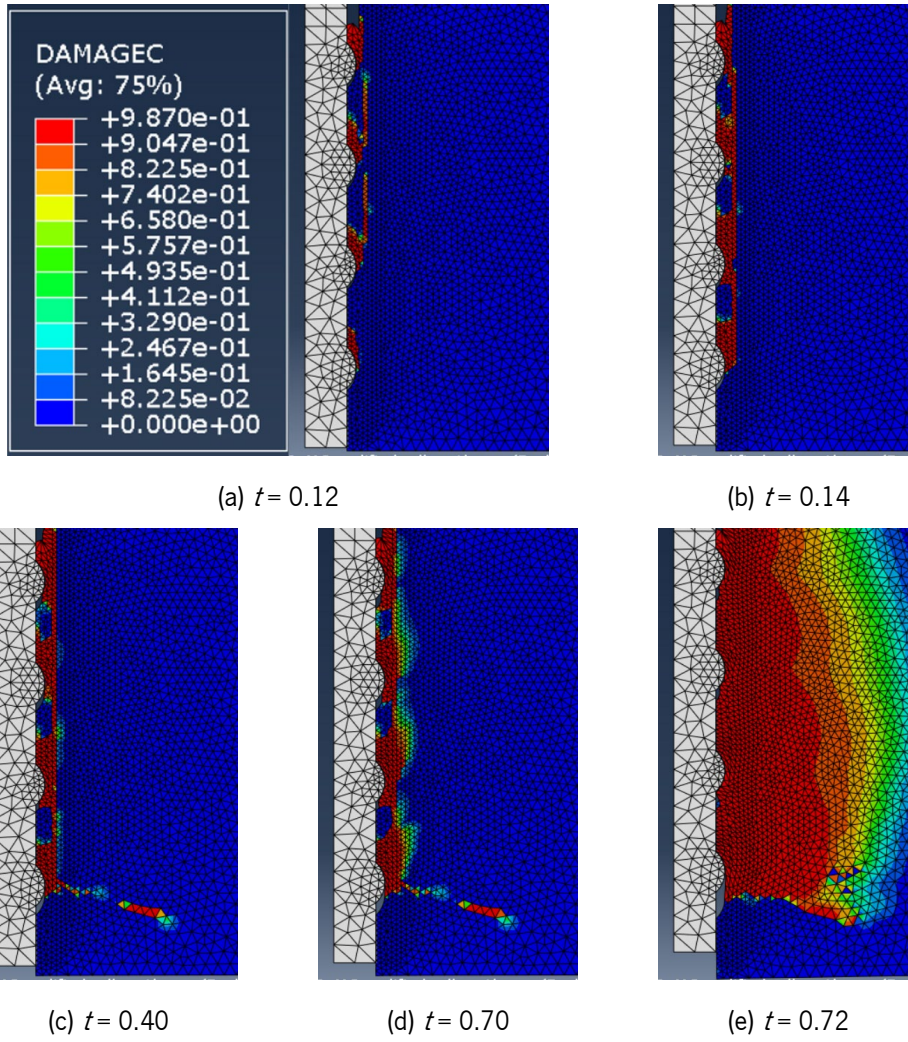
Figure 4.15: Compressive damage at the bond interface in different step times.

(a) Partition 1   (b) Partition 2   (c) No Partition
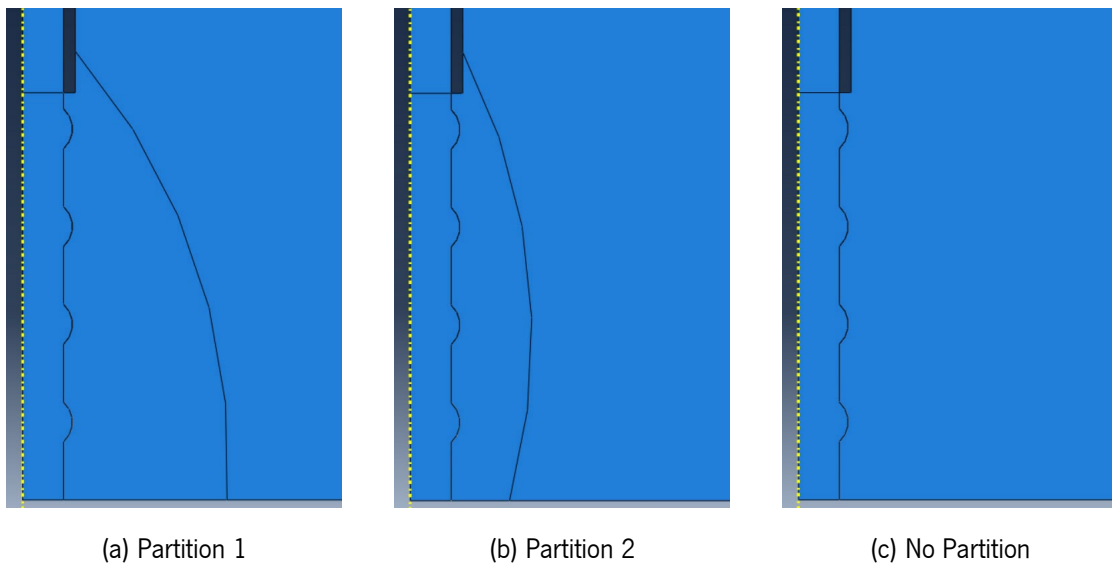
Figure 4.16: Fine mesh region partitions used to investigate their effect on the bond behaviour.

4.4.2. Rebar Unbonded Region

To look into the second potential cause of energy accumulation mentioned earlier, a remodelled geometry shown in Figure 4.17 was used. The unbonded part of the rebar was removed, and the displacement was directly applied at the top of the bonded region, eliminating the element causing elongation.
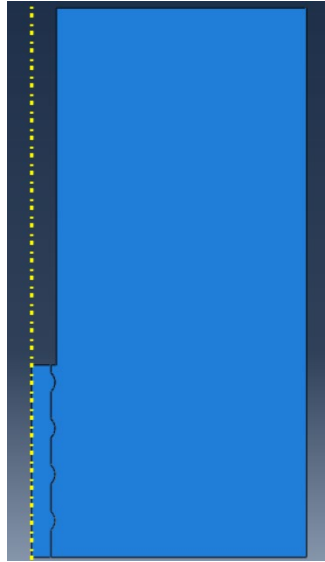
Figure 4.17: Remodelled rebar geometry with unbonded region removed from the part.

The result of this remodelling in Figure 4.18 shows a significant improvement in the definition of the descending branch. Furthermore, this simplification reduced the CPU time by 26% from 2 hours and 27 minutes to 1 hour and 48 minutes.
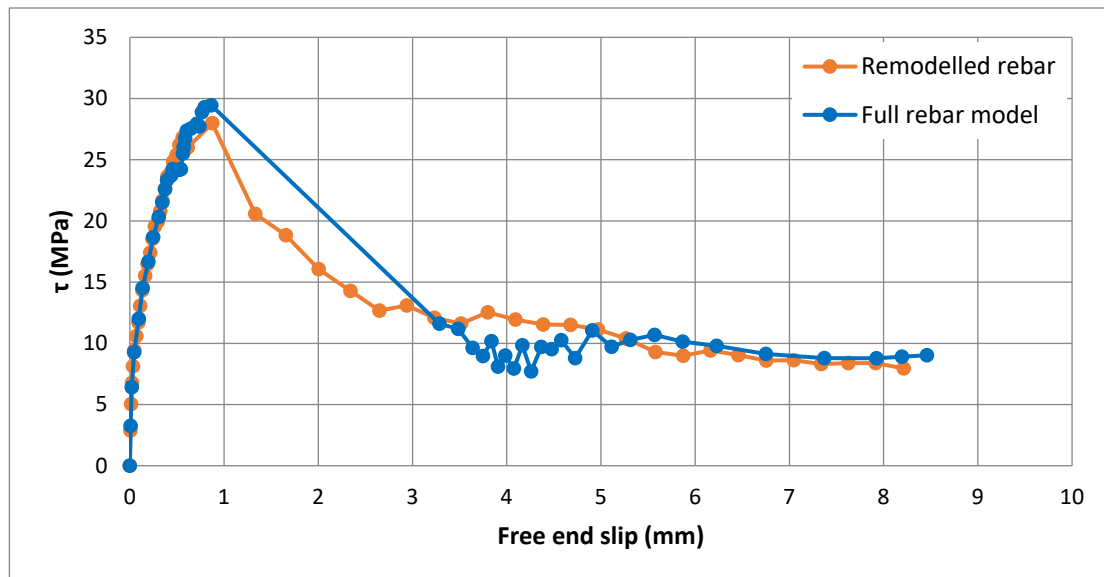
Figure 4.18: Bond stress-slip relationship of rebar without unbonded part, compared to the previous results from the full rebar model.

4.5. Sensitivity Analysis

In this section, various parameters listed in Table 4.1 are studied to analyse their impact on the interface behaviour. Throughout the analysis, two models are used: the 'Simplified' model with assumed material properties that has been used so far, and 'D14S3', a modified version of it. In 'D14S3', the dimensions and properties are changed to the reported ones in [68], which was the initial source of the rib geometry. Additionally, the 'Simplified' model includes the unbonded region of the rebar, whereas the 'D14S3' model has the load applied at the end of the bonded region, as in the previous section.

Table 4.1: Parameters that will be studied in this section.

Model	Parameter Type	Parameter
Simplified	Plasticity Input	ψ
		μ
D14S3	Mesh Configuration	Coarse Mesh
		Fine Mesh
	Interaction Characteristic	COF

For 'D14S3', rib spacing is changed to the one reported with the same name in [68] and has a 10 mm spacing. GFRP material properties are changed to match the ones reported, but the article only mentions the longitudinal elastic modulus (E1). The other properties shown in Table 4.2 are completed using the data provided in [13] because of their similar surface configuration and longitudinal elastic modulus. Finally, the concrete dimensions are changed to match the concrete cube dimensions used in the experimental program reported. However, this brings back the limitation of using axisymmetric modelling space, as the same dimensions can be used, but the final shape can only be a cylinder, as cubes are not axisymmetric geometries.

Table 4.2: Updated engineering constants input in elastic properties of GFRP.

E1 (MPa)	E2 (MPa)	E3 (MPa)	v_{12}	v_{13}	v_{23}	G12 (MPa)	G13 (MPa)	G23 (MPa)
47810	17500	17500	0.3	0.2	0.2	8000	8000	8000

4.5.1. Dilation Angle and Viscosity Parameter

An additional trial was carried out to study the impact of the dilation angle on the behaviour of the models. Values from 20° to 50° were simulated in 5° intervals for both the MT and MT-dc models. The set of

results for MT shown in Figure 4.19 shows a clear pattern of increasing τ_{max}, decreasing s_1, and decreasing stress of the friction plateau with the increase of ψ. This pattern can also be seen in Figure 4.20 with the set of results for the MT-dc model from 35° up to 50°, whereas the lower values show an opposite pattern. Once again, the results with the model have a compressive damage of 0.98 and are less stable. The simulations for MT with ψ=25° and MT-dc with ψ=20° did not converge, which is why the curves terminate earlier than the rest.

Additionally, Viscosity parameters of 0.001 and 0.01 were also experimented on both models. The results yielded identical bond stress-slip relationships in both models. Hence, the model has no dependence on the viscosity parameter of the CDP.
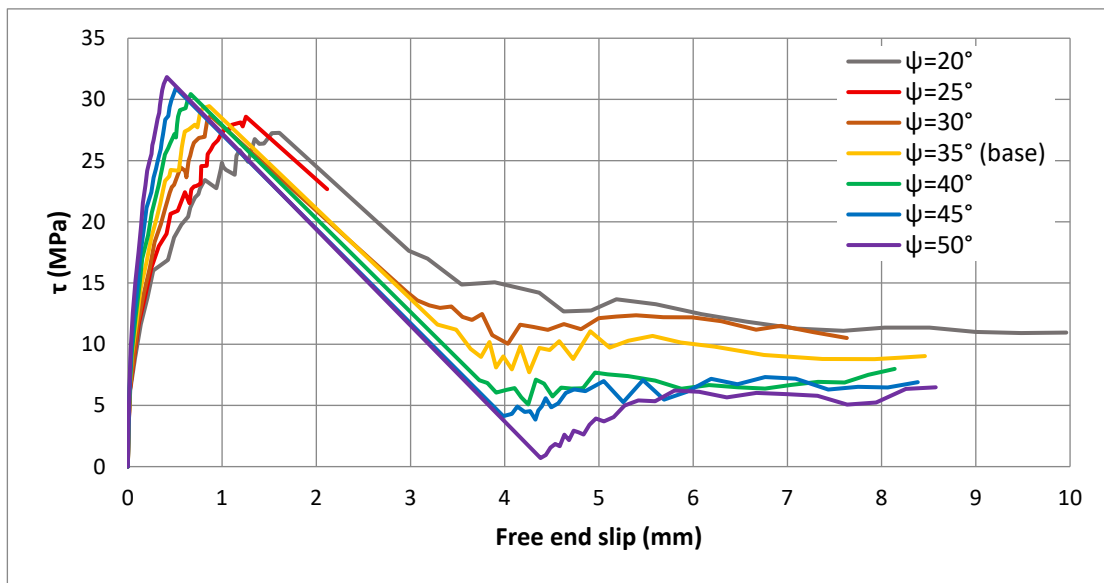
Figure 4.19: Dilation angle sensitivity analysis results for (MT) CDP model input.
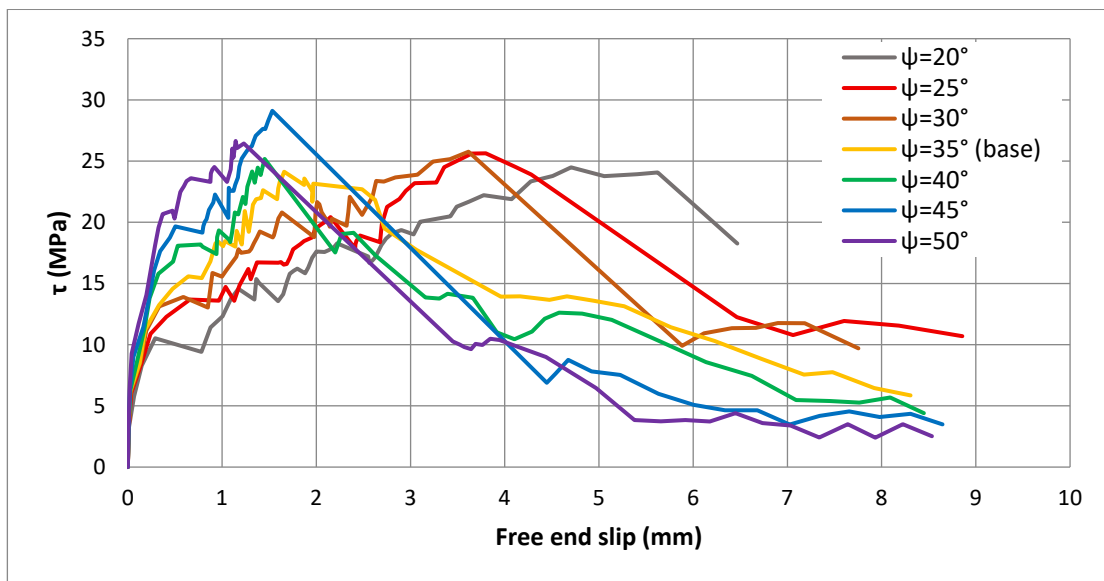
Figure 4.20: Dilation angle sensitivity analysis results for (MT-dc) CDP model input.

4.5.2. Mesh

Mesh sensitivity analysis was then carried out on the coarse mesh region, where 2 mm was used originally. The modified model in the previous step, with reduced rib spacing but without resizing the concrete specimen, was used. The use of this bigger concrete specimen in this analysis was to have a clearer picture of the effect of the change with more elements present, especially in terms of CPU time. Global mesh sizes of 3, 4, 5, and 7.5 mm were studied. Table 4.3 shows their respective CPU times recorded. The resulting bond stress-slip relationships have minor variations and, thus, are unaffected by the coarse mesh size. The reason is that concrete damage propagates in that region only after τ_{max} has been reached, as previously observed in Figure 4.15. However, the tensile cracking of concrete in the initial damage stage for the 7.5 mm mesh is different from the rest, as shown in Figure 4.21, where the 5 mm mesh is selected to represent the smaller meshes. The crack initiated from the last rib at the bottom follows a different path, aligning with the finer mesh region, which could potentially affect the results of subsequent trials. Hence, a 5 mm coarse mesh size will be used for improved computational efficiency for the succeeding simulations.

Table 4.3: CPU times of coarse mesh sensitivity analysis.

Coarse Mesh Size (mm)	2	3	4	5	7.5
CPU Time (seconds)	12,113	9,267	6,670	5,298	4,144

(a) 5 mm   (b) 7.5 mm
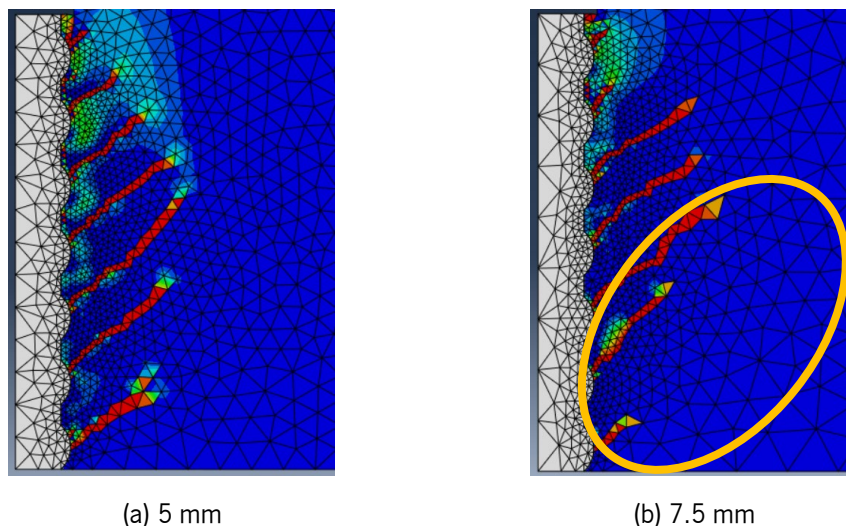
Figure 4.21: Tensile cracking pattern at $t = 0.16$.

For the fine mesh size sensitivity analysis, local mesh seeds of size 0.2, 0.35, 0.5, and 1.2 mm were simulated to be contrasted with the original 0.85 mm used. Due to the high number of increments required for the 0.2 and 0.35 mm models, double precision was used when running the Abaqus/Explicit

analyses. The results once again showed the independence of the resulting behaviour on the mesh size up to 1.2 mm. However, an abrupt propagation of compressive damage in the model with a 1.2 mm fine mesh size was seen near the peak stress, which indicates instabilities in the damage propagation. The 0.85 mm mesh size will hence be used in upcoming simulations as it is the most efficient in terms of CPU time, as shown in Table 4.4, and also does not result in any unstable behaviours.

Table 4.4: CPU times of fine mesh sensitivity analysis.

Fine Mesh Size (mm)	0.2	0.35	0.5	0.85	1.2
CPU Time (seconds)	63,795	30,303	8,805	6,528	3,122

4.5.3. Rebar Placement

Next, a sensitivity analysis of the first rib location at the top of the bonded region was carried out. This is not a question in practice since ribbed rebars have spiral deformations, and moving the rebar up and down would not affect the overall location of the ribs in the interface perimeter. However, since they are simplified to circular wound ribs in the model, the placement of the rib might affect the overall interface behaviour. Various positions shown in Figure 4.22 were placed at the top of the bonded area to study their effect on the results.

(a) Original position   (b) Position 4
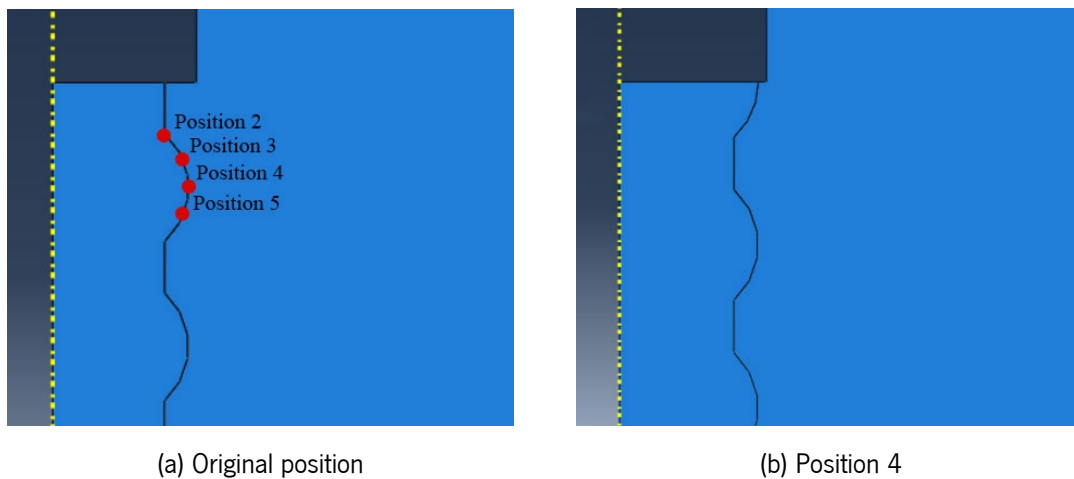
Figure 4.22: Rib positions to be placed at the top of the bonded area for sensitivity analysis, showing (a) the original position and highlighting the potential positions with (b) an example at Position 4.

The model's sensitivity to this factor was mostly in terms of result stability rather than overall behaviour. The bond stress-slip relationships remained the same for all positions, but the model with position 4 showed slight stability improvements in its behaviour. One such improvement is shown in Figure 4.23 (a), where position 2 elements on the top of the bonded region show significant distortion following the

induced damage from the pull-out force. Unlike the other trials, the elements were not distorted even after complete failure when using position 4 as seen in Figure 4.23 (b).

(a) Position 2   (b) Position 4
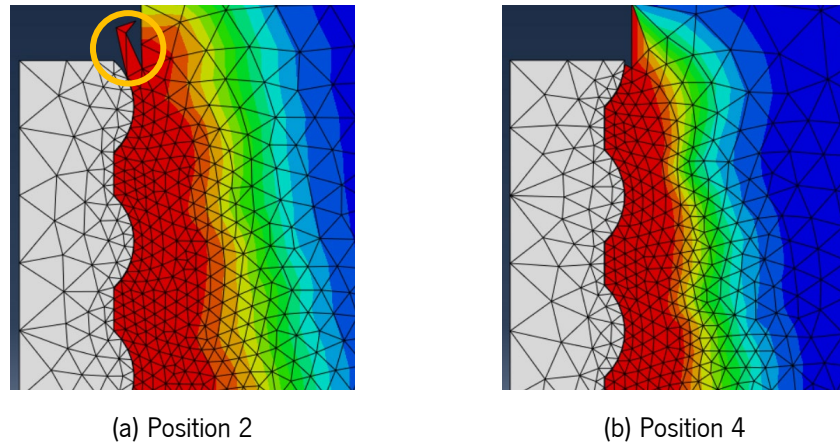
Figure 4.23: Element distortion comparison for different rib positions.

4.5.4. Coefficient of Friction

Lastly, COF sensitivity analysis was carried out with values of 0.1 through 0.4 in 0.1 intervals, and compared to the base value of 0.5. Figure 4.24 and Figure 4.25 show the results of this analysis, which was carried out for both the (MT) and (MT-dc) CDP model inputs. From these figures, it can be observed that decreasing COF causes a decrease in τ_{max} and s_1. With that being said, the initial stress-slip relationship remains the same, with lower stress at which the damage propagation occurs. Meaning there is not a scale-down of the overall behaviour when reducing the value of COF, but rather a cutoff in the relationship before it can evolve further. This change can be more evidently seen in the results of (MT-dc) models. Additionally, the friction plateau also decreases with decreasing coefficient of friction.
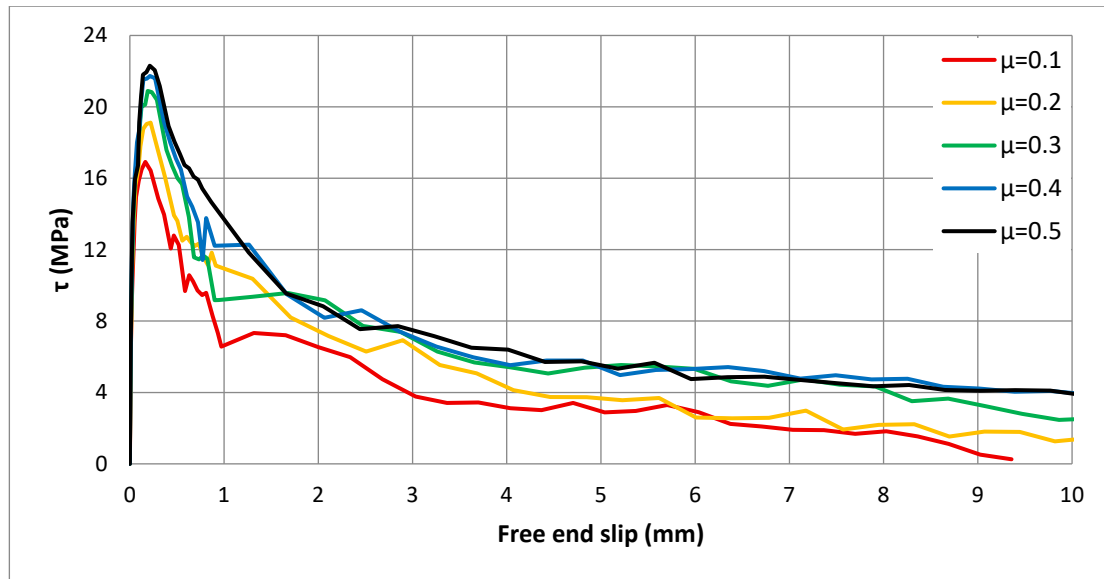
Figure 4.24: Bond stress-slip relationships from friction coefficient sensitivity analysis with (MT) CDP model.
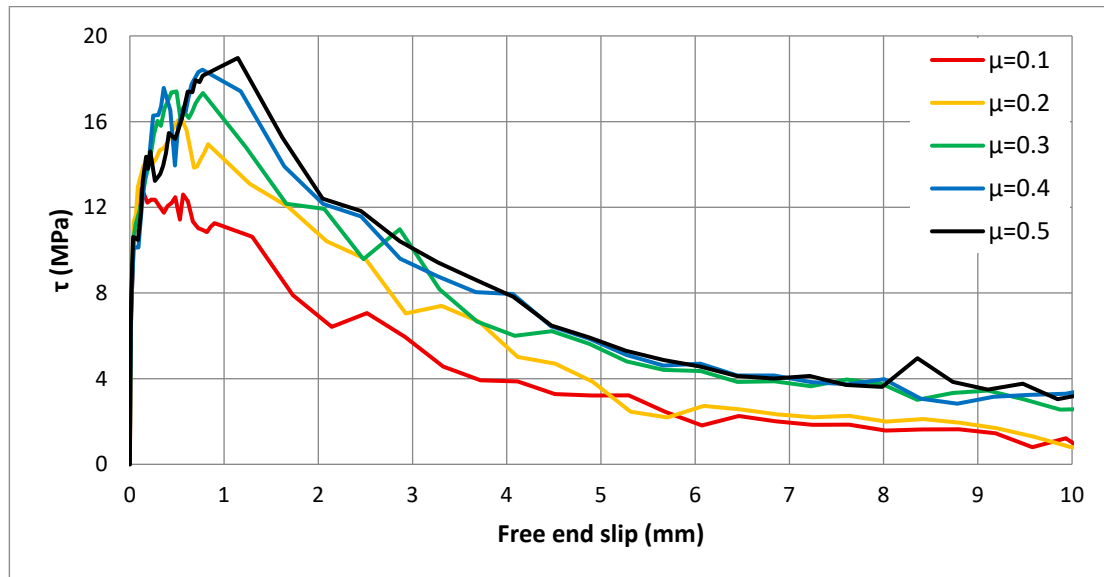
Figure 4.25: Bond stress-slip relationships from friction coefficient sensitivity analysis with (MT-dc) CDP model.

The descending branch was significantly improved throughout this section, showing resemblance to the analytical models in Chapter 2 and experimental results. On the other hand, the τ_{max} remains higher than the experimental values in section 3.1, with the value of s_1 also being different in most results. Table 4.5 summarises the parameters studied and their impact on the various aspects of the bond stress-slip relationship, namely, τ_{max}, s_1, and friction plateau.

Table 4.5: Qualitative impact of parameters on key aspects of the bond stress-slip relationship.

Parameter	Impact on τ_{max}	Impact on s_1	Impact on Friction Plateau
ψ	Medium	High	High
μ	*No Impact*	*No Impact*	*No Impact*
Coarse Mesh	*No Impact*	*No Impact*	*No Impact*
Fine Mesh	*No Impact*	*No Impact*	*No Impact*
COF	High	Low	Medium

The coming chapter presents a parametric study to further assess the model's capability to capture the interface behaviour and to better approximate the bond stress-slip relationship observed in the experimental results. The sensitivity analysis focused on numerical parameters, such as model fitting constants and assumed interface properties. It examined how these parameters influenced the bond stress-slip behaviour. In contrast, the parametric study will shift attention to physical and mechanical properties of the materials involved—namely, the GFRP reinforcement and concrete. Specifically, the effects of rebar diameter, surface deformation, and elastic modulus, and the height and diameter of the concrete specimen will be investigated.

5. PARAMETRIC STUDY

Before commencing with the parametric study, CDP inputs with lower ψ were simulated, now that the model's behaviour is more stable. Unlike the trials in the previous chapter, it was easier to reach convergence with lower ψ, as shown in Figure 5.1. Material inputs MT and MT-dc were used with ψ of 20° and 35°, and MT-dc with ψ of 20° showed the highest value of s_1 and the lowest τ_{max}. However, the s_1 previously seen in Figure 3.3 (c) approaches 3 mm, whereas this one still only has a value of 1.14 mm. Similarly, the τ_{max} is 2.5 times greater than the experimental value of 7.6 MPa. These results will need to be calibrated, potentially based on the revelations of this chapter.
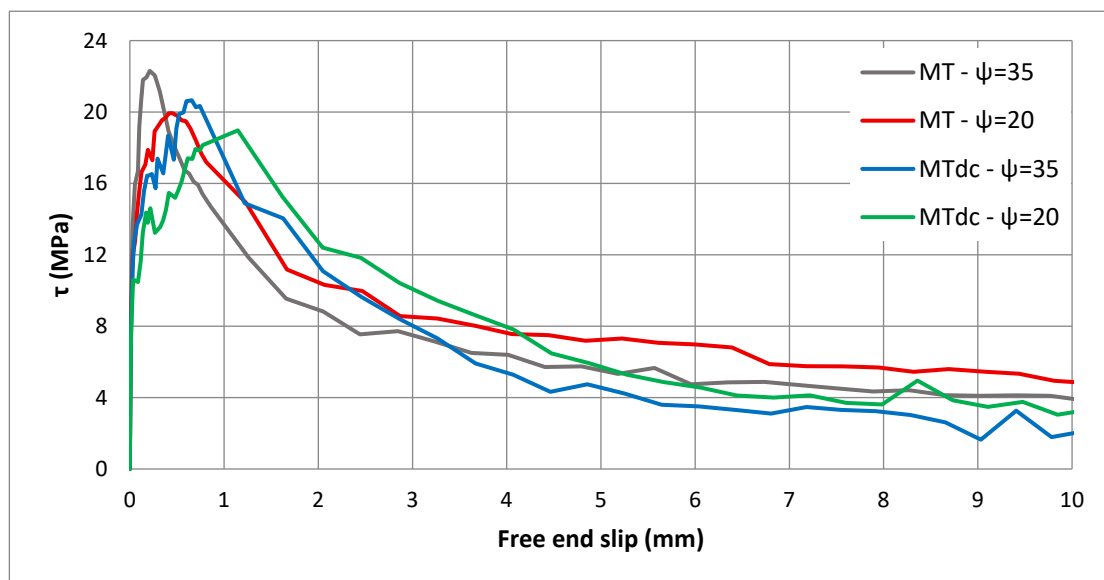
Figure 5.1: Bond stress-slip relationship of D14S3 rebar with various CDP inputs.

5.1. Bar Geometry

In addition to the previously modelled S3 rib geometry, [68] describes two other rib geometries, S1 and S2. The rib dimensions of these two types of rebar are listed in Table 5.1. To study the validity of the model with various ribbed rebar geometries, the S1 and S2 rebars with 14 mm diameter are modelled using the same material properties stated in section 4.5.

Table 5.1: Rib geometry dimensions of different rebar types provided in [68].

Rebar Type	Diameter (mm)	Rib Width (mm)	Rib Spacing (mm)	Rib Height (mm)
S1		4.6	5.0	0.1
S2	14	6.6	8.0	0.8
S3		6.8	10.0	1.5

5.1.1. 'S1' Surface Geometry

In the results of D14S1 shown in Figure 5.2, a second peak can be seen after the descending branch starts at about 0.6 mm. The sub-figures use different y-axis scales, which should be considered when comparing the data. This second peak is usually lower than the previous peak in experimental results, if it exists [49]. Whereas in the model, the second peak at 1.8 mm has a higher stress value than the first one. This occurs due to the friction between the rebar and the concrete, preventing the slippage of the rebar and distorting the concrete elements instead. To overcome this phenomenon, another model with one-third of the COF value (0.167) was simulated as shown in the same figure. Despite the significant reduction in friction, the τ_{max} is more than 6 times higher than the experimental values obtained in [68]. Additionally, the friction plateau drops to zero at 5 mm slip, which is caused by the reduced COF as discussed in the previous chapter.

(a) Numerical results

(b) Experimental results [68]
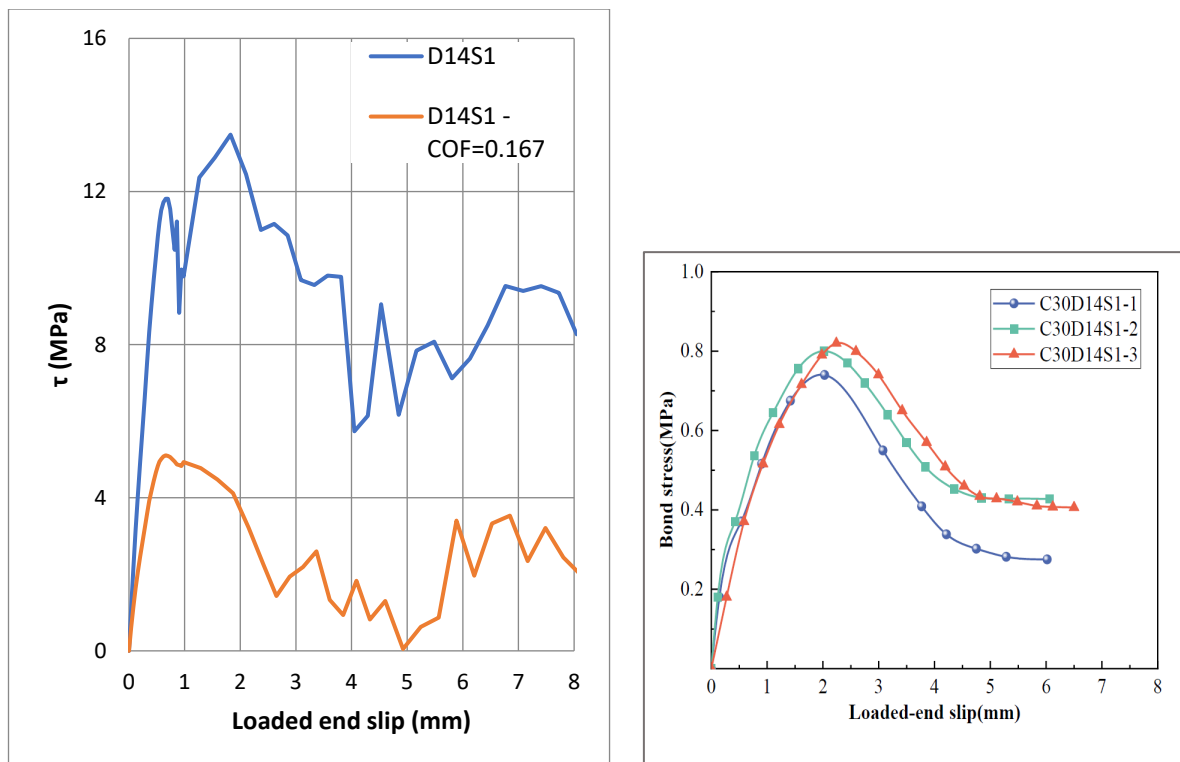
Figure 5.2: Bond stress-slip relationship of D14S1 rebar (sub-figures use different y-axis scales).

5.1.2. 'S2' Surface Geometry

Similarly, the results for D14S2 rebar type in Figure 5.3 (a) show a higher τ_{max} and lower s_1 compared to the experimental programs. The difference in bond stiffness is evident for the 14 mm rebar and will be tested for the rest of the specimens shown in Figure 5.3 (b) in the upcoming section.

(a) Numerical result   (b) Experimental result [68]
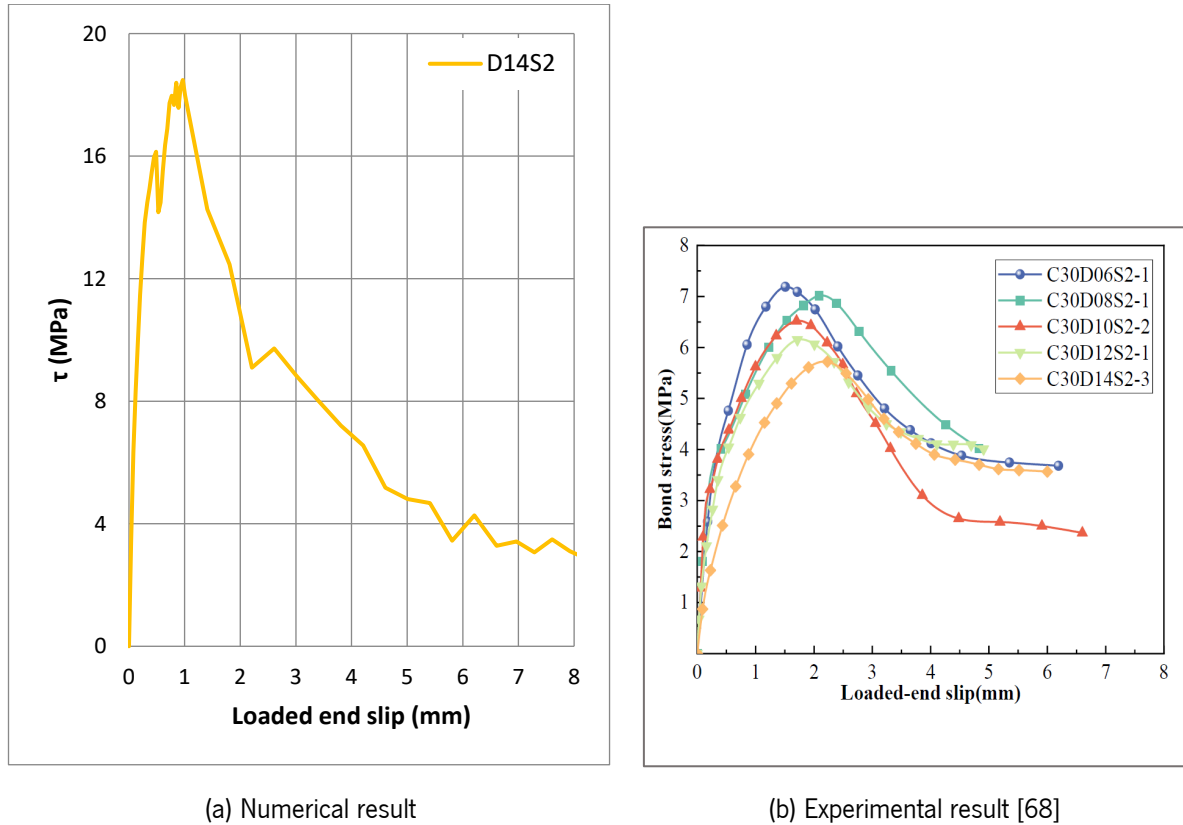
Figure 5.3: Bond stress-slip relationship of D14S2 rebar (sub-figures use different y-axis scales).

5.1.3. Indented Surface Geometry

Next, the rebar specimen with an indented surface configuration, shown in Figure 5.4 (a), is modelled. The three GFRP rebar types from the previous experimental program featured surface ribs created by wrapping fibre rovings around the core prior to curing. In contrast, the newly examined rebars are manufactured using a different method: their surface deformations are formed by machining grooves directly into the cured bar core. Moreover, the rebars are manufactured with thermoplastic resin as matrix material. These result in a distinct surface geometry and bonding profile, potentially leading to different mechanical properties and bond behaviours, which may be more accurately captured by the model.

The indented rebar was modelled with rectangular rib projections featuring 45° chamfered edges, as shown in Figure 5.4 (b). This geometric representation was selected based on the rebar image provided. Two types of rebar, differing in rib geometry and diameter as detailed in Table 5.2, were modelled. The

concrete used in the experimental program had a measured compressive strength of 37.5 MPa. Accordingly, the input parameters for the CDP model were calculated based on the procedure described in the previous chapter, using the EC2 guidelines and the CDP generator.
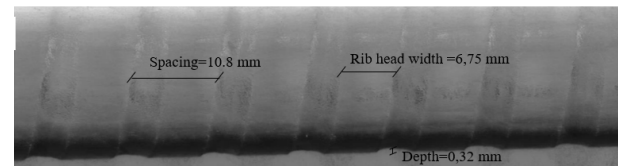
(a) Image analysis of surface from [10]

(b) Modelled rebar geometry

Figure 5.4: M1-D16 rebar surface deformation geometry.

Table 5.2: Rib geometry dimensions of indented rebar series studied in [10].

Rebar Series	Diameter (mm)	Rib Width (mm)	Rib Spacing (mm)	Rib Depth (mm)
M1	12	4.98	10.70	0.70
	16	6.75	10.80	0.32

The results in Figure 5.5 show the same limitation discussed earlier, with higher τ_{max} in the results of the numerical simulations, while s_1 is higher than that of the experimental curves.
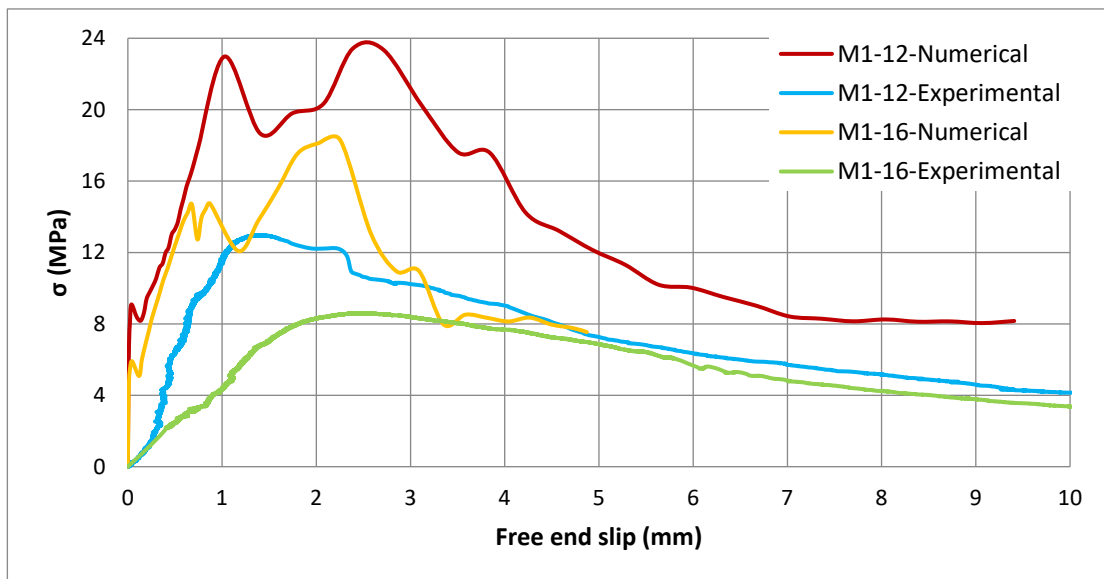
Figure 5.5: Comparison of numerical and experimental bond stress-slip relationship of indented rebar specimens

From the results, it can be seen from the experimental stress-slip relationships that the value of s_1 for the smaller diameter rebar (M1-12) is smaller than that of the larger diameter rebar (M1-16). However, the opposite can be observed from the numerical results with a greater s_1 value for the M1-12 rebar. The pattern in the experimental curve can also be seen in the previously studied relationship in Figure 5.3 (b). The opposite behaviour captured in the recent simulations could either be another limitation of the model or due to the different rib geometries of the two rebars. This will be further studied in the next section.

5.2. Bar Diameter

In this section, the compatibility of the model for various rebar diameters with the same rib geometry is investigated. To do this, the S2 rebar type from [68] studied earlier will be used. The rebar type was experimented with diameters of 6, 8, 10, 12, and 14 mm, all of which have the exact rib geometries as the one mentioned in Table 5.1. However, the elastic moduli of the various rebars differ, with smaller diameter rebars having a lower modulus as they are more prone to manufacturing defects compared to larger diameters [72]. The respective longitudinal elastic modulus for each rebar diameter listed in Table 5.3 was used in combination with the same engineering constants assumed for the previous simulations, as they are not stated in the article. Moreover, the anchor lengths used in the experimental program based on the provisions of ACI 440.3R-04 [17] were also modelled accordingly.

Table 5.3: Modelling parameters of each rebar diameter studied.

Rebar Type	Diameter (mm)	Elastic Modulus (MPa)	Anchor Length (mm)
	6	46,100	50
	8	47,160	50
S2	10	46,840	50
	12	48,210	60
	14	50,710	70

The results of these simulations are shown in Figure 5.6 (a). The discrepancy in τ_{max} between the numerical simulations and experimental results is evident across all rebar diameters. This difference in τ_{max} varies with diameter, with the ratio of simulated to experimental peak stress decreasing as the diameter increases, specifically, 5.1, 4.2, 3.8, 3.6, and 3.2 for 6-, 8-, 10-, 12-, and 14-mm rebars, respectively. Furthermore, the trend of increasing s_1 with decreasing rebar diameter, as observed in the previous section, persists, indicating a limitation of the current model.

This limitation could be caused by the assumed material properties for the rebar, such as the radial stiffness, Poisson's ratio, and shear stiffness, as they all might affect the pull-out behaviour. Hence, the effect of these parameters will be studied in the next section.

(a) Numerical results   (b) Experimental results [68]
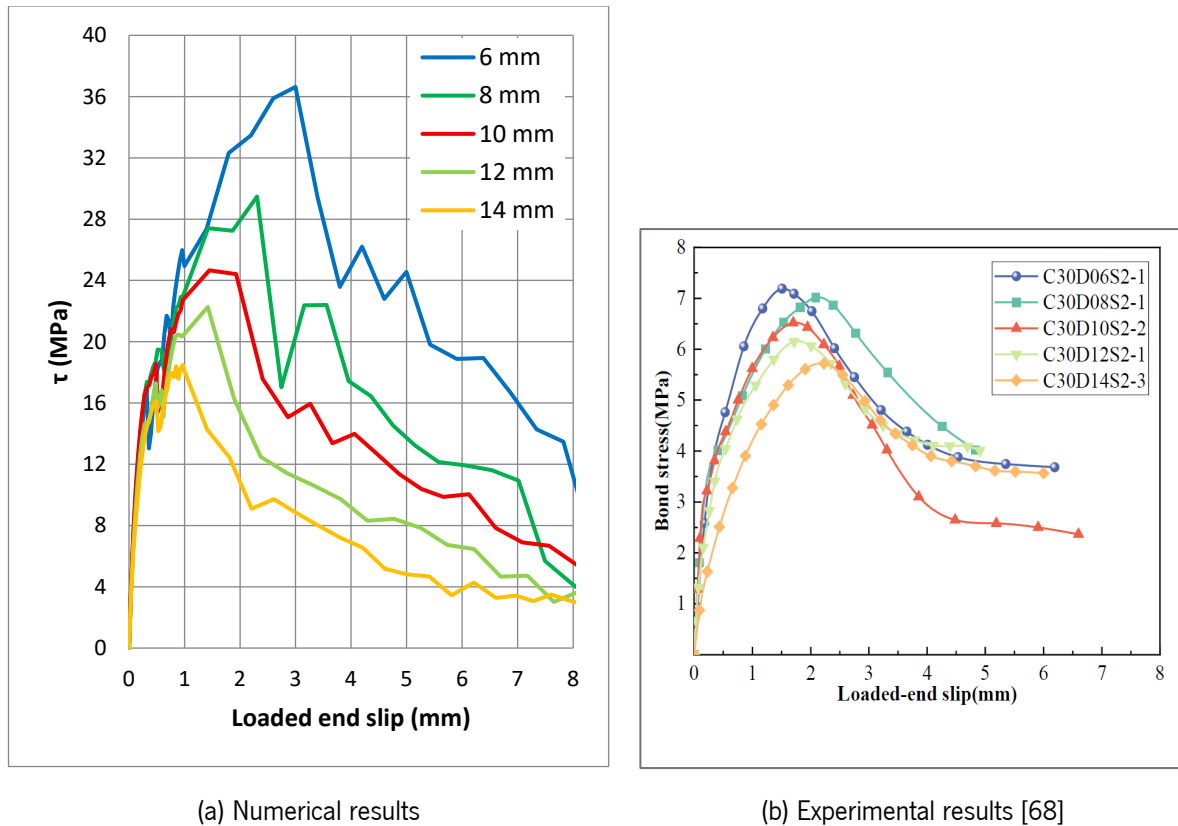
Figure 5.6: Comparison of bond stress-slip relationships for various rebar diameters.

5.3. Bar Elastic Properties

To study the effect of various GFRP material properties, three sets of simulations were run as listed in Table 5.4. The first set was to study the transverse stiffness parameter, while the second set was to study the effect of the Poisson's ratio. Note that in the material properties obtained from [13], the ν_{12} and ν_{13} have different values despite axis-1 being the longitudinal direction. Since GFRP rebars are transversely orthotropic, the material inputs for the second set were adjusted such that the two aforementioned parameters are equal. Lastly, the third set's aim was to study the shear stiffness parameters. The trials were run on the (D06S2) model for the rebar with a 6 mm diameter from the previous section.

The results of these trials all yielded the same pattern, showing minor variations within each set, but displaying the same overall bond behaviour. The bond stress-slip relationship obtained from this numerical model is hence not dependent on any of the GFRP material parameters studied.

Table 5.4: Engineering constants input for various trials.

Set	E1 (MPa)	E2 (MPa)	E3 (MPa)	ν_{12}	ν_{13}	ν_{23}	G12 (MPa)	G13 (MPa)	G23 (MPa)
Base	46,100	17,500	17,500	0.3	0.2	0.2	8,000	8,000	8,000
1	46,100	*14,000*	*14,000*	0.3	0.2	0.2	8,000	8,000	8,000
	46,100	*10,500*	*10,500*	0.3	0.2	0.2	8,000	8,000	8,000
	46,100	*7,000*	*7,000*	0.3	0.2	0.2	8,000	8,000	8,000
	46,100	*3,500*	*3,500*	0.3	0.2	0.2	8,000	8,000	8,000
2	46,100	17,500	17,500	*0.15*	*0.15*	*0.3*	8,000	8,000	8,000
	46,100	17,500	17,500	*0.2*	*0.2*	*0.3*	8,000	8,000	8,000
	46,100	17,500	17,500	*0.25*	*0.25*	*0.3*	8,000	8,000	8,000
	46,100	17,500	17,500	*0.3*	*0.3*	*0.3*	8,000	8,000	8,000
3	46,100	17,500	17,500	0.3	0.2	0.2	*5,000*	*5,000*	*5,000*
	46,100	17,500	17,500	0.3	0.2	0.2	*2,000*	*2,000*	5,000

5.4. Concrete Specimen Dimensions

The concrete specimen dimensions currently used in the model are 150 mm in length and 150 mm in diameter. In this section, two sets of simulations will be run: one for studying the effect of changing the concrete length, and the other for studying the effect of changing the concrete specimen diameter. Lengths of 120, 130, and 140 mm will be modelled, and diameters of 105, 120, 130, and 140 mm. The simulations are run on the same D06S2 specimen model from section 5.2.

The results of the first set demonstrated only minor differences in the observed relationships, indicating consistent overall behaviour. In contrast, the second set of results, as illustrated in Figure 5.7, revealed a trend of decreasing τ_{max} with decreasing specimen diameter. While the underlying cause of this pattern remains unclear, one possible explanation is the reduction in isostatic confinement stresses from the concrete support as the specimen diameter decreases.

Following the parametric study, the overestimation of τ_{max} and discrepancies in s_1 remain evident in the results. A stout methodology to address these discrepancies remains to be established. These limitations appear to stem from the model itself and are beyond the scope of the measures undertaken in this study. One possible cause of the high τ_{max} could be the residual stiffness of the concrete after failure. As previously mentioned, this residual stiffness helps to reproduce the friction plateau, but it may also result

in a load-bearing response that does not exist in experimental observations, as crushed concrete does not transmit stresses in the same way.
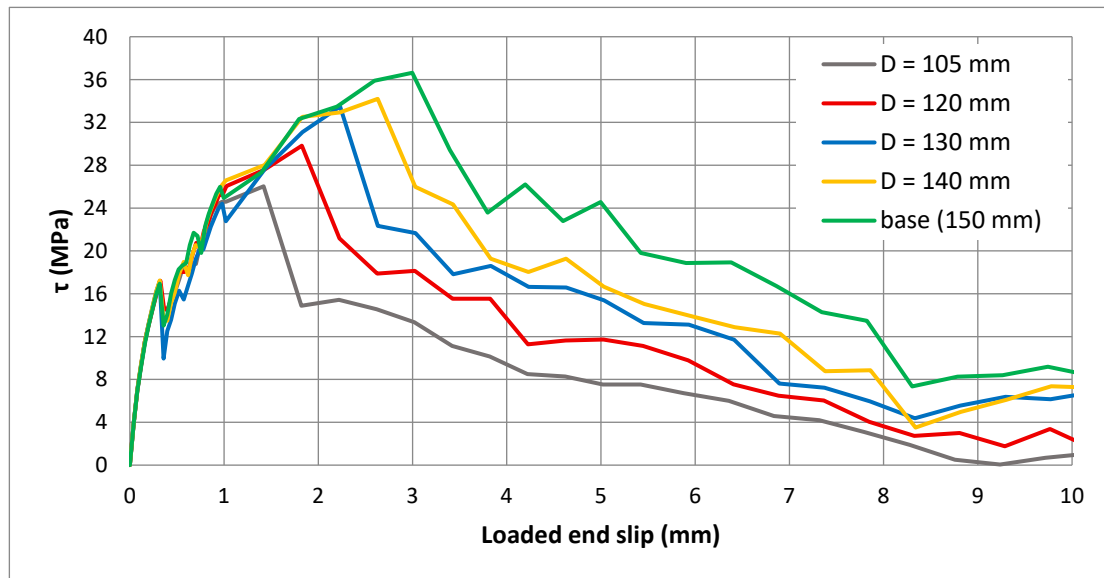
Figure 5.7: Comparison of bond stress-slip relationships for various concrete specimen diameters.

Table 5.5 summarises the mechanical and physical parameters studied and their impact on the various aspects of the bond stress-slip relationship, namely, τ_{max}, s_1, and friction plateau. Despite the model's limitations, the results of the parametric study highlight the dominant influence of rebar geometry and diameter on the bond stress-slip response, with surface configuration being a primary driver of τ_{max} variation across all specimens. This highlights the necessity of standardising the manufacturing process to improve the understanding of bond mechanisms and to support more consistent design procedures. In contrast, variations in concrete specimen dimensions and GFRP elastic properties had a comparatively modest impact, suggesting that model sensitivity is highest to surface-level mechanical interlock parameters. These findings reinforce the importance of accurately capturing rib geometry and highlight the limitations of applying a single bond model across varying rebar types. Together, these observations provide clear guidance for tailoring finite element models for GFRP-reinforced concrete and underscore the potential of the developed approach for generalisation, provided appropriate geometric detail is retained.

Table 5.5: Qualitative impact of mechanical parameters on key aspects of the bond stress-slip relationship.

Parameter	Impact on τ_{max}	Impact on s_1	Impact on Friction Plateau
Rebar Surface Geometry	Medium	High	High
Rebar Diameter	High	High	Medium
Rebar Mechanical Properties	*No Impact*	*No Impact*	*No Impact*
Concrete Length	*No Impact*	*No Impact*	*No Impact*
Concrete Diameter	Medium	Medium	Medium

THIS PAGE WAS INTENTIONALLY LEFT BLANK

6. Conclusions and Further Developments

6.1. Main Conclusions

This dissertation developed an axisymmetric finite element model in Abaqus to simulate the bond behaviour between GFRP rebars and concrete in pull-out tests. The primary objective was to characterise this interfacial behaviour with minimal reliance on extensive experimental data, while focusing on ribbed/indented GFRP rebars.

An axisymmetric numerical model was established, utilising engineering constants for GFRP rebars and the CDP model for concrete's non-linear behaviour. The model underwent rigorous calibration, particularly concerning the definition of concrete's tensile softening and compressive inelastic behaviours, which were found to significantly influence the bond stress-slip relationship. The following key aspects can be concluded from the work carried out:

- Several modelling parameters were modified to improve the stability of the model, such as mesh refinement and loading rate. Initial simulations highlighted the critical role of mesh compatibility, element shape, and loading rate in achieving stable damage propagation and a well-defined post-peak response. The transition to triangular elements and the implementation of a smooth-step amplitude significantly improved the stability of the model's behaviour.

- The study demonstrated the profound influence of the CDP model's input parameters, especially the maximum values for d_c and d_t, on the bond stress-slip curve. Calibrating these parameters using tools like the CDP Generator, while adapting them to match expected concrete behaviour, was crucial for obtaining more realistic responses.

- Sensitivity analyses revealed that ψ notably affects τ_{max} and s_1, with higher values generally leading to increased τ_{max} and decreased s_1. Conversely, μ had no impact on the overall bond stress-slip relationship within the tested range.

- The unbonded length of the rebar was identified as a significant factor influencing the accumulation of elastic energy and overall bond behaviour. Simplifying the rebar geometry by removing the unbonded part was essential for improving the descending branch definition and reducing computational effort.

- The coefficient of friction played a direct role in defining both the τ_{max} and the friction plateau, with lower COF values leading to reduced strength and earlier cut-offs in the bond-slip curve.

65

- The bond stress-slip relationship was found to be largely independent of the GFRP rebar's transverse stiffness, Poisson's ratio, and shear stiffness within the tested ranges, suggesting that the mechanical interlock and concrete properties are more dominant in this modelling approach.

However, despite the extensive calibrations and improvements in the stability of the model, several limitations persisted throughout the study:

- While the model successfully captured the general shape of the bond stress-slip curve, a consistent overestimation of the $\tau_{\max}$ and discrepancies in s_1 were observed when compared to experimental data, particularly for smaller diameter rebars.

- The parametric study on various ribbed and indented rebar geometries indicated that the model's accuracy varies with rib configuration, with some geometries exhibiting an unrealistic second peak or significant deviations from experimental results.

- The model showed a limitation in accurately predicting the trend of s_1 with varying rebar diameters, often showing an increasing s_1 with decreasing diameter, contrary to experimental observations.

In summary, the developed axisymmetric model provides a robust framework for simulating the bond behaviour of ribbed/indented GFRP rebars in concrete, offering valuable insights into the influence of various material and geometric parameters. However, further refinements are necessary to enhance its predictive accuracy across a broader range of rebar types and to fully capture the complex interplay of factors governing the bond-slip mechanism.

6.2. Further Developments

Building upon the insights and limitations identified in this study, the following areas are recommended for future research to further enhance the predictive capabilities and applicability of numerical models for GFRP rebar-concrete bond behaviour:

- Conduct a dedicated study on the fundamental reasons behind the observed limitations in predicting the s_1 trend with varying rebar diameters. This might involve a deeper investigation into the scale effect on bond, potentially considering concrete confinement, and the relative stiffness of the rebar to the surrounding concrete for different diameters.

- Calibrate the model into a 3-D modelling space and use it to better understand the model limitations. The current model exhibits computational inefficiencies when implemented in 3-D, even when double-symmetry is used in modelling.

- Expand the model's capabilities to explicitly capture other critical failure mechanisms, such as rebar deformation shear-off or squeeze-through. This would require careful consideration of the interlaminar shear strength of the GFRP rebar, which was not the primary focus of this axisymmetric pull-out model. A simplified approach would be modelling the surface deformation and the inner core as separate parts connected by a calibrated cohesive law.

- Generate a comprehensive, standardised database of GFRP rebar-concrete bond test results, covering a wide range of rebar geometries, diameters, and concrete strengths. This database would be invaluable for rigorous validation and further calibration of numerical models.

THIS PAGE WAS INTENTIONALLY LEFT BLANK

REFERENCES

[1]   M. Seis and A. Beycioğlu, 'Bond performance of basalt fiber-reinforced polymer bars in conventional Portland cement concrete: A relative comparison with steel rebar using the hinged beam approach', *Science and Engineering of Composite Materials*, vol. 24, no. 6, pp. 909–918, Nov. 2017, doi: 10.1515/secm-2015-0210.

[2]   'Concrete: Building Pathology - Google Books'. Accessed: May 28, 2025. [Online]. Available: https://books.google.es/books?hl=en&lr=&id=OXz2WK9jFuYC&oi=fnd&pg=PA15&dq=concrete+rebar+materials+throughout+history&ots=y8TYb7jPjK&sig=Uqj7ckq0QUriarUxH7jzEoOg-8s&redir_esc=y#v=onepage&q=concrete%20rebar%20materials%20throughout%20history&f=false

[3]   H. Oh, J. Sim, T. Kang, and H. Kwon, 'An experimental study on the flexural bonding characteristic of a concrete beam reinforced with a GFRP rebar', *KSCE Journal of Civil Engineering*, vol. 15, no. 7, pp. 1245–1251, Sep. 2011, doi: 10.1007/s12205-011-1018-y.

[4]   L. Wu, X. Xu, H. Wang, and J. Q. Yang, 'Experimental study on bond properties between GFRP bars and self-compacting concrete', *Constr Build Mater*, vol. 320, Feb. 2022, doi: 10.1016/j.conbuildmat.2021.126186.

[5]   A. Rolland, M. Quiertant, A. Khadour, S. Chataigner, K. Benzarti, and P. Argoul, 'Experimental investigations on the bond behavior between concrete and FRP reinforcing bars', *Constr Build Mater*, vol. 173, pp. 136–148, Jun. 2018, doi: 10.1016/j.conbuildmat.2018.03.169.

[6]   N. Saleh, A. Ashour, D. Lam, and T. Sheehan, 'Experimental investigation of bond behaviour of two common GFRP bar types in high – Strength concrete', *Constr Build Mater*, vol. 201, pp. 610–622, Mar. 2019, doi: 10.1016/j.conbuildmat.2018.12.175.

[7]   H. Mazaheripour, J. A. O. Barros, J. M. Sena-Cruz, M. Pepe, and E. Martinelli, 'Experimental study on bond performance of GFRP bars in self-compacting steel fiber reinforced concrete', *Compos Struct*, vol. 95, pp. 202–212, Jan. 2013, doi: 10.1016/j.compstruct.2012.07.009.

[8]   N. Zemour, A. Asadian, E. A. Ahmed, K. H. Khayat, and B. Benmokrane, 'Experimental study on the bond behavior of GFRP bars in normal and self-consolidating concrete', *Constr Build Mater*, vol. 189, pp. 869–881, Nov. 2018, doi: 10.1016/j.conbuildmat.2018.09.045.

[9]   T. D'Antino, V. Bertolli, M. A. Pisani, and C. Poggi, 'Tensile and interlaminar shear behavior of thermoset and thermoplastic GFRP bars exposed to alkaline environment', *Journal of Building Engineering*, vol. 72, Aug. 2023, doi: 10.1016/j.jobe.2023.106581.

[10]   M. Fodda *et al.*, 'Experimental Investigation on the Bond Behavior between Thermoplastic GFRP Rebars And Concrete', in *CICE2025 – 12th International Conference on Fiber-Reinforced Polymer (FRP) Composites in Civil Engineering*, Lisbon, Portugal, Jul. 2025.

[11]   R. Kotynia, D. Szczech, and M. Kaszubska, 'Bond Behavior of GRFP Bars to Concrete in Beam Test', in *Procedia Engineering*, Elsevier Ltd, 2017, pp. 401–408. doi: 10.1016/j.proeng.2017.06.230.

[12]   H. Jin, Q. Chun, C. Zhang, and Y. Han, 'A durability prediction method for historical square rebar reinforced concrete buildings', *Applied Sciences (Switzerland)*, vol. 11, no. 24, Dec. 2021, doi: 10.3390/app112411737.

[13]   C. Bai, J. Xue, and Z. Luo, 'Experimental and finite element study on bond behavior between GFRP bar and recycled aggregate concrete', *Constr Build Mater*, vol. 456, Dec. 2024, doi: 10.1016/j.conbuildmat.2024.139241.

[14]   J. A. Rami Hamad, M. A. Megat Johari, and R. H. Haddad, 'Mechanical properties and bond characteristics of different fiber reinforced polymer rebars at elevated temperatures', *Constr Build Mater*, vol. 142, pp. 521–535, Jul. 2017, doi: 10.1016/j.conbuildmat.2017.03.113.

[15]   G. Trabacchin, W. Sebastian, and M. Zhang, 'Experimental and analytical study of bond between basalt FRP bars and geopolymer concrete', *Constr Build Mater*, vol. 315, Jan. 2022, doi: 10.1016/j.conbuildmat.2021.125461.

[16]   M. Baena, L. Torres, A. Turon, and C. Barris, 'Experimental study of bond behaviour between concrete and FRP bars using a pull-out test', *Compos B Eng*, vol. 40, no. 8, pp. 784–797, Dec. 2009, doi: 10.1016/j.compositesb.2009.07.003.

[17]   ACI Committee 440, 'ACI 440.3R-04: Guide Test Methods for Fiber-Reinforced Polymers (FRPs) for Reinforcing or Strengthening Concrete Structures', Farmington Hills, MI, Jun. 2004.

[18]   Rilem, 'RC6 Bond test for reinforcement steel. 2. Pull-out test', *RILEM Technical Recommendations for the testing and use of construction materials*, pp. 627–629, Jul. 2020, doi: 10.1201/9781482271362-157/RC6-BOND-TEST-REINFORCEMENT-STEEL-2-PULL-TEST-RILEM.

[19]   BS EN 10080:2005, *Steel for the reinforcement of concrete - weldable reinforcing steel - general, Annex D: Determination of bond strength – Pull-out test.* Brussels: European Committee for Standardization (CEN), 2005.

[20]   A. Rolland, K. Benzarti, M. Quiertant, and S. Chataigner, 'Accelerated aging behavior in alkaline environments of gfrp reinforcing bars and their bond with concrete', *Materials*, vol. 14, no. 19, Oct. 2021, doi: 10.3390/ma14195700.

[21]   Task Group 9.3, 'fib Bulletin No. 40: FRP reinforcement in RC structures', International Federation for Structural Concrete, Sep. 2007.

[22]   S. Sólyom, M. Di Benedetti, and G. L. Balázs, 'Effect of Surface Characteristics of FRP Bars on Bond Behavior in Concrete', 2017. [Online]. Available: https://www.researchgate.net/publication/333670843

[23]   M. B. Muñoz, 'Study of Bond Behaviour between FRP Reinforcement and Concrete', PhD Thesis, Universitat de Girona, Girona, 2010. [Online]. Available: http://hdl.handle.net/10803/7771

[24]   F. Sayed Ahmad, G. Foret, and R. Le Roy, 'Bond between carbon fibre-reinforced polymer (CFRP) bars and ultra high performance fibre reinforced concrete (UHPFRC): Experimental study', *Constr Build Mater*, vol. 25, no. 2, pp. 479–485, Feb. 2011, doi: 10.1016/j.conbuildmat.2010.02.006.

[25]   Task Group Bond Models (former CEB Task Group 2.5), 'fib Bulletin No. 10: Bond of reinforcement in concrete', Aug. 2000.

[26]   A. Rolland, P. Argoul, K. Benzarti, M. Quiertant, S. Chataigner, and A. Khadour, 'Analytical and numerical modeling of the bond behavior between FRP reinforcing bars and concrete', *Constr Build Mater*, vol. 231, Jan. 2020, doi: 10.1016/j.conbuildmat.2019.117160.

[27]   J. Shafaie, A. Hosseini, and M. S. Marefat, '3D Finite Eelement Modelling of Bond-slip between Rebar and Concrete in Pull-out Test', Apr. 2009.

[28]   H. F. S. G. Pereira, V. M. C. F. Cunha, and J. Sena-Cruz, 'Numerical simulation of galvanized rebars pullout', *Frattura ed Integrita Strutturale*, vol. 31, pp. 54–66, Jan. 2015, doi: 10.3221/IGF-ESIS.31.05.

[29]   S. Lettow, R. Eligehausen, and J. Ožbolt, 'The simulation of bond between concrete and reinforcement in nonlinear three-dimensional finite element analysis.', in *5th International PhD Symposium in Civil Engineering*, Delft, The Netherlands, 2004, pp. 16–19. Accessed: Jun. 26, 2025. [Online]. Available: https://scholar.google.com/scholar?hl=en&as_sdt=0%2C5&q=the+simulation+of+bond+between+concrete+and+reinforcement+in+nonlinear+three-

dimensional+finite+element+analysis&btnG=#d=gs_cit&t=1750945502298&u=%2Fscholar%3Fq%3Dinfo%3AflJXVVfVi-8J%3Ascholar.google.com%2F%26output%3Dcite%26scirp%3D0%26hl%3Den

[30] 'Abaqus - SIMULIA User Assistance 2022'. Accessed: Apr. 29, 2025. [Online]. Available: https://help.3ds.com/2022/english/dssimulia_established/SIMULIA_Established_Frontmatter Map/sim-r-DSDocAbaqus.htm?contextscope=all&id=ec01bc8c83d743a6a30123c5a034edca

[31] Z. Achillides and K. Pilakoutas, 'FE modelling of bond interaction of FRP bars to concrete', *Structural Concrete*, vol. 7, no. 1, pp. 7–16, Mar. 2006, doi: 10.1680/stco.2006.7.1.7.

[32] ACI Committee 408, 'ACI 408R-03: Bond and Development of Straight Reinforcing Bars in Tension', Farmington Hills, MI, Sep. 2003.

[33] A. F. Al-Khafaji, J. J. Myers, and H. H. Alghazali, 'Evaluation of bond performance of glass fiber rebars embedded in sustainable concrete', *J Clean Prod*, vol. 282, Feb. 2021, doi: 10.1016/j.jclepro.2020.124516.

[34] M. Burdziński and M. Niedostatkiewicz, 'Experimental-Numerical Analysis of the Effect of Bar Diameter on Bond in Pull-Out Test', *Buildings*, vol. 12, no. 9, Sep. 2022, doi: 10.3390/buildings12091392.

[35] I. C. Rosa, J. P. Firmo, J. R. Correia, and P. Mazzuca, 'Influence of elevated temperatures on the bond behaviour of ribbed GFRP bars in concrete', *Cem Concr Compos*, vol. 122, Sep. 2021, doi: 10.1016/j.cemconcomp.2021.104119.

[36] M. Baena, L. Torres, A. Turon, M. Llorens, and C. Barris, 'Bond behaviour between recycled aggregate concrete and glass fibre reinforced polymer bars', *Constr Build Mater*, vol. 106, pp. 449–460, Mar. 2016, doi: 10.1016/j.conbuildmat.2015.12.145.

[37] A. Jafari, A. A. Shahmansouri, H. A. Abdulridha, B. I. Issa, and H. A. Bengar, 'Effect of CFRP confinement on bond-slip behavior of steel rebar in low-strength concrete: Experimentation, prediction and parametric study', *Constr Build Mater*, vol. 477, May 2025, doi: 10.1016/j.conbuildmat.2025.141333.

[38] L. Chen, K. Liang, and Z. Shan, 'Experimental and theoretical studies on bond behavior between concrete and FRP bars with different surface conditions', *Compos Struct*, vol. 309, Apr. 2023, doi: 10.1016/j.compstruct.2023.116721.

[39] L. Huang, J. Chen, J. Qu, and Q. Dai, 'Modeling for bond-constitutive relationships of FRP rebars to concrete matrix', *Constr Build Mater*, vol. 263, Dec. 2020, doi: 10.1016/j.conbuildmat.2020.120654.

[40] L. J. Malvar, 'Bond Stress–Slip Characteristics of FRP Rebars', Port Hueneme, CA, Feb. 1994.

[41] R. Elighausen, E. P. Popov, and V. V. Bertero, 'Local Bond Stress-Slip Relationships of Deformed Bars under Generalized Excitations', 1983.

[42] V. A. Rossetti, D. Galeota, and M. M. Giammatteo, 'Local bond stress-slip relationships of glass fibre reinforced plastic bars embedded in concrete', *Mater Struct*, vol. 28, no. 6, pp. 340–344, Jul. 1995, doi: 10.1007/BF02473149.

[43] E. Cosenza, G. Manfredi, and R. Realfonzo, 'Analytical modelling of bond between FRP reinforcing bars and concrete', in *Non-Metallic (FRP) Reinforcement for Concrete Structures: Proceeding of the Second International RILEM Symposium*, L. Taerwe, Ed., E & FN SPON, Jan. 1995, pp. 164–171. [Online]. Available: https://www.researchgate.net/publication/262259677

[44] X. Lin and Y. X. Zhang, 'Evaluation of bond stress-slip models for FRP reinforcing bars in concrete', *Compos Struct*, vol. 107, no. 1, pp. 131–141, Jan. 2014, doi: 10.1016/j.compstruct.2013.07.037.

[45] E. Cosenza, G. Manfredi, and R. Realfonzo, 'Behavior and Modeling of Bond of FRP Rebars to Concrete', in *Journal of Composites for Construction*, American Society of Civil Engineers, May 1997, pp. 40–51. doi: 10.1061/(ASCE)1090-0268(1997)1:2(40).

[46] B. Tighiouart, B. Benmokrane, and D. Gao, 'Investigation of bond in concrete member with fibre reinforced polymer FRP bars', 1998.

[47] S. Solyom and G. L. Balázs, 'Analytical and statistical study of the bond of FRP bars with different surface characteristics', *Compos Struct*, vol. 270, Aug. 2021, doi: 10.1016/j.compstruct.2021.113953.

[48] L. Huang, J. Chen, J. Qu, and Q. Dai, 'Modeling for bond-constitutive relationships of FRP rebars to concrete matrix', *Constr Build Mater*, vol. 263, Dec. 2020, doi: 10.1016/j.conbuildmat.2020.120654.

[49] W. Wei, F. Liu, Z. Xiong, Z. Lu, and L. Li, 'Bond performance between fibre-reinforced polymer bars and concrete under pull-out tests', *Constr Build Mater*, vol. 227, Dec. 2019, doi: 10.1016/j.conbuildmat.2019.116803.

[50] G. Trabacchin, W. Sebastian, and M. Zhang, 'Experimental and analytical study of bond between basalt FRP bars and geopolymer concrete', *Constr Build Mater*, vol. 315, Jan. 2022, doi: 10.1016/j.conbuildmat.2021.125461.

[51] Q.-W. Zheng and W.-C. Xue, 'Constitutive relationship of bond-slip behavior of sand-coated deformed GFRP rebars', *Gong cheng Li xue/Engineering Mechanics*, no. 25, pp. 162–169, 2008.

[52] A. Denisiewicz, M. Kuczma, K. Kula, and T. Socha, 'Influence of boundary conditions on numerical homogenization of high performance concrete', *Materials*, vol. 14, no. 4, pp. 1–18, Feb. 2021, doi: 10.3390/MA14041009,.

[53] O. Gooranorimi, W. Suaris, and A. Nanni, 'A model for the bond-slip of a GFRP bar in concrete', *Eng Struct*, vol. 146, pp. 34–42, Sep. 2017, doi: 10.1016/j.engstruct.2017.05.034.

[54] E. El Alami *et al.*, 'Numerical Study of the Bond Strength Evolution of Corroded Reinforcement in Concrete in Pull-Out Tests', *Applied Sciences (Switzerland)*, vol. 12, no. 2, Jan. 2022, doi: 10.3390/app12020654.

[55] A. Qasem, Y. S. Sallam, H. Hossam Eldien, and B. H. Ahangarn, 'Bond-slip behavior between ultra-high-performance concrete and carbon fiber reinforced polymer bars using a pull-out test and numerical modelling', *Constr Build Mater*, vol. 260, Nov. 2020, doi: 10.1016/j.conbuildmat.2020.119857.

[56] A. Sharma, J. Bošnjak, J. Ožbolt, and J. Hofmann, 'Numerical modeling of reinforcement pull-out and cover splitting in fire-exposed beam-end specimens', *Eng Struct*, vol. 111, pp. 217–232, Mar. 2016, doi: 10.1016/j.engstruct.2015.12.017.

[57] I. C. Rosa, M. R. T. Arruda, J. P. Firmo, and J. R. Correia, 'Bond Behavior of Straight and Bent Glass Fiber–Reinforced Polymer Bars at Elevated Temperatures: Pull-Out Tests and Numerical Simulations', *Journal of Composites for Construction*, vol. 26, no. 3, Jun. 2022, doi: 10.1061/(asce)cc.1943-5614.0001213.

[58] M. Rezazadeh, V. Carvelli, and A. Veljkovic, 'Modelling bond of GFRP rebar and concrete', *Constr Build Mater*, vol. 153, pp. 102–116, Oct. 2017, doi: 10.1016/j.conbuildmat.2017.07.092.

[59] L. Molina *et al.*, 'Bond strength of galvanized steel: experimental and numerical study based on pull-out tests', in *3rd International Conference on Mechanical Models in Structural Engineering*, Seville, Spain, Jun. 2015, pp. 143–158.

[60] L. Henrique Pereira França, F. Estevão Damasceno Filho, M. Silva Medeiros Júnior, and A. Eduardo Bezerra Cabral, 'Experimental and Finite Element Analysis of Pullout Test on GFRP Rebars', in *XLI Ibero-Latin-American Congress on Computational Methods in Engineering, ABMEC*, Foz do Iguacu/Parana, Brazil, Nov. 2020.

[61] F. M. de Almeida Filho, S. De Nardin, and A. L. H. de C. El Debs, 'Numerical approach of the steel-concrete bond behavior using pull-out models', *Revista Materia*, vol. 24, no. 2, 2019, doi: 10.1590/s1517-707620190002.0656.

[62]   J. G. Stoner, 'Finite Element Modelling of GFRP Reinforced Concrete Beams', PhD Thesis, University of Waterloo, 2015. Accessed: May 04, 2025. [Online]. Available: https://uwspace.uwaterloo.ca/items/ff19ae6c-ce63-4a37-8ba2-d539e4d687e9

[63]   'Eurocode 2: Design of concrete structures-Part 1-1: General rules and rules for buildings', 2004.

[64]   R. Malm, 'Predicting shear type crack initiation and growth in concrete with non-linear finite element method', Thesis, Royal Institute of Technology, Stockholm, Sweden, 2009. [Online]. Available: https://www.researchgate.net/publication/265073350

[65]   J. Lee and G. L. Fenves, 'Plastic-Damage Model for Cyclic Loading of Concrete Structures', *J Eng Mech*, no. 124, pp. 892–900, Aug. 1998.

[66]   M. Z. Naser, R. A. Hawileh, and J. Abdalla, 'Modeling strategies of finite element simulation of reinforced concrete beams strengthened with frp: A review', 2021, *MDPI AG*. doi: 10.3390/jcs5010019.

[67]   X. Chang, G. Yue, H. Lin, and C. Tang, 'Modeling the pullout behavior of fiber reinforced polymer bars from concrete', *Constr Build Mater*, vol. 24, no. 4, pp. 431–437, Apr. 2010, doi: 10.1016/j.conbuildmat.2009.10.020.

[68]   F. Xie, W. Tian, P. Diez, S. Zlotnik, and A. G. Gonzalez, 'Bonding Performance of Glass Fiber-Reinforced Polymer Bars under the Influence of Deformation Characteristics', *Polymers (Basel)*, vol. 15, no. 12, Jun. 2023, doi: 10.3390/polym15122604.

[69]   ARC Insulations., 'GFRP Rebar Details.' Accessed: Apr. 03, 2025. [Online]. Available: https://chatgpt.com/c/686bc3ab-2730-8001-91f8-9a00bc18bf26

[70]   MaxComposites China., 'GFRP Rebar Technical Specifications.' Accessed: Apr. 03, 2025. [Online]. Available: https://maxcompositeschina.com/products/glass-fiber-rebargfrp-bar

[71]   GatorBar., 'Technical Resources.' Accessed: Apr. 03, 2025. [Online]. Available: https://maxcompositeschina.com/products/glass-fiber-rebargfrp-bar

[72]   O. Gooranorimi, W. Suaris, E. Dauer, and A. Nanni, 'Microstructural investigation of glass fiber reinforced polymer bars', *Compos B Eng*, vol. 110, pp. 388–395, Feb. 2017, doi: 10.1016/j.compositesb.2016.11.029.

[73]   S. M. Allam, M. S. Shoukry, G. E. Rashad, and A. S. Hassan, 'Evaluation of tension stiffening effect on the crack width calculation of flexural RC members', *Alexandria Engineering Journal*, vol. 52, no. 2, pp. 163–173, 2013, doi: 10.1016/j.aej.2012.12.005.

[74]   A. Elkady, 'ABAQUS_CDP_Generator: A tool for generating concrete damage parameters for ABAQUS', 2023, *Zenodo*: v23.04. doi: 10.5281/ZENODO.7755926.

[75]   'CEB-Fib Model Code 1990: Design Code', 1993.

[76]   'CEB-fib Model Code for Concrete Structures 2010', 2013.

ANNEX I. CDP MODEL INPUTS

Table A1.1: Results of calculations described in Chapter 3 for compressive behaviour.

Step	ε_c [‰]	η	σ_c [MPa]	ε_c^{el} [‰]	ε_c^{in} [‰]	d_c	ε_c^{pl} [‰]
1	0.42	-	13.20	0.42	0.00	0	0.00
2	0.52	0.251	14.82	0.47	0.05	0	0.05
3	0.62	0.299	17.14	0.54	0.07	0	0.07
4	0.72	0.348	19.30	0.61	0.11	0	0.11
5	0.82	0.396	21.30	0.68	0.14	0	0.14
6	0.92	0.444	23.13	0.73	0.18	0	0.18
7	1.02	0.493	24.80	0.79	0.23	0	0.23
8	1.12	0.541	26.31	0.84	0.28	0	0.28
9	1.22	0.589	27.66	0.88	0.34	0	0.34
10	1.32	0.638	28.86	0.92	0.40	0	0.40
11	1.42	0.686	29.90	0.95	0.47	0	0.47
12	1.52	0.734	30.79	0.98	0.54	0	0.54
13	1.62	0.783	31.52	1.00	0.62	0	0.62
14	1.72	0.831	32.11	1.02	0.70	0	0.70
15	1.82	0.879	32.55	1.03	0.79	0	0.79
16	1.92	0.928	32.84	1.04	0.88	0	0.88
17	2.02	0.976	32.98	1.05	0.97	0	0.97
18	2.12	1.024	32.98	1.05	1.07	0	1.07
19	2.22	1.072	32.84	1.04	1.18	0.005	1.17
20	2.32	1.121	32.55	1.03	1.29	0.013	1.27
21	2.42	1.169	32.13	1.02	1.40	0.026	1.37
22	2.52	1.217	31.57	1.00	1.52	0.043	1.47
23	2.62	1.266	30.86	0.98	1.64	0.065	1.57
24	2.72	1.314	30.03	0.95	1.77	0.090	1.67
25	2.82	1.362	29.05	0.92	1.90	0.120	1.77
26	2.92	1.411	27.95	0.89	2.03	0.153	1.87
27	3.02	1.459	26.71	0.85	2.17	0.191	1.97
28	3.12	1.507	25.34	0.81	2.31	0.232	2.07
29	3.22	1.556	23.84	0.76	2.46	0.278	2.17
30	3.32	1.604	22.21	0.71	2.61	0.327	2.27
31	3.42	1.652	20.46	0.65	2.77	0.380	2.37
32	3.50	1.691	18.95	0.60	2.90	0.426	2.45

Table A1.2: Results of calculations described in Chapter 3 for tensile behaviour.

Step	ε_t [‰]	σ_t [MPa]	ε_t^{el} [‰]	ε_t^{cr} [‰]	d_t	ε_t^{pl} [‰]
1	0	0	0	0.00	0	0.00
2	0.08149	2.6	0.08149	0.00	0	0.00
3	0.40745	0.9	0.027163	0.38	0.666667	0.33
4	1.30384	0.1	0.001589	1.30	0.99	1.14

Table A1.3: CDP inelastic behaviour parameter inputs from EC2 and [73].

Compressive Behaviour			Tensile Behaviour		
Yield Stress	Inelastic Strain	Damage Parameter	Yield Stress	Cracking Strain	Damage Parameter
13.20	0.00E+00	0.000	2.56	0.00E+00	0.000
14.82	4.86E-05	0.000	0.85	3.80E-04	0.667
17.14	7.48E-05	0.000	0.01	1.30E-03	0.990
19.30	1.06E-04	0.000	-	-	-
21.30	1.43E-04	0.000	-	-	-
23.13	1.85E-04	0.000	-	-	-
24.80	2.32E-04	0.000	-	-	-
26.31	2.84E-04	0.000	-	-	-
27.66	3.41E-04	0.000	-	-	-
28.86	4.03E-04	0.000	-	-	-
29.90	4.69E-04	0.000	-	-	-
30.79	5.41E-04	0.000	-	-	-
31.52	6.18E-04	0.000	-	-	-
32.11	6.99E-04	0.000	-	-	-
32.55	7.85E-04	0.000	-	-	-
32.84	8.76E-04	0.000	-	-	-
32.98	9.72E-04	0.000	-	-	-
32.98	1.07E-03	0.000	-	-	-
32.84	1.18E-03	0.005	-	-	-
32.55	1.29E-03	0.013	-	-	-
32.13	1.40E-03	0.026	-	-	-
31.57	1.52E-03	0.043	-	-	-
30.86	1.64E-03	0.065	-	-	-
30.03	1.77E-03	0.090	-	-	-
29.05	1.90E-03	0.120	-	-	-
27.95	2.03E-03	0.153	-	-	-
26.71	2.17E-03	0.191	-	-	-
25.34	2.31E-03	0.232	-	-	-
23.84	2.46E-03	0.278	-	-	-
22.21	2.61E-03	0.327	-	-	-
20.46	2.77E-03	0.380	-	-	-
18.95	2.90E-03	0.426	-	-	-

Table A1.4: CDP inelastic behaviour parameter inputs of modified EC2 with d_c = 0.98.

Compressive Behaviour			Tensile Behaviour		
Yield Stress	Inelastic Strain	Damage Parameter	Yield Stress	Cracking Strain	Damage Parameter
13.20	0.00E+00	0.000	2.56	0.00E+00	0.000
14.82	4.86E-05	0.000	1.71	1.90E-04	0.333
17.14	7.48E-05	0.000	0.96	4.48E-04	0.625
19.30	1.06E-04	0.000	0.43	8.42E-04	0.833
21.30	1.43E-04	0.000	0.29	1.29E-03	0.889
23.13	1.85E-04	0.000	-	-	-
24.80	2.32E-04	0.000	-	-	-
26.31	2.84E-04	0.000	-	-	-
27.66	3.41E-04	0.000	-	-	-
28.86	4.03E-04	0.000	-	-	-
29.90	4.69E-04	0.000	-	-	-
30.79	5.41E-04	0.000	-	-	-
31.52	6.18E-04	0.000	-	-	-
32.11	6.99E-04	0.000	-	-	-
32.55	7.85E-04	0.000	-	-	-
32.84	8.76E-04	0.000	-	-	-
32.98	9.72E-04	0.000	-	-	-
32.98	1.07E-03	0.000	-	-	-
32.84	1.18E-03	0.005	-	-	-
32.55	1.29E-03	0.013	-	-	-
32.13	1.40E-03	0.026	-	-	-
31.57	1.52E-03	0.043	-	-	-
30.86	1.64E-03	0.065	-	-	-
30.03	1.77E-03	0.090	-	-	-
29.05	1.90E-03	0.120	-	-	-
27.95	2.03E-03	0.153	-	-	-
26.71	2.17E-03	0.191	-	-	-
25.34	2.31E-03	0.232	-	-	-
23.84	2.46E-03	0.278	-	-	-
22.21	2.61E-03	0.327	-	-	-
20.46	2.77E-03	0.380	-	-	-
18.95	2.90E-03	0.426	-	-	-
17.64	2.95E-03	0.465	-	-	-
16.33	2.99E-03	0.505	-	-	-
15.02	3.04E-03	0.545	-	-	-
13.71	3.08E-03	0.585	-	-	-
12.40	3.13E-03	0.624	-	-	-
11.09	3.18E-03	0.664	-	-	-
9.78	3.22E-03	0.704	-	-	-
8.47	3.27E-03	0.743	-	-	-
7.16	3.32E-03	0.783	-	-	-
5.85	3.36E-03	0.823	-	-	-
4.54	3.41E-03	0.862	-	-	-
3.23	3.46E-03	0.902	-	-	-
1.92	3.50E-03	0.942	-	-	-
0.61	3.55E-03	0.982	-	-	-

**Table A1.5:** CDP inelastic behaviour parameter inputs of CDP generator – MT.

Compressive Behaviour			Tensile Behaviour		
Yield Stress	Inelastic Strain	Damage Parameter	Yield Stress	Cracking Strain	Damage Parameter
13.20	0.00E+00	0.000	2.56	0.00E+00	0.000
14.91	2.11E-05	0.000	2.50	1.09E-05	0.022
18.85	6.38E-05	0.000	1.87	5.04E-05	0.269
22.29	1.24E-04	0.000	1.42	8.98E-05	0.447
25.23	2.01E-04	0.000	1.13	1.29E-04	0.557
27.69	2.95E-04	0.000	0.95	1.69E-04	0.630
29.68	4.05E-04	0.000	0.75	2.50E-04	0.707
31.19	5.32E-04	0.000	0.64	3.17E-04	0.750
32.25	6.74E-04	0.000	0.56	3.70E-04	0.782
32.84	8.33E-04	0.000	0.49	4.23E-04	0.808
32.99	1.01E-03	0.000	0.43	4.76E-04	0.831
32.70	1.20E-03	0.009	0.38	5.29E-04	0.852
31.98	1.40E-03	0.031	0.33	5.82E-04	0.872
30.83	1.62E-03	0.066	-	-	-
29.26	1.85E-03	0.113	-	-	-
27.28	2.10E-03	0.173	-	-	-
24.89	2.36E-03	0.246	-	-	-
22.10	2.64E-03	0.330	-	-	-
18.91	2.93E-03	0.427	-	-	-
18.00	3.01E-03	0.454	-	-	-
13.83	3.46E-03	0.581	-	-	-
11.16	3.86E-03	0.662	-	-	-
9.34	4.23E-03	0.717	-	-	-
8.02	4.58E-03	0.757	-	-	-
7.03	4.92E-03	0.787	-	-	-
6.26	5.26E-03	0.810	-	-	-
5.64	5.58E-03	0.829	-	-	-
5.15	5.91E-03	0.844	-	-	-
4.73	6.23E-03	0.857	-	-	-
4.39	6.55E-03	0.867	-	-	-
4.09	6.87E-03	0.876	-	-	-
3.83	7.18E-03	0.884	-	-	-
3.61	7.50E-03	0.891	-	-	-
3.41	7.81E-03	0.897	-	-	-
-	8.12E-03	0.902	-	-	-
-	8.44E-03	0.907	-	-	-
-	8.75E-03	0.911	-	-	-
-	9.06E-03	0.915	-	-	-
-	9.37E-03	0.919	-	-	-
-	9.68E-03	0.923	-	-	-
-	9.99E-03	0.926	-	-	-
-	1.03E-02	0.929	-	-	-
-	1.06E-02	0.932	-	-	-
-	1.09E-02	0.934	-	-	-

Table A1.6: Additional CDP inelastic behaviour parameter inputs for (CDP generator – MTdc)

Compressive Behaviour		
Yield Stress	**Inelastic Strain**	**Damage Parameter**
3.41	*7.81E-03*	*0.897*
3.19	8.13E-03	0.903
2.98	8.44E-03	0.910
2.77	8.76E-03	0.916
2.55	9.07E-03	0.923
2.34	9.38E-03	0.929
2.13	9.70E-03	0.935
1.92	1.00E-02	0.942
1.70	1.03E-02	0.948
1.49	1.06E-02	0.955
1.28	1.10E-02	0.961
1.07	1.13E-02	0.968
0.85	1.16E-02	0.974
0.64	1.19E-02	0.981
0.43	1.22E-02	0.987

THIS PAGE WAS INTENTIONALLY LEFT BLANK

ANNEX II. BOND STRESS-SLIP RELATIONSHIPS
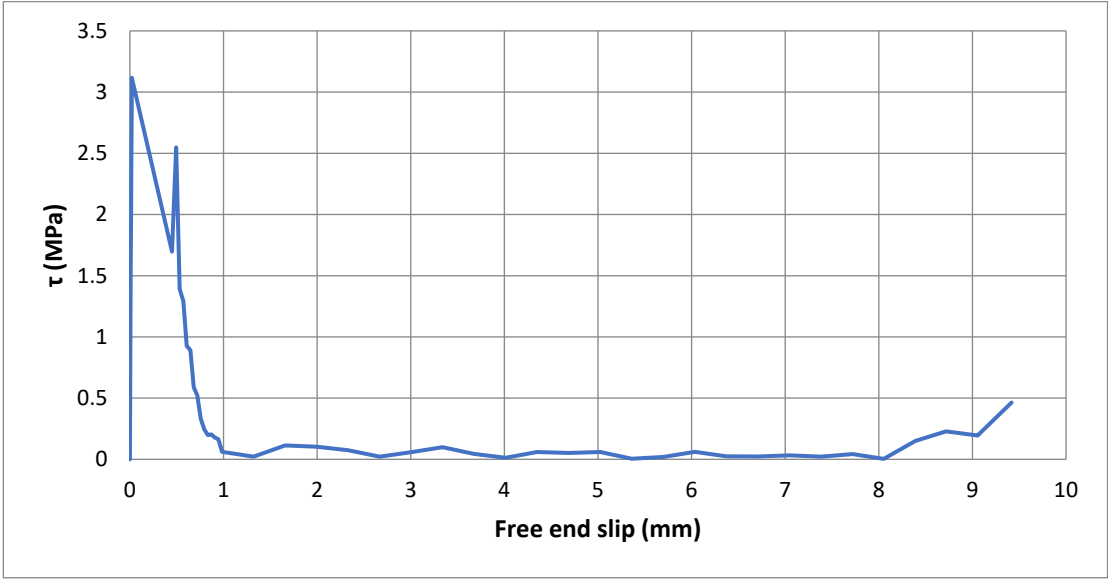
Figure A2.1: Free-end bond stress-slip relationship with the new defined amplitude in section 4.2 with concrete failure.

Figure A2.2: Bond stress-slip relationship comparison with different unbonded area modelling of rebar.

Following the improvements in Figure 4.11, the tensile behaviour was modified for a higher damage value of 0.98, to be equivalent to that of compression. This change resulted in the elimination of the friction plateau due to the complete degradation of the materials. With no residual stiffness to be a means of obtaining the behaviour, the plateau past 7 mm was reduced to 0 MPa as in Figure A2.3.
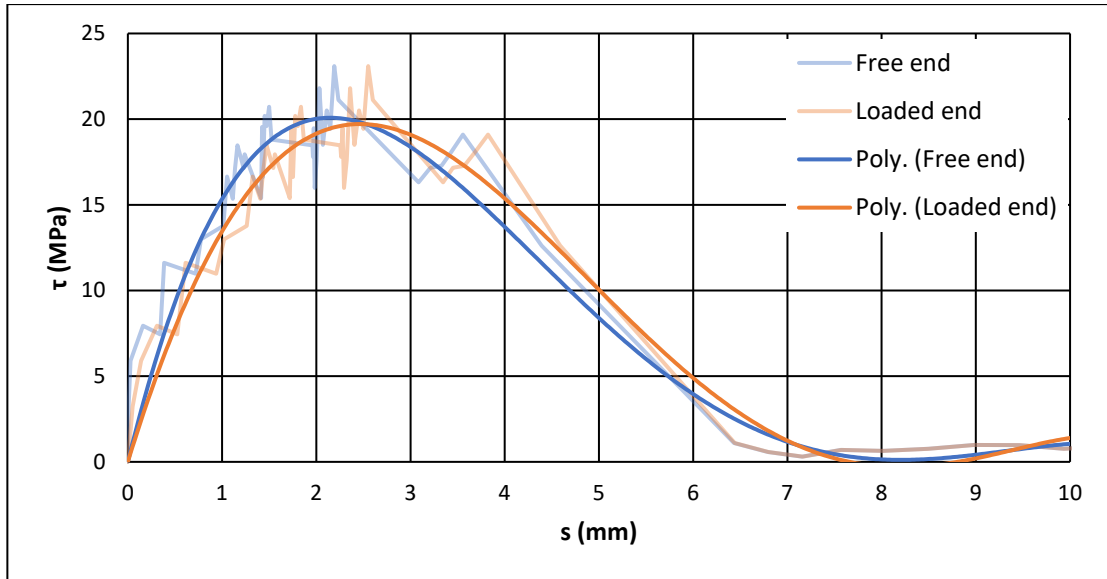
Figure A2.3: Bond stress-slip relationship with modified tensile damage reaching 0.98 in the EC2 model.
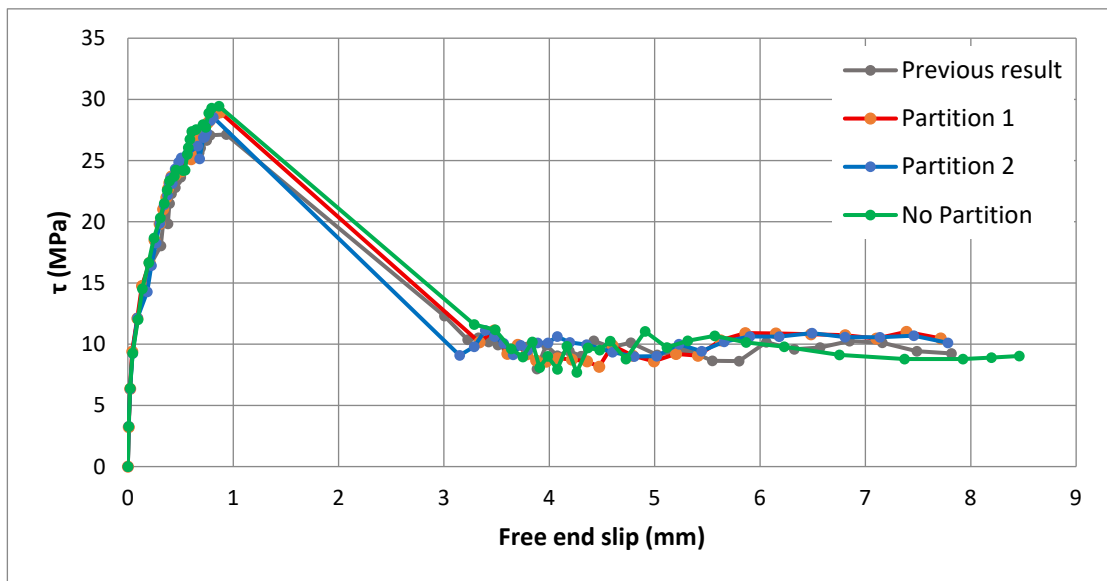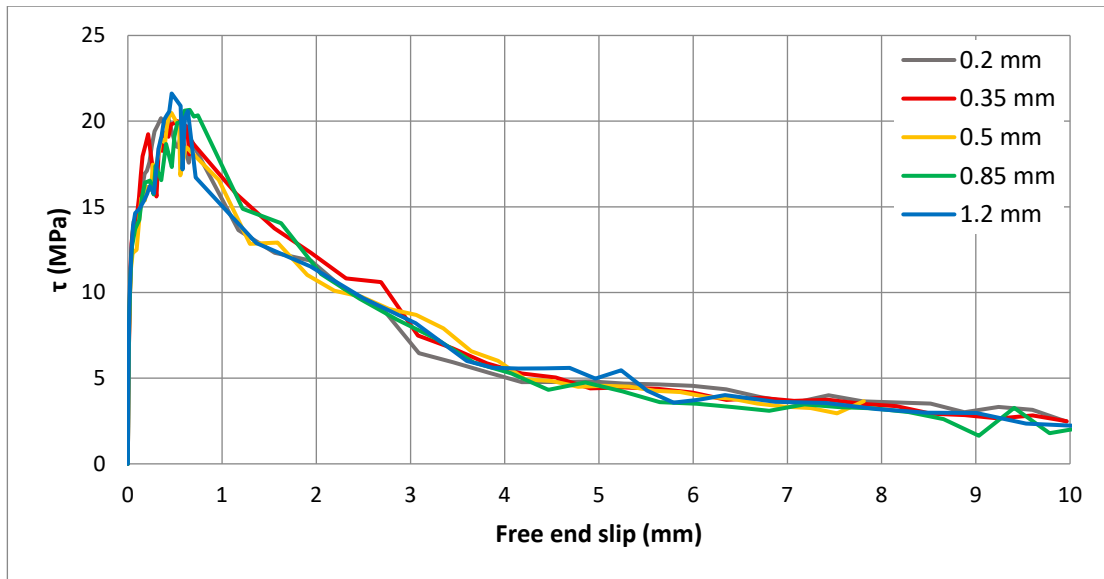

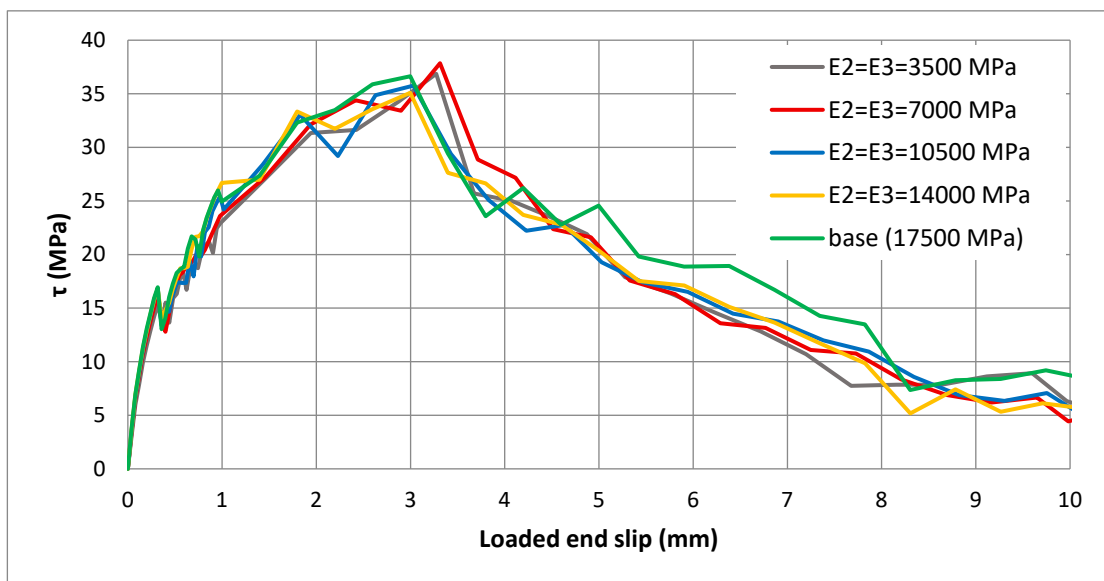**Figure A2.4:** Partition location sensitivity analysis results for (MT) CDP model input.
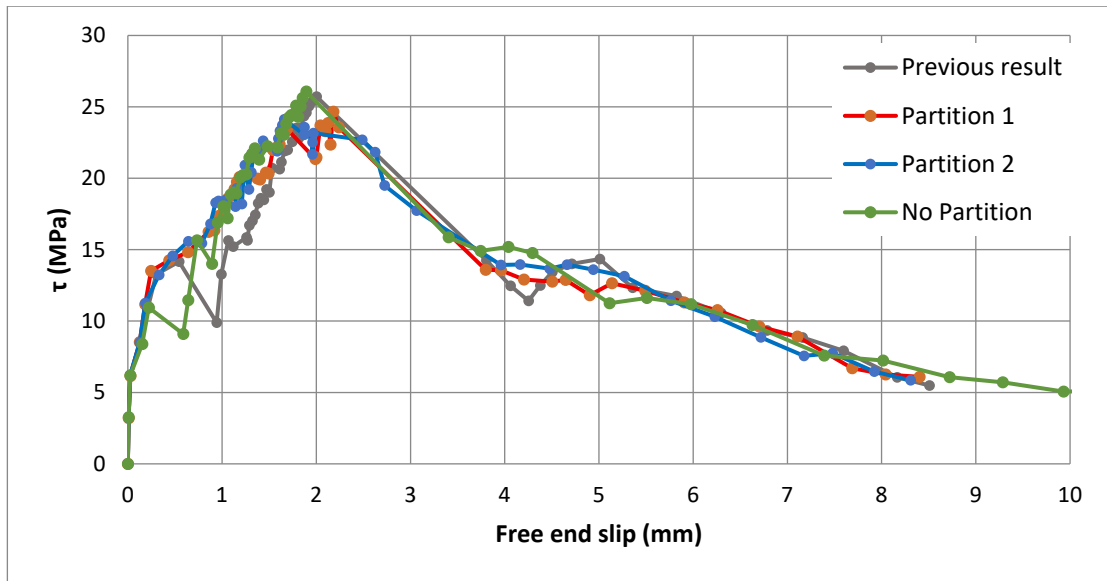
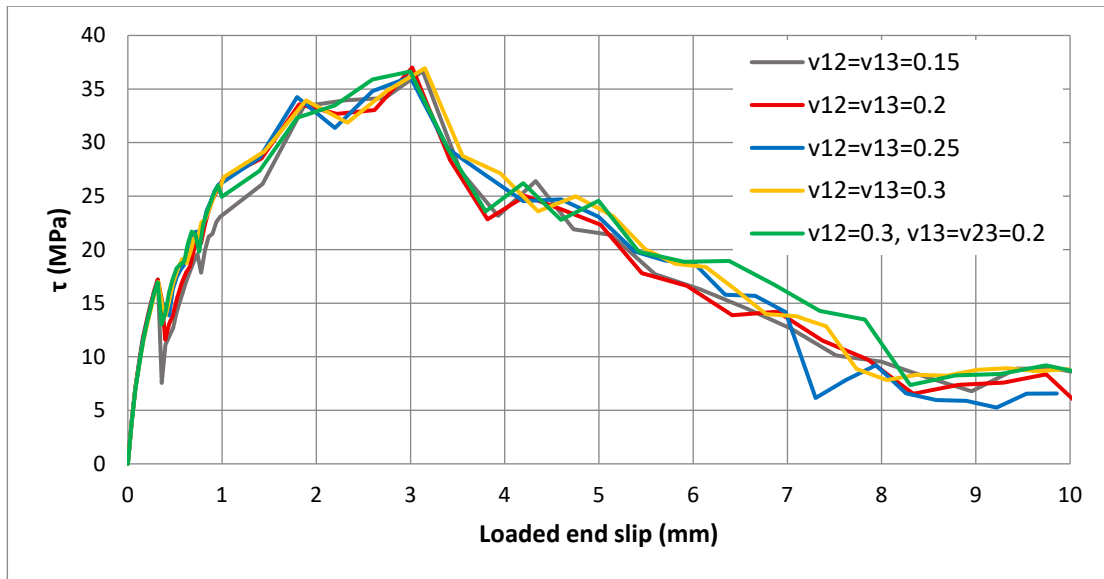**Figure A2.5:** Partition location sensitivity analysis results for (MT-dc) CDP model input.
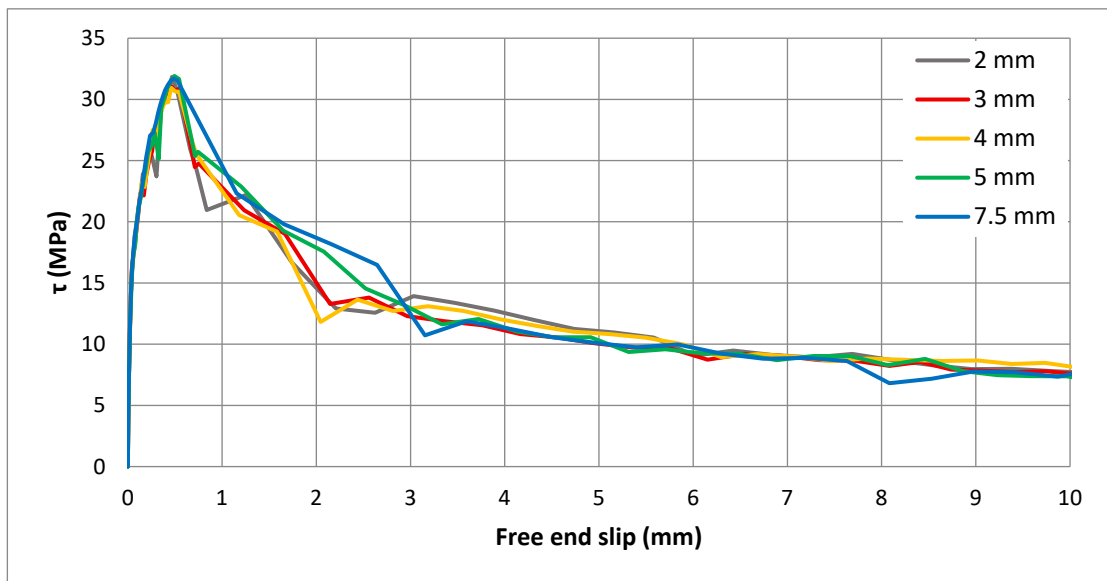
Figure A2.6: Bond stress-slip relationships from coarse mesh sensitivity analysis.
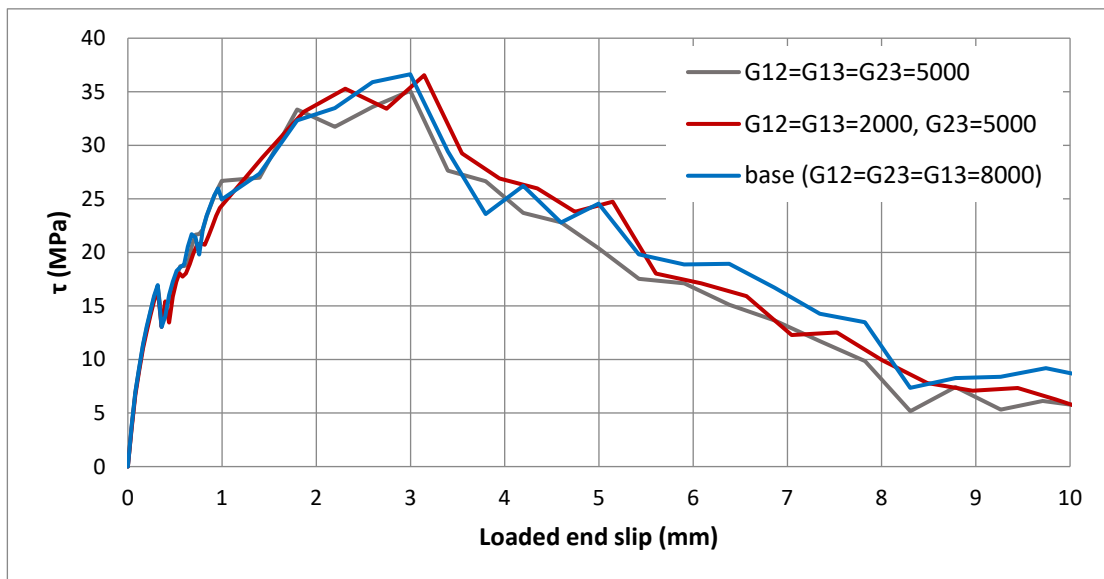
Figure A2.7: Bond stress-slip relationships from fine mesh sensitivity analysis.

Figure A2.8: Bond stress-slip relationship of D06S2 rebar transverse stiffness parametric study.

Figure A2.9: Bond stress-slip relationship of D06S2 rebar Poisson's ratio parametric study.

Figure A2.10: Bond stress-slip relationship of D06S2 rebar shear stiffness parametric study.